Development of a Liquid-PbBi Target for ISOL@MYRRHA

Donald Houngbo

Promotoren: prof. dr. ir. J. Vierendeels, dr. L. Popescu
Proefschrift ingediend tot het behalen van de graad van
Doctor in de ingenieurswetenschappen

UNIVERSITEIT
GENT

Vakgroep Mechanica van Stroming, Warmte en Verbranding
Voorzitter: prof. dr. ir. J. Vierendeels
Faculteit Ingenieurswetenschappen en Architectuur
Academiejaar 2016 - 2017

ISBN 978-90-8578-932-1
NUR 928, 924
Wettelijk depot: D/2016/10.500/64

## Supervisors:

Prof. dr. ir. Jan Vierendeels (UGent)
Dr. Lucia Popescu (SCK•CEN)

## Research lab:

Department of Flow, Heat and Combustion Mechanics (FloHeaCom)
Ghent University
Sint-Pietersnieuwstraat 41
B-9000 Gent
BELGIUM

## Members of the exam committee:

### Chairman:

| | |
|---|---|
| Prof. Gert De Cooman | UGent |

### Reading committee:

| | |
|---|---|
| Prof. Pierre Bricault | TRIUMF & Université Laval |
| Ir. Marc Dierckx | SCK-CEN |
| Prof. Dieter Fauconnier | UGent |
| Dr. Paul Schuurmans | SCK-CEN |

### Other members:

| | |
|---|---|
| Prof. Joris Degroote | UGent |
| Dr. Lucia Popescu | SCK-CEN |
| Prof. Jan Vierendeels | UGent |

This research was funded by the SCK•CEN Academy for Nuclear Science and Technology and the BriX network project P7/12 of the Interuniversity Attraction Poles (IAP) programme of the Belgian Science Policy Office.

# Acknowledgement

Although a PhD dissertation bears the name of a single author, this research is far from a one man's job. The work leading to this manuscript has been influenced by many people and I would like to hereby express my gratefulness to them.

In the first place I would like to thank my supervisors, prof. dr. ir. Jan Vierendeels and dr. Lucia Popescu. They both invested their time, experience and patience in the research and my personal development. Whenever I could not find the solution to a problem related to numerical simulations either in my mind or in literature, I could always get a hint through discussions with Jan. Complementarily, the daily interaction with Lucia provided me with opportunities to spot aspects of the isotope-release calculations that require additional thoughts. I could also always count on her reviews of written documents and on her guidance when preparing presentations. I would also like to thank you both for the freedom you gave me in defining my research path, while providing me with your support and steering.

Many thanks to dr. Paul Schuurmans for challenging me with constructive criticism at different stages of the research. My warm thanks go to prof. dr. ir. Joris Degroote, for filling the gap in my knowledge on fluid structure interaction calculations and coupling algorithms with a remarkable sense of devotion and enthusiasm. The work would have been much more difficult without the support of two key people: Radu Popescu and Yves Maenhout who helped out with issues related to clusters at SCK•CEN and UGent. I

would like to express my gratitude to Radu for enabling parallel FLUKA runs on the SCK•CEN cluster.

I am grateful to Lars Ghys and all the colleagues of the Proton Target Research unit of SCK•CEN for the fruitful discussions. I am thankful as well to Jeroen De Ridder and all the colleagues of the fluid mechanics research group at Ghent University. My gratitude also goes to Luca Egoriti for investing his effort into a master thesis topic of relevance for my research. I would also like to thank administrative teams, both at the Flow heat and Combustion mechanics department of Ghent University and at SCK•CEN.

Finally, I would like to thank my parents and my younger brother for their encouragement. Last but not least, my gratitude goes to my girlfriend Cristelle Messan for her patience throughout these years.

Donald HOUNGBO

Ghent, June 2016

# Summary

Radioactive Ion Beams (RIBs) are used as a tool by physicists to study nuclei far from stable nuclei in the nuclide chart (see Figure 0.1). The RIBs used in these studies are produced via different methods, among which the Isotope Separation Online (ISOL). At current ISOL facilities, part of the requested RIBs cannot be delivered because they necessitate R&D. In order to meet the requirements of certain experiments, it is necessary to increase RIB-intensities by several orders of magnitude.

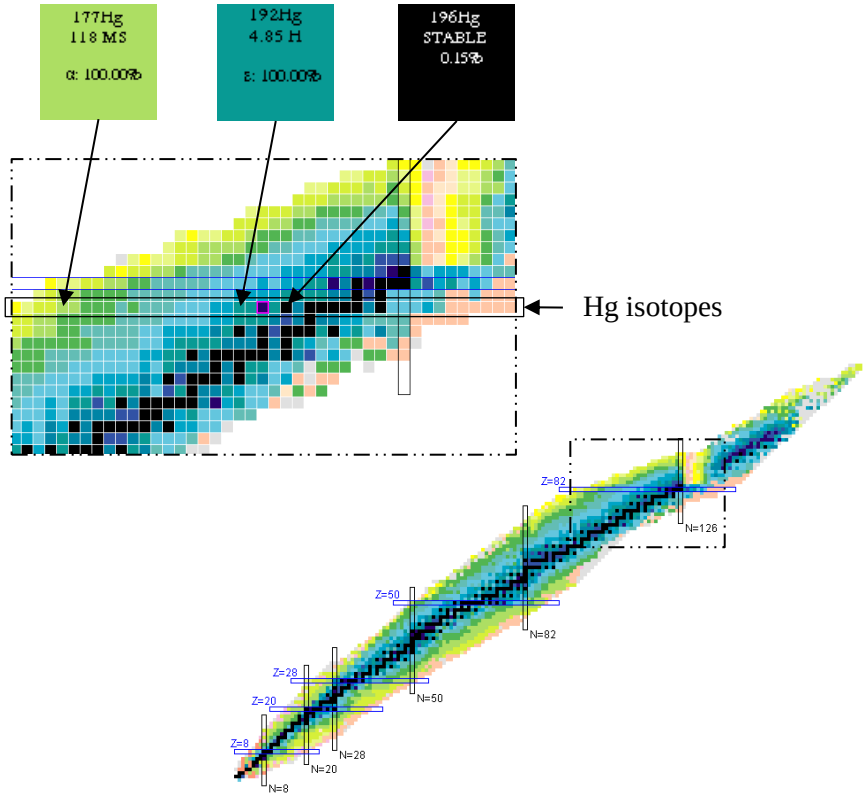


Figure 0.1: The chart of nuclides, with an excerpt focusing Hg isotopes.

The project EURISOL aims at increasing the RIB intensity by up to four orders of magnitude. However, because of the substantial technological developments required for such a facility, intermediate-generation facilities like ISOL@MYRRHA have been planned. A common feature of these facilities is their high-power driver beam which results in an increased heat deposition in targets. This induces a need for development of a new generation of targets capable of operating under this high-power condition.

A molten metal target concept, capable of addressing this need, was proposed within the EURISOL Design Study (see Figure 0.2). Because such a target is of interest for different ISOL facilities, a project entitled LIEBE (LIquid lEad Bismuth eutectic loop target for EURISOL) was initiated for the detail design and construction of a prototype Pb-Bi loop target setup. This work comprises the conceptual design and simulations of the target. Because the target material flows in a loop equipped with a heat exchanger, this target concept is capable of handling high power primary-beams. In addition, liquid targets typically have a higher number of target atoms per unit area of beam spot, as compared to solid targets. This usually results in higher in-target production rates. Also, as in this concept the irradiated liquid is fractionated into small droplets, good release properties can be envisaged.

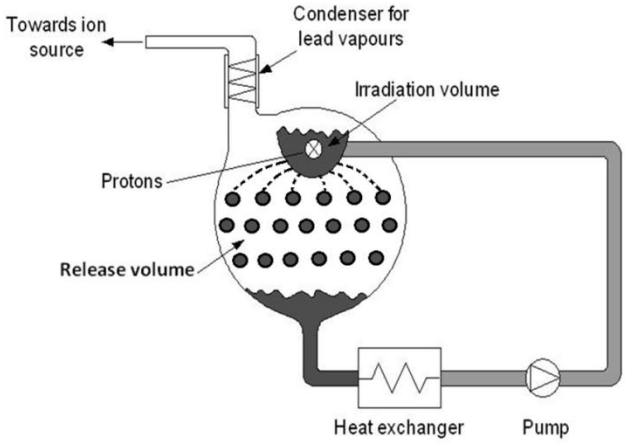


Figure 0.2: Conceptual view of the molten metal loop target.

Effects like pressure drop, cavitation, liquid-metal recirculation, instabilities and non-uniform flows are studied for the design of this target. These phenomena are most crucial inside the irradiation volume, as they can significantly affect the performance of the target. A major design requirement is a complete evacuation of the irradiated lead-bismuth-eutectic (LBE) within 100 ms after the impact of a proton pulse. The dynamics of LBE in the irradiation volume was analyzed, with CFD simulations, in order to ensure a proper design.

Starting from a simple cylindrical geometry, several improved configurations of the irradiation volume have been studied. In each of the proposed satisfactory geometries, the inlet-jet effect was solved with a combination of two approaches: (1) increasing the size of the inlet sections in order to reduce inlet velocities; (2) positioning one or two feeder grids to distribute the inlet jet over the length of the irradiation volume. A parallelepiped-shape feeder proved to be the most robust of the satisfactory concepts, with regards to risks of clogging.

Upon irradiation by a proton pulse, the liquid target material is fractionated into droplets inside the release volume. This release volume must be optimized for the reference nuclide of interest, $^{177}$Hg, of which the half-life is only 0.118 s. A sound engineering of the release volume is therefore crucial in order to minimize decay losses during the release of these nuclides. In this objective, a proper modeling of the release of nuclides out of the target is a requisite. A computational approach to predict the release of nuclides out of the target and assess its efficiency was thus developed.

The proper test case for validation of the proposed release model is a loop-type target. However, in the absence of experimental data for the liquid loop-target, measured data on several targets operated online were used. These are the ISOLDE-SC Pb target and two Ta foil targets with different internal geometries. In all these cases, a good match between computed and experimental release curves and efficiencies has been observed for a variety of isotopes of different elements.

The method proposed, to predict the release of nuclides, was then applied to optimize the design of a molten LBE loop target. Optima of different parameters have been determined and it was found that the optimum size of the target is species and half-life dependent. In addition, the shorter the half-life of the isotope of interest, the more compact is the optimum target design.

When passing through the target material, the driver beam can deposit significant amounts of energy in the target through Coulomb interactions. The energy loss profile was computed with FLUKA, a Monte Carlo code for particle transport in matter. This profile was then used to calculate initial temperature and pressure distributions in the target using Fluent. These calculations provide insight into effects generated by proton-induced shocks in this liquid metal target under a highly pulsed beam. The simulations show

that strong pressure waves develop in the target but no severe constructive interference was found when using the 16.2-μs bunch spacing of the beam.

The prototype will be constructed and tested at CERN-ISOLDE. Offline tests are foreseen this fall and the prototype is planned for online tests in November 2016.

# Samenvatting

Radioactieve ionenbundels (RIBs) worden door fysici gebruikt om kernen te bestuderen die zich op de nuclide-kaart ver van stabiliteit bevinden (zie Figuur 0.1). De RIBs die gebruikt worden in deze studies worden geproduceerd via verschillende methodes, waaronder de 'Isotope Separation Online' (ISOL) techniek. Huidige ISOL faciliteiten kunnen echter een deel van de gevraagde RIBs niet of onvoldoende afleveren, waardoor verder onderzoek een noodzaak is. Het is namelijk voor sommige experimenten nodig om de RIB-intensiteiten van bepaalde isotopen te verhogen met verschillende grootte-ordes.

Om aan deze vereisten tegemoet te komen, is het EURISOL project opgestart met als doel om de RIB-intensiteit met vier grootteordes te verhogen. Omdat er substantiële technologische ontwikkelingen nodig zijn voor zulke faciliteit, zijn er plannen om faciliteiten te bouwen van een tussengeneratie, zoals ISOL@MYRRHA. Een gemeenschappelijk kenmerk van deze installaties is een primaire bundel met een hoog vermogen, waardoor er een verhoogde warmte-afzetting is in de protondoelwitten. Dit zorgt ervoor dat het noodzakelijk is om een nieuwe generatie van doelwitten te ontwikkelen die in staat zijn om deze hoge vermogens te weerstaan.

Om aan deze eis te voldoen werd binnen de ontwerpstudie van EURISOL een protondoelwit van gesmolten metaal voorgesteld (zie ook Figuur 0.2). Omdat zo een target interessant is voor verschillende ISOL installaties, werd een project genaamd LIEBE (LIquid lEad Bismuth eutectic loop target for EURISOL) opgestart. Dit project heeft als doel om een prototype van een doelwit met een Pb-Bi kringloop te ontwerpen en te bouwen. Dit werk omvat het conceptuele ontwerp en de simulaties van dit protondoelwit. Omdat het materiaal in een lus met een warmtewisselaar stroomt, kan dit ontwerp primaire bundels van een hoog vermogen weerstaan.

Daarenboven hebben doelwitten van een vloeibaar materiaal meestal een hoger aantal atomen per eenheid oppervlakte van de primaire bundel in vergelijking met vaste doelwitten. Hierdoor hebben vloeibare doelwitten vaak een hogere productiesnelheid van radioactieve isotopen. In dit concept

wordt de bestraalde vloeistof ook verstoven in kleine druppels, waardoor een efficiënte vrijgave van radio-isotopen mogelijk is.

Verschillende effecten, zoals drukverlies, cavitatie, recirculatie van vloeibaar metaal, instabiliteiten en niet-uniforme stromen, werden bestudeerd voor het ontwerp van dit protondoelwit. Deze fenomenen zijn het meest cruciaal in het bestraalde volume omdat deze de prestaties van het doelwit significant kunnen beïnvloeden. Een belangrijke voorwaarde voor het ontwerp is een complete evacuatie van het bestraalde eutectisch lood-bismut mengsel (LBE) binnen 100 ms na de impact van een proton puls. De dynamiek van LBE in het bestraalde volume werd geanalyseerd met CFD simulaties om een degelijk ontwerp te realiseren.

Startend van een simpele cilindrische geometrie werden verschillende verbeterde configuraties van het bestraalde volume bestudeerd. In elk van de voorgestelde concepten werd het effect van een instromende straal opgelost door een combinatie van de volgende twee oplossingen: (1) het vergroten van de aanvoerbuizen om de snelheid van de inkomende vloeistof te verlagen; (2) het positioneren van één of twee roosters die de inkomende vloeistofkolom verdelen over de ganse lengte van het bestraalde volume. Een aanvoervolume in de vorm van een parallellepipedum bleek het minste risico te hebben op het vormen van klonters in het gesmolten metaal.

Wanneer het vloeibare metaal wordt bestraald door een protonpuls, wordt het verstoven in kleinere druppels zodat isotopen kunnen worden vrijgegeven. Het volume waar deze vrijgave plaatsvindt, moet worden geoptimaliseerd voor de referentiekern, $^{177}$Hg, die een halfwaardetijd heeft van slechts 0.118 s. Een goed ontwerp van dit volume is daarom cruciaal om het verlies door het radioactief verval van deze kernen tijdens hun vrijgave te minimaliseren. Een degelijk model van de vrijgave van kernen uit het protondoelwit is daarom belangrijk. Daarom werd een computationele aanpak ontwikkeld om dit proces te beschrijven en de bijhorende vrijgave-efficiëntie te bepalen.

Ideaal gezien zou dit model getest worden op een protondoelwit met een kringloop. In de afwezigheid van experimentele data van zo een protondoelwit werd het model getest op verschillende doelwitten die momenteel online worden gebruikt. Het gaat hier over het ISOLDE-SC Pb doelwit en twee protondoelwitten bestaande uit Ta-folies met verschillende interne configuraties. In al deze gevallen werd er een goede overeenkomst gevonden tussen berekende en experimentele vrijgave-curves en de

bijhorende efficiënties voor verschillende isotopen van verschillende elementen.

Deze methode om de vrijgave van kernen te modelleren werd dan toegepast om het ontwerp van het protondoelwit met een kringloop van gesmolten LBE te optimaliseren. Het optimum van verschillende parameters werd bepaald en er werd vastgesteld dat de optimale grootte van het protondoelwit afhankelijk is van zowel het element als de halfwaardetijd van de nuclide. Een kortere halfwaardetijd van de desbetreffende kern betekent dat het optimale ontwerp van het protondoelwit compacter is.

Wanneer de primaire bundel door het doelwit beweegt worden er significante hoeveelheden energie afgezet in het materiaal door middel van Coulomb interacties. Dit energieverlies werd in kaart gebracht met behulp van FLUKA, een Monte Carlo code voor deeltjestransport in materie. Deze resultaten werden dan gebruikt om de initiële temperatuur- en drukverdeling in het doelwit te berekenen met behulp van het programma Fluent. Deze berekeningen geven inzicht in de vorming van schokgolven in het vloeibare metaal wanneer een sterk gepulste bundel wordt gebruikt. De simulaties tonen aan dat sterke drukgolven ontstaan in het protondoelwit, maar ook dat er geen zware constructieve interferentie ontstaat door de spatie van 16.2 µs tussen twee groepen in een protonpuls.

Het prototype zal gebouwd en getest worden in CERN-ISOLDE. Offline testen zijn voorzien tijdens deze herfst en het prototype zal online worden getest in november 2016.

# Table of Contents

# Abbreviations and Symbols

## Abbreviations

| | |
|---|---|
| AC | Angular Coefficient method |
| ADS | Accelerator Driven System |
| ARIEL | TRIUMF's Advanced Rare IsotopE Laboratory |
| CEA | Commissariat à l'énergie atomique et aux énergies alternatives |
| CERN | European Organization for Nuclear Research |
| CFD | Computational Fluid Dynamics |
| DSMC | Direct Simulation Monte Carlo |
| ESS | European Spallation Source |
| EURISOL | European ISOL facility |
| EURISOL-DS | EURISOL- Design Study |
| FLUKA | FlUktuierende KAskade, a multi-particle transport code |
| FWHM | Full Width at Half Maximum |
| HIE-ISOLDE | High Intensity Energy-ISOLDE |
| IF | In-Flight Separation |
| IGISOL | Ion-guide ISOL |
| IPUL | Institute of Physics of University of Latvia |
| ISAC | TRIUMF's Isotope Separator and Accelerator |
| ISOL | Isotope Separation Online |

| | |
|---|---|
| ISOL@MYRRHA | ISOL-facility project for Fundamental physics at MYRRHA |
| ISOLDE | Isotope Separator On Line Device |
| LBE | Lead Bismuth Eutectic |
| LIEBE | LIquid lEad Bismuth eutectic loop target for EURISOL |
| MC | Monte Carlo |
| MCNP | Monte-Carlo N-Particle transport code |
| MEGAPIE | Megawatt pilot experiment |
| MYRRHA | Multipurpose hYbrid Research Reactor for High-tech Applications |
| ***pdf*** | probability density function |
| PS-Booster | Proton-Synchrotron-Booster |
| PSI | Paul Scherrer Institute |
| RIB | Radioactive Ion Beam |
| RISP-IBS | Rare Isotope Science Project of the Institute for Basic Science |
| RIST | Radioactive Ion Source Test tantalum foil target |
| SC | SynchroCyclotron |
| SCK•CEN | Belgian Nuclear Research Centre |
| SINP | Saha Institute of Nuclear Physics |
| SPES-INFN | Selective Production of Exotic Species at the Istituto Nazionale di Fisica Nucleare |
| SPIRAL 2-GANIL | Système de production d'Ions Radioactifs en Ligne de 2$^{ème}$ génération, at the Grand Accélérateur National d'Ions Lourds |

| | |
|---|---|
| SST | Shear Stress Transport |
| Ta129 | Tantalum foil target, reference 129 |
| TPMC | Test Particle Monte Carlo |
| WP | Work-Packages |

## Symbols

| | | |
|---|---|---|
| $\alpha$ | Surface tension | $\mathrm{N/m}$ |
| $\Delta t$ | Time duration | s |
| $\Delta H_a$ , $E_{des}$ | Adsorption enthalpy | eV |
| $\varepsilon$ | Efficiency | |
| $\rho$ | Density | $\mathrm{kg/m^3}$ |
| $\lambda$ | Molecular mean free path | m |
| $\sigma$ | Standard deviation (Ch. 2) | m |
| $\sigma$ | Cross section (Ch. 3) | barn |
| $\phi$ | Azimuthal angle | rad |
| $\tau_a$ , $\tau_s$ | Mean surface residence time | s |
| $\tau_f$ | Mean flight time of an effusing particle between consecutive surface interactions | s |
| $\mu$ | Dynamic viscosity | kg/(ms) |
| $\theta$ | Zenith angle | rad |
| $a$ | Radius (Ch. 3) | m |
| $C$ | Concentration | $\mathrm{kg/m^3}$ |
| $d$ | Molecular diameter | m |

| | | |
|---|---|---|
| $D$ | Diffusion coefficient | $m^2/s$ |
| $F$ | Rate of transfer | $kg/m^2s$ |
| I | Intensity | $s^{-1}$ |
| $i, j, k$ | Effusion fit parameters | |
| $k_B$ | Boltzmann constant | J/K |
| $Kn$ | Knudsen number | |
| $L$ | Mean length of nuclide paths from initial desorption to exit from release volume | m |
| $L_c$ | Characteristic scale of the gas flow | m |
| N | Number of neutrons | |
| $N_{col}$ | Mean number of collisions of an effusing particle | |
| $N_{target}$ | Number of target atoms per unit area of beam spot | $m^{-2}$ |
| p | Pressure | Pa |
| $r$ | Radius (Ch. 2) | m |
| $r$ | Radial coordinate (Ch. 3) | m |
| $R$ | Delay time distribution | $s^{-1}$ |
| Re | Reynolds number | |
| $T$ | Temperature | K |
| $t$ | Time | s |
| $t_{1/2}$ | Half-life | s |
| $v$ | Velocity | m/s |

| | |
|---|---|
| We | Webber number |
| Z | Number of protons |

## Subscripts

| | |
|---|---|
| 0 | End of proton pulse (Ch. 2) |
| 0 | Initial (Ch. 3) |
| $bs$ | Bath Surface |
| $di$ | Diffusion |
| $ds$ | Droplets Surface |
| $ef$ | Effusion |
| $ev$ | Evacuation of isotopes |
| $ev\,min$ , $ev\,max$ | Lower and Upper limits of integration on evacuation time |
| $fall$ | Fall in release volume |
| $fev$ | Full evacuation of irradiated LBE |
| $i$ | Initial |
| $ion$ | Ionization |
| $irr$ | Irradiation volume |
| $is$ | Ion Source |
| $liq$ | Liquid |
| $post-acc$ | Post acceleration |
| $rel$ | Release |
| $s$ | Liquid surface |

| | |
|---|---|
| $sep$ | Mass separation |
| $stor$ | Storage |
| $transp$ | Transport |
| $vap$ | Vapor |
| $x,y,z$ | x-,y- and z-direction |

# 1 Introduction

This introductory chapter aims at framing the research performed here in its general background. The nuclides studied in nuclear physics are produced artificially as Radioactive Ion Beams (RIBs) if they are not naturally occurring. However, while of interest, beams of many nuclides are still challenging to produce with sufficient intensity and purity. In order to enable production of RIBs of these nuclides, new facilities are currently under consideration worldwide.

The different techniques for production of RIBs are introduced in the first section of the chapter. In all the techniques, the production of a RIB first requires the interaction of a primary beam of particles with a target. The target materials and the reaction-mechanisms used for RIB production with the Isotope Separation Online (ISOL) technique are presented in the second section.

In order to improve the production of RIBs of challenging nuclides, future ISOL facilities are foreseen with a high intensity primary beam. At these facilities, introduced in the third section of the chapter, the high intensity primary beam leads to an important heat deposition in the target. The target concept studied in this work has been specifically imagined for the dissipation of a large amount of deposited heat.

In the ISOL technique, one of the main factors hindering the production of RIBs is the release efficiency of nuclides out of the target. The aim of the work reported here is to propose an efficient design of the loop target concept. The chapter ends with a description of the research goals.

## 1.1 Radioactive Ion Beams Production

### 1.1.1 Motivation

Radioactive Ion Beams are a tool for physicists to study nuclei far from stability. Based on current knowledge, more than 6000 nuclides are expected to exist of which about 3600 have been observed even though

many of them are still to be studied in full detail [1]. The systematic study of these nuclides is expected to provide significant insight on nuclear physics and models. Next to providing nuclear physicists with a detailed understanding of many aspects in nuclear interaction and dynamics, radioactive beams are useful in other fields of science such as nuclear astrophysics, solid-state physics, and nuclear medicine.

### 1.1.2 Production

The RIBs used in the studies mentioned above are mainly produced via two complementary techniques schematized in Figure 1.1: the In-Flight Separation (IF) [2] and the Isotope Separation Online (ISOL) [3-5]. A third technique also used in RIB production is the ion-guide ISOL (IGISOL) [6]. In all methods, nuclei of interest are transported from their location of production so that they can be studied in dedicated setups well shielded from the significant radiation background of the production area. Along the transport, the energy, the time structure and the ion optical properties of the beam can be adapted for specific experiments.

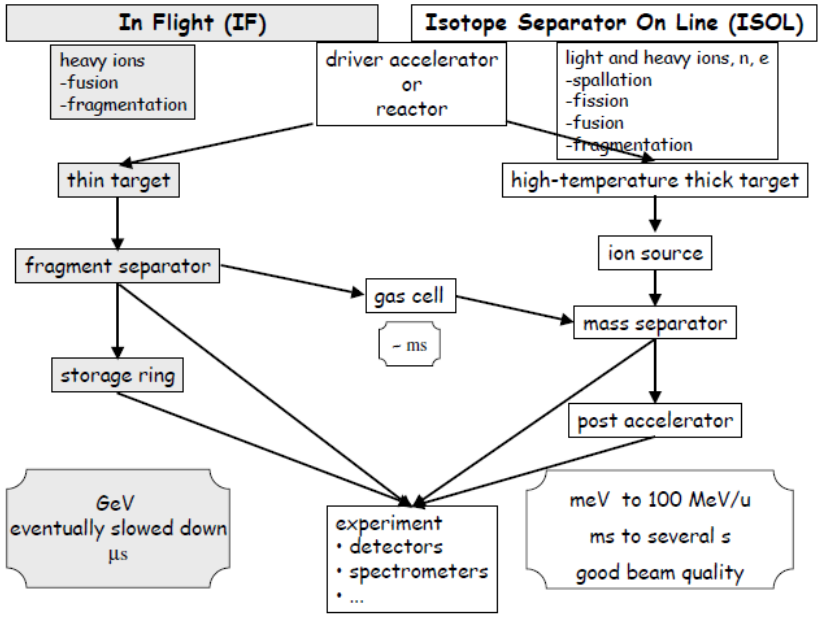


Figure 1.1: A generic description of the In-Flight and Isotope Separator On Line techniques [1].

### *1.1.2.1 The In-Flight Separation technique*

In the In-Flight Separation technique a primary beam of typically heavy and energetic ions is directed on a thin target (~ 0.3 to ~ 3 g/cm$^2$) [2]. This technique relies on the forward emission of reaction products that occurs in nuclear reactions induced by heavy and high energy projectiles. In such reactions, whether fragmentation, fission or fusion, reaction residues retain the initial kinetic energy of the beam. These energetic reaction products then recoil out of the thin target with a charge state distribution. This results in nuclei having large forward momenta and a relatively sharp forward angular distribution. Out of this full momentum and angular distribution, a given portion is selected based on magnetic rigidity, which yields a set nuclei with a specific momentum-to-charge ratio [2]. If the reaction products recoil at nearly the same velocity as the unreacted primary beam particles, this initial momentum-to-charge-ratio selection is essentially a mass-to-charge-ratio separation, leading to primary beam rejection.

However, in combination with the in-target reaction kinematics, processes like multiple angular scattering and energy loss straggling induce unavoidably large beam emittance values. For these reasons, the kinetic energy spread of the beam is relatively large and the beam at this step consists of a cocktail of nuclei with different masses, atomic numbers, momenta and charge states. Further selectivity is therefore required. It can be obtained by passing the preselected nuclei through a degrader where the energy loss depends on the atomic number [7] and afterward through a second momentum-to-charge-ratio selection device [8, 9]. However the use of a degrader has the drawbacks of increasing the transverse emittance of the beam and generating secondary products through nuclear reactions in the degrader. In-flight separated beams are injected in gas cells in order to reduce their momenta, or injected in cooler rings to reduce both size and momentum spread. This step has the drawback of increasing flight time and consequently the decay losses between production and analysis.

### *1.1.2.2 The Isotope Separation Online (ISOL) technique*

In the ISOL technique a primary beam of light or heavy particles, generally protons, interacts with a thick target (~5 to ~200 g/cm$^2$). A wide variety of primary particles, energies, reactions and target materials combinations are available to produce the radionuclides of interest. Reaction mechanisms used in the ISOL technique include: spallation, fission, fragmentation and fusion evaporation. The appropriate reaction mechanism for the production of an ion beam from a particular isotope depends on its position in the

nuclide chart as well as its physical and chemical properties. Once produced, the radionuclides are thermalized in a solid or gaseous catcher. Often, the target material also serves as catcher. The target/catcher is kept at high temperature to promote a fast release of the radionuclides. When required, physical and chemical properties of the reaction products and the target/catcher materials are utilized to enhance or prevent the release of desired or unwanted nuclides respectively.

When solid or liquid catchers are used, the release process typically includes diffusion out of the catcher material and effusion towards the ion source. Part of the effusion process takes place in a transfer line with a suitably controlled temperature, connecting the target/catcher to an ion source. It often provides selectivity based on physics and chemistry between the effusing elements and the transfer line material. In the ion source, different mechanisms are available to ionize the isotopes of interest, depending on the ionization potential or electron affinity [3] of the isotopes of interest as well as the required charge state and selectivity. Additionally, selectivity is obtained with surface ionization and more-so with resonant laser ionization. Resonant laser ionization is so chemically selective that it results in a significant reduction of isobars or even isomers, when the laser bandwidth is narrow enough [4].

The ions are subsequently extracted and accelerated in a 30-60 keV electric field. This low-energy ion beam is directed into a mass separator where ions with a specific mass-over-charge-ratio are selected. When required, the beam is post-accelerated. ISOL beams are characterized by high purity and small transverse emittance, albeit that, in the absence of a post-accelerator, the energies of the ions are low. For exotic RIBs, the high purity constitutes a major advantage since studying the exotic nuclei is often hindered if they are submerged in a high background of more stable nuclei also produced in the target. However, decay losses during the isotope-release and in the ion source are the main drawback for the production of very short-lived isotopes of half-lives in the millisecond range and below through the ISOL technique.

#### *1.1.2.3 The ion-guide ISOL (IGISOL) technique*

The IGISOL technique has been proposed to overcome the limitation of the ISOL technique concerning the production of beams of very short-lived isotopes. Similarly to the In-Flight Separation, it relies on the recoil of high momentum reaction products out of a thin target, upon the impact of the

primary beam. Reaction products, recoiling in a high charge-state are however thermalized in a cell filled with noble gas (helium or argon). Along with the thermalization process, charge-exchange reactions occurring in the cell with the gas atoms induce a reduction in charge state of the reaction products. Still, the high ionization potential of noble gases ensures that eventually, part of the reaction products end up with a 1+ or 2+ charge state. The surviving ions are evacuated with the gas via an exit hole in the cell, extracted and mass separated. The formation and survival of the 1+ or 2+ ions along the transport through the cell is affected by their residence time in the cell, the purity of the gas, the density of electrons and ions in the cell and potentially the chemistry of the nuclides. Beside the non-selective ionization, recombination and neutralization of ions in the gas are key issues with this technique. However in case of significant neutralization, resonant laser ionization can be efficiently applied [10].

#### *1.1.2.4 Reaction mechanisms for RIB production*

Different reactions mechanisms are used in the RIB production techniques presented above: fission, spallation, fragmentation and fusion. The general features of these mechanisms are described in this section.

**Fission**

Based on the specific proton to neutron ratios of heavy nuclides in the stability valley, neutron-rich nuclei of medium mass (mass number 60~170) are readily produced from fission of long lived actinides. Primary beams of low/high-energy protons, heavy ions, fast/thermal neutrons or electrons through photo-fission can be used to induce the fission mechanism. When thermal neutrons are required, neutrons from a reactor can be used. Alternatively, neutrons are produced in a converter when fast neutrons are requested. The converter method for neutrons consists of dumping a high power beam of protons or deuterons in a well-cooled neutron production target while the generated neutrons induce fission in a separate target with less power deposition. Gamma rays can similarly be produced out of an electron converter to induce photo-fission. Nuclei with a kinetic energy of approximately one MeV/nucleon are created in the fission process [2]. When fission is the desired production mechanism for an in-flight or an IGISOL facility, the kinetic energy of the fissioning nucleus has to be large compared to the fission recoil. Yet, even in this case, only one of the two fission products is generally accepted by current in-flight separators.

**Spallation**

Spallation is one of the reactions induced by the interaction of high energy proton beam with a target. It results in the emission of an important number of protons, neutrons and $\alpha$ particles from the target nuclei. Spallation products are distributed on the neutron-deficient side of the nuclear chart, over nuclides having few protons less than the target nuclei. Production cross-sections decrease for very neutron deficient isotopes but this can partially be compensated by the use of thick ISOL targets with high-energy protons. The cross section for production of a nuclide expresses the likelihood for the production of this nuclide in the target, through different reactions. The type and energy of particles in the primary beam are parameters that determine the production cross-section, as well as the target-material composition.

**Fragmentation**

Two types of fragmentation reactions are distinguished, depending on which of the target or projectile nuclei are fragmented. Because of its kinematics requirements, in-flight separation mainly makes use of projectile fragmentation with a high-energy heavy ion beam, typically above 50 MeV/nucleon [11]. At ISOL facilities, in addition to projectile fragmentation, target fragmentation is also applied whereby a heavy target is bombarded with a high-energy proton beam [12, 13]. Both types produce a wide variety of isotopes, some lying close to the fragmenting target/projectile nucleus in the nuclear chart and others lying in the very light nuclei region of the chart.

Fragmentation is described as an initial peripheral interaction of the projectile with a target nucleus followed by a de-excitation step. Few nucleons are stripped in the initial interaction and Coulomb deflection induces a small recoil of the excited residues (projectile or target). In projectile fragmentation, the kinetic energy of the projectile residue is typically much larger than both the Coulomb deflection and the isotropic recoil from the de-excitation, which explains the forward momentum of fragments suitable for in-flight separation.

Fragment cross-sections have been reported to be relatively constant for energies in the range ~40 MeV/nucleon to ~2 GeV/nucleon [14], except for fragments close in mass with the initial nucleus. Cross-sections are larger for these fragments. Neutron-rich nuclei are best produced with heavy

production stable targets and proton-rich nuclei near stability are produced with the heavy N ~ Z targets [2].

**Light- and Heavy-ion Fusion Evaporation Reactions**

Light-ion fusion reactions produce slightly neutron-deficient nuclei and are characterized by a high cross section and a high-intensity primary beam. On the other hand, lower cross-sections are characteristic of heavy-ion fusion evaporation reactions which lead to the production of neutron-deficient nuclei. In this case, heavy-ions beams with energies around MeV/u are operated with lower intensities due the significant heat deposition in-target. For the same reason, thinner targets are required for heavy-ion fusion evaporation. However, fusion reactions produce on average a lower number of different isotopes (typically 10 for the heavy-ion reactions) than other reaction mechanisms discussed above [4]. A property of fusion reactions with importance for in-flight separation or IGISOL is that, at the exit of the target, the momentum of the reaction products is significantly lower than that of the beam particles [2].

Additional details on the different reaction mechanisms can be found in the following references showing their large application [2, 4, 15, 16]. Even though nuclides in different regions of the chart are known to be most suitably produced via certain reaction mechanisms, no clear classification is currently accepted. Indeed, improvements in target design can, among others, affect the suitability of a certain reaction mechanism for the production of a specific isotope. A description of ISOL targets is given in the next section.

## 1.2 ISOL targets

ISOL facilities provide radioactive beams for a multitude of applications. Several parameters influence the yields achievable by an ISOL target. These include the geometrical layout of the target and transfer line, along with the thermal conductivity, emissivity, range of operational temperature and radiation hardness of the target and container materials on the one hand. On the other hand, parameters like the cross section, half-life, diffusion coefficient and adsorption enthalpy of the nuclei also affect the yields.

The design of an ISOL target is based on the optimization of both the in-target production rate and the efficiency of isotope release from the target. Typical ISOL targets are cylinders, 10 to 20 cm in length and 1 to 2 cm in diameter (see Figure 1.2).

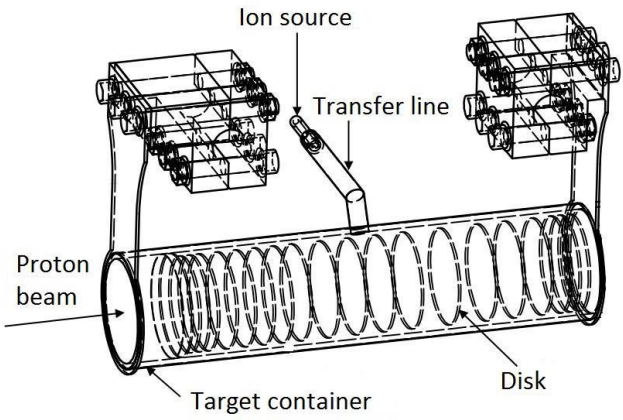


Figure 1.2: Schematic representation of a typical solid ISOL target [17].

The target is connected via a transfer line to the ion source. After diffusing out of the target material, nuclei undergo a succession of adsorption and desorption steps that compose the effusion process. This effusion process takes place both in the target volume and in the transfer line. When required, the temperature of the target can be brought up to 2500 °C to enhance diffusion of nuclei out of the target material [3]. At facilities where the target heating by the beam is not enough, complementary ohmic heating is used. This is the case at ISOLDE (driver beam power < 6 kW). Conversely, at TRIUMF-ISAC (driver beam power = 50 kW), the target container is equipped with external radiator fins for cooling purposes.

This section gives an overview of different ISOL targets (liquid metals, solid metals, carbides and oxides), pointing out specific pros and cons.

**Solid-metal targets**

Effusion of elements with high adsorption enthalpy requires a high temperature in both the target and transfer line. Thus, metals with a high melting point, like Ti, Nb, Ta and W are good candidate target materials for such cases. To keep the diffusion path short, the solid-metal target material is often shaped as thin foils, 2 to 25-μm thick. Different layout of metal targets such as annular discs [18], D-shape discs [19], multi-strip foils [20] and single-strip rolled-foil [18] have been used or studied.

The single-strip rolled-foil is the standard Ta target material layout at CERN-ISOLDE while D-shape discs are typically used at TRIUMF-ISAC. In the ISOLDE target, the foil is embossed to keep separate the layers,

avoiding thermal contact between layers. For similar reasons, the D-shape discs in the TRIUMF target are cut slightly oversize with respect to the inner diameter of the target container and stacked inside it with a tight contact. Besides, metal-target materials in powder form have been studied both off-line [21] and on-line [22, 23]. Still, the number of metals with acceptable properties is rather limited. Under the conditions of operation of ISOL targets, metals tend to melt or react with the container material. Further, slow diffusion has been observed for some elements in solid metals. In such cases, refractory compounds like carbides and oxides are considered.

**Carbides**

The chemical properties of metals like actinides, lanthanides, titanium and chromium render possible the formation of stable carbides. Uranium and thorium carbides [24] have specifically been studied at many ISOL facilities. The target material is typically a carbide/graphite mixture in pressed-powder form [25], in thin foils [19] or as impregnated graphite cloth [26]. A multitude of neutron-rich medium-size nuclei are routinely produced with uranium carbide targets at ISOLDE [27]. In the standard ISOLDE uranium carbide/graphite targets [28], powders of uranium oxide and high purity graphite are mixed and cold-pressed into 1-mm thick pills. The pills are then heated in a graphite container under vacuum so that the graphite reacts with the uranium oxide, leading to the release of carbon monoxide. The open porosities created by the release of the carbon monoxide are of significant importance in the release properties of the final material. A graphite sleeve, 2-mm thick, is inserted in order to prevent a reaction between the pills and the target container.

At TRIUMF, a different procedure is used for the production of composite carbide target material among which the uranium carbide target. In this production method, the carbothermal reduction of uranium oxide is followed by slip-casting a mixture slurry of uranium dicarbide and graphite on a graphite foil. D-shaped thinner foils of fine grains (< 10 μm) are obtained. The main operational limitation of carbides is the potential decomposition of the compound under ISOL conditions leading to pressure buildup from the release of the metal component or impurities.

**Oxides**

Some oxide compounds are also stable enough at high temperatures to serve as ISOL target material. Noble gas nuclides like He, Ne, Ar, Kr and Xe have

been produced at ISOLDE from MgO, CaO, $TiO_2$, SrO, $ZrO_2$, $La_2O_3$, $CeO_2$. Oxides from actinides like uranium and thorium have also been studied [28]. These oxide target materials were mostly produced either by sintering commercial oxide powders or via the decomposition of carbonates under vacuum [29]. Note that oxide-powder targets tend to sinter and close open porosities over time, at ISOL temperatures.

Commercial oxide material in the form of felt or cloth has also been used with the distinct feature that it contained no binder and did not lead to excessive outgassing when operated at high temperatures. Impregnation of a commercial felt with the desired target element has also been an option when the desired oxide material is not commercially available as a felt. Fast diffusion was ensured by the size of the fiber, 5 – 10 μm.

In both cases, the target material is usually inserted in a thin foil platinum or rhenium container in order to avoid a direct contact between the oxide and the tantalum target container, thus preventing oxidation risks. Oxide targets are however not suitable for the production of isotopes of elements that form refractory oxides.

**Liquid targets**

One significant parameter in targetry is the areal thickness ($g/cm^2$) of the target, deriving from the density of the target element in the target material. Contrary to compound targets, bulk-material targets typically offer the largest areal thickness values of any ISOL target, but a bulk material of the size of an ISOL target would induce long diffusion paths for the produced nuclei. Molten metals were studied as they combine a fast diffusion coefficient and the large in-target production rates of a bulk material. Elements with a relatively low melting point like tin, lanthanum, lead and bismuth have been used, as well as germanium, gold and eutectic alloys.

The areal thickness of molten metal targets is on average an order of magnitude higher than other ISOL targets. They can therefore provide the highest intensities for reasonably short-lived isotopes of certain elements: Cd from a Sn target, Hg from a Pb target, Xe and Cs from a La target [30]. Other liquid targets in the form of molten salts have been studied: $ThF_4$-LiF mixture [31], a eutectic mixture of $TeO_2$, KCl and LiCl [32].

Currently, liquid target-materials are generally in the form of a static bath partially filling the target container. Volatile elements with a low adsorption enthalpy are presently released from molten targets even though long release

times have been reported [33]. The long release time generated by the diffusion step could be reduced by operating the target at higher temperatures but vapor pressure of the target material dictates the highest usable temperature of the target. An alternative idea to speed up the release out of molten targets is to fragment the target material into smaller volumes [34], as studied in this work.

**Other materials**

Release studies of other refractory compounds like $BaB_6$, $CeB_6$, CeS, $Zr_5Ge_3$, $Hf_5Sn_3$ and $Ta_5Si_3$ can be found in literature [21, 32].

## 1.3 Next-generation ISOL-facility projects

### 1.3.1 ISOL@MYRRHA

Over the past years, the Belgian Nuclear Research Centre SCK•CEN has been developing MYRRHA (see Figure 1.3), a **M**ultipurpose h**Y**brid **R**esearch **R**eactor for **H**igh-tech **A**pplications [35]. The MYRRHA facility is planned to operate as an Accelerator Driven System (ADS) with spallation neutrons generated by 600-MeV and 2 to 4-mA proton beam impinging on a lead-bismuth target [36]. The high energy and high intensity proton beam of this accelerator makes it suitable for the production of radioactive ion beams (RIBs). This is the reason why, within the MYRRHA project, the ISOL@MYRRHA project (see Figure 1.3) is foreseen with the aim of producing intense high purity RIBs based on the ISOL method.

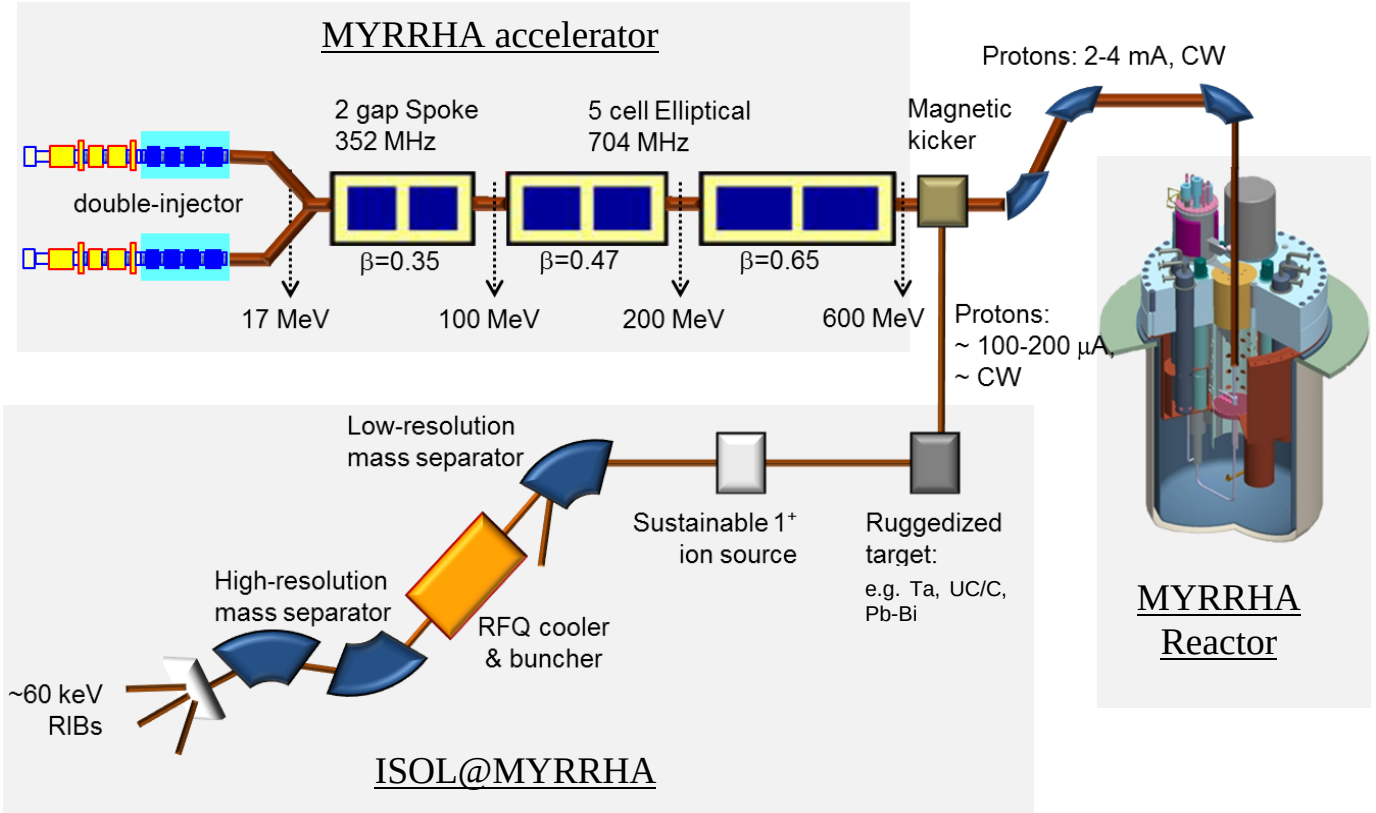


Figure 1.3: Conceptual representation of MYRRHA and ISOL@MYRRHA [37].

ISOL@MYRRHA [36] is an ISOL facility foreseen to operate with a primary beam consisting of a small fraction (up to 5%) of the proton beam from the MYRRHA-ADS accelerator [35]. With this 100 to 200-μA x 600-MeV proton beam for RIB production, 60 - 120 kW proton beam power will then be available. This is higher than currently available at operating ISOL facilities. ISOL@MYRRHA aims to be complementary to existing and future facilities, by focusing on experimental programs in need of long uninterrupted beam times [36]. Given the higher primary-beam power at ISOL@MYRRHA, as compared to running ISOL facilities, the development of new targets is mandatory. Among other ruggedized targets for the RIB production at ISOL@MYRRHA, a liquid Pb-Bi target is foreseen.

### 1.3.2 EURISOL

The idea behind EURISOL – a European isotope-separation-on-line (ISOL) facility – is to provide a unique ISOL-based facility for European scientists. The project aims at the design and subsequent construction of the next-generation European ISOL-facility. EURISOL is intended to produce RIB yields up to four orders of magnitude higher than ISOL facilities in operation in Europe [38].

As a first step toward EURISOL, a Feasibility Study [39] was conducted by a collaboration of European laboratories. Following the Feasibility Study, a primary proton beam intensity of up to 4 MW was considered to be necessary for achieving the goal of $10^{15}$ fissions per second in the target. It also derived from this study that a liquid-metal converter target would be required to remove the heat load deposited by this multi-mega-watt beam.

To undertake further studies identified during the Feasibility Study, a Design Study (EURISOL-DS) [40] was initiated. Some technological challenges of the project, along with instrumentation and safety issues have been investigated during this Design Study. The production of elements not available from the fission of uranium was investigated and three 100-kW direct target stations were planned, to host different target units. One of the target concepts proposed within the EURISOL-DS is an innovative molten metal target.

The concern that current ISOL targets are not suitable for operation with the high power primary beams of next generation facilities is relevant for EURISOL [40]. For these two facilities in project, ISOL@MYRRHA and EURISOL, ISOL targets capable of withstanding high-power primary beams without compromising the reliability of the yields and the structural integrity

of the target over extended periods of time are requested. Different concepts for high-power targets have been proposed and studied in this framework [41-44].

### 1.3.3 LIEBE

Because a molten metal target capable of operating efficiently with a high-power primary beam is of interest for different ISOL facilities, the LIEBE (LIquid lEad Bismuth eutectic loop target for EURISOL) project was initiated. The project aims at conducting a detailed design and construction of a prototype Pb-Bi loop target for RIB production. The loop target concept under study for the LIEBE project is illustrated on Figure 1.4, as proposed within the EURISOL Design Study [40, 45]. With the flowing liquid target-material this concept offers the possibility to transport the heat deposited by the primary beam to a remotely located heat exchanger. Furthermore, with respect to the efficiency for RIB-production, this concept offers the possibility of fractionating the irradiated liquid into small droplets. This reduces the length of the diffusion path from container dimensions, being a few centimeters, to a few hundred micrometers.

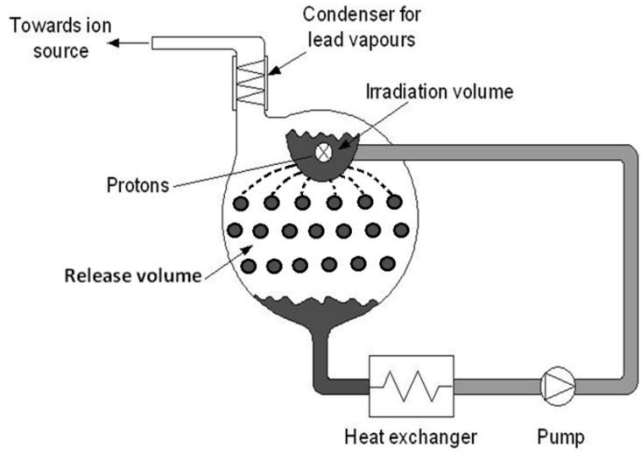


Figure 1.4: Conceptual view of the target as proposed within the EURISOL Design Study [45, 46].

Note that unlike suggested by the conceptual view on Figure 1.4, the irradiation volume studied in this work features neither an open upper half nor a free surface. The project is conducted in collaboration between several

institutes: CEA[1], CERN[2], IPUL[3], PSI[4], SCK.CEN[5] and SINP[6]. It is organized in nine Work-Packages (WP) and SCK•CEN is responsible for the WP-2: Conceptual design and simulations. The prototype should feature all components required for operation at a high primary-beam-power and will be tested at CERN-ISOLDE.

Molten Pb-Bi is considered as target material as it is suitable for the production of Hg isotopes. Neutron-deficient isotopes in this region of the nuclide chart are of interest for studies on shape coexistence in atomic nuclei [47]. In addition, both Pb and Bi have been used as target material at CERN-ISOLDE in a static bath configuration. In this configuration, the target is a cylindrical container partially filled with a static liquid target material (see Figure 1.5). The container is 2 cm in diameter and 20 cm long.

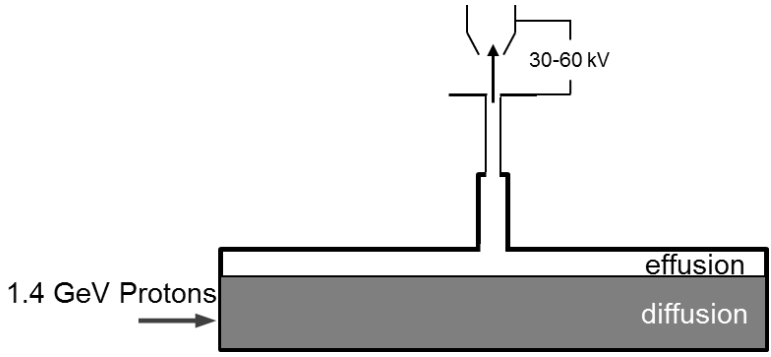


Figure 1.5: Static bath target configuration at CERN-ISOLDE [48].

## 1.4 Research goals of the present work

The production cross-sections of many of the exotic nuclides produced in the targets above are higher for high-energy proton beams. Also, since the in-target production of nuclides scales with the intensity of the primary beam, increasing the beam power on target is one of the options to increase RIB intensities. For this reason, ISOL facilities of the next generation such as ISOL@MYRRHA [36] and EURISOL [49] are foreseen with a driver

[1] CEA: Commissariat à l'énergie atomique et aux énergies alternatives, http://www.cea.fr/
[2] CERN: European Organization for Nuclear Research, http://home.cern/
[3] IPUL: Institute of Physics of University of Latvia, http://ipul.lv/main/
[4] PSI: Paul Scherrer Institute, https://www.psi.ch/
[5] SCK•CEN: Belgian Nuclear Research Centre, https://www.sckcen.be/
[6] SINP: Saha Institute of Nuclear Physics, http://www.saha.ac.in/web/

beam power of ~ 100 kW. Current targets are mostly not suitable for operation under those conditions and new target designs are required.

In their current design, molten metal targets operated at CERN-ISOLDE, the state of the art ISOL facility in Europe, are facing significant limitations to meet both future physics requirements and technical challenges of next generation ISOL facilities. Still, molten metal targets are the most efficient for the in-target production of some of the isotopes required. The aim of this research is to design a liquid Pb-Bi target for next generation ISOL facilities and especially for ISOL@MYRRHA.

In order to ensure that the designed target can handle a very high primary-beam power, the recently proposed idea of a dynamic molten metal target [46] is adopted. The molten Pb-Bi target material flows in a loop equipped with a heat exchanger. The molten Pb-Bi is irradiated by a proton beam in a dedicated container called the "irradiation volume". Soon after irradiation, liquid Pb-Bi droplets are created, forming a shower inside a release volume.

Several aspects need to be accounted for in the design of the target, including the hydrodynamics of the Pb-Bi flow, the dynamics of isotope release, the thermal effects of beam-target interactions and the consequent transient structural load.

The research goals pursued in relation with the hydrodynamics of the Pb-Bi flow are listed below:

- To define initial target geometries and predict the flow pattern in these geometries.
- To optimize the target geometry in order to obtain satisfactory flow patterns.
- To study the stability of the satisfactory flow patterns with respect to typical experimental conditions.

The study of the dynamics of isotope release was structured around the following research goals:

- To define and construct a suitable method to predict the release of isotopes from the target.

- To validate the developed method against experimental data from the most similar target.
- To study the influence of secondary effects like surface residence of effusing nuclides on the predicted isotope-release curve.
- To define an initial geometry for the release volume and predict the release of isotopes from this geometry.
- To optimize the geometry of the release volume in order to improve the release of isotopes.

Research goals with reference to the thermal effects of beam-target interactions and the consequent transient structural load are enumerated here:

- To determine the heat deposition in the target material and container due to the impact of the primary beam.
- To determine the transient thermal response of the target due to the proton-target interaction.

# 2 Target design & optimization - Hydrodynamic aspects

Different concepts for high-power targets have been proposed and studied in the framework of the preparation for the new-generation RIB facilities. Based on radiative heat transfer studies, Zhang and Alton [41] have proposed porous and fibrous composite targets, that are expected to operate with deposited beam powers of up to 40 kW. Upon testing with both resistive and electron-beam heating, the TRIUMF-ISAC high-power target equipped with a finned container was shown to be capable of dissipating more than 25 kW when operated at 2200 °C [43]. However, these different studies concern solid targets, characterized by relatively low thicknesses.

An alternative approach is the recently proposed liquid-metal-loop target [40, 45], which is expected to handle much higher primary-beam power because the target material flows in a loop equipped with a heat exchanger. In addition, liquid targets typically offer the highest thicknesses of any material ( ~200 g/cm$^2$ for Lead Bismuth Eutectic (LBE)). A thicker target typically means a higher number of target atoms per unit surface being exposed to the primary beam, which leads to higher in-target production rates for the isotopes of interest. Concerns for the design of these targets include effects like pressure drop, cavitation, liquid-metal recirculation, instabilities, non-uniform flows etc. [50-52]. Studies conducted in the past by different researchers highlight the importance of these effects on the target system [53, 54].

The liquid-metal-loop target is one of the foreseen 100-kW EURISOL direct targets and is also of interest for the ISOL@MYRRHA facility. The study reported in this chapter aims at providing solutions to specific hydrodynamics issues of concern for the design of this target. The satisfactory concepts will be prototyped and tested at CERN-ISOLDE within the LIEBE (LIquid lEad Bismuth eutectic loop target for EURISOL) project. The design optimization based on criteria detailed in section 2.1 is also presented, followed by a discussion of the hydraulic aspects of different optimized concepts.

Beam parameters considered for EURISOL, ISOL@MYRRHA and the test facility CERN-ISOLDE are given in table 1 for reference.

Table 2.1: Beam parameters for EURISOL, ISOL@MYRRHA and CERN-ISOLDE facilities.

| | Particles | Energy | Intensity | Beam structure | Pulse length | Repetition rate | Average power |
|---|---|---|---|---|---|---|---|
| EURISOL | Protons | 1 GeV | 100 µA | CW | - | - | 100 kW |
| ISOL@MYRRHA | Protons | 0.6 – 1 GeV | up to 200 µA | Interrupted CW | < 200 µs | 250 Hz | < 120 kW |
| CERN-ISOLDE (test facility) | Protons | 1.4 GeV | 1 - 2 µA | Pulsed | 2.4 – 40 µs | 0.8 Hz | 1 – 2.8 kW |

## 2.1 Target Concept

Detailed understanding of the time dependence of the release process of radioisotopes is necessary for the development of improved targets for ISOL-RIB production. Liquid-lead targets have been studied and operated at ISOLDE with 600-MeV protons from the SynchroCyclotron (SC) and later on, with 1 to 1.4-GeV protons from the Proton-Synchrotron-Booster (PS-Booster) [55]. The partially-filled liquid-metal-target containers were 20-cm long cylinders with a 1-cm radius. At the SynchroCyclotron, the time necessary to release half of the isotopes ($t_{50}$) from molten-metal targets was typically 30 to 120 s [33]. At the PS-Booster, the violent shaking of the target due to the pulsed beam has induced faster release of isotopes. However, the $t_{50}$ calculated from a fitted release function for mercury atoms was still 10 ± 5 s [33], which is long in comparison with the half-lives of some short-lived isotopes like $^{178}$Hg ($t_{1/2}$ = 0.26 s) and $^{177}$Hg ($t_{1/2}$ = 0.118 s).

The proposed concept for the liquid-metal-loop target is shown in Figure 2.1. In this concept, a dedicated container, filled with LBE, is used for irradiating the target material by the proton beam. This container, called “irradiation volume”, is placed in a vacuum chamber, called “diffusion volume”. After irradiation by protons, LBE droplets are created, forming a shower inside the diffusion volume. The droplets fall under gravity before being collected at the bottom of the diffusion volume. Meanwhile, the isotopes diffuse to the surface of the droplets, desorb from this surface and effuse towards the ion source via the transfer tube. A heat exchanger is

foreseen upstream to the pump to cool the LBE. The position of the pump is chosen to ensure that the LBE temperature at the pump inlet does not exceed maximum acceptable values for the magnets of the pump ( ~600 °C [56]). The pump ensures a constant LBE flow. Heating devices foreseen along the loop allow for a better adjustment of the temperature at start-up and during operation.

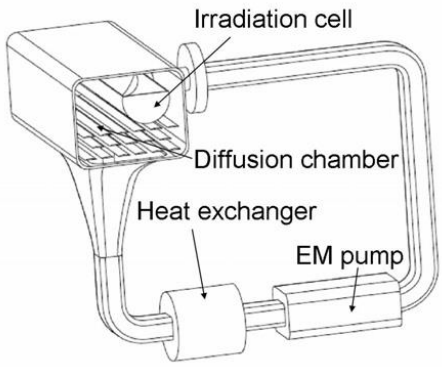


Figure 2.1: Liquid metal loop concept [45].

Based on the knowledge derived from operation of the static-bath liquid-metal targets and in order to improve the efficiency of the release process for short-lived isotopes, two major requirements were set prior to the detailed design of the liquid-metal-loop target.

Because the objective of this target is to produce short-lived isotopes like $^{177}$Hg ($t_{1/2}$ = 0.118 s), the first requirement is a fast evacuation of all the irradiated LBE from the irradiation volume into the diffusion volume. Meeting this requirement will decrease decay losses of the isotopes in the irradiation volume. In the present design, we aimed at a complete evacuation of the irradiated LBE in a shower of droplets within ~100 ms after a proton-pulse impact. The 100 ms objective is defined according to the half-life of the isotope of interest, $^{177}$Hg. Meeting this requirement also ensures that hot spots will be avoided and constitutes the main subject of the analysis in this chapter.

In order to achieve higher release efficiencies, the second requirement is to reduce the characteristic diffusion length of isotopes out of the liquid-metal. This is ensured in the present concept by decreasing the size of the LBE matrix out of which nuclides have to diffuse. Irradiated LBE will be spread into a shower of droplets with radii in the range of few 100 μm, which

represents a decrease in the characteristic diffusion length of isotopes of two orders of magnitude compared to static-bath ISOLDE liquid-metal targets.

## 2.2 Regimes of droplet formation

Droplet formation is a phenomenon arising from the interplay of different forces including gravitational forces, surface tension forces, inertial forces and linear as well as non-linear effects of waves generated by turbulent conditions, irregularities of apertures and instabilities due to pinch-off. Depending on the relative importance of these effects, the pattern of droplet formation is different. Different regimes of droplet formation have been identified experimentally [57-60].

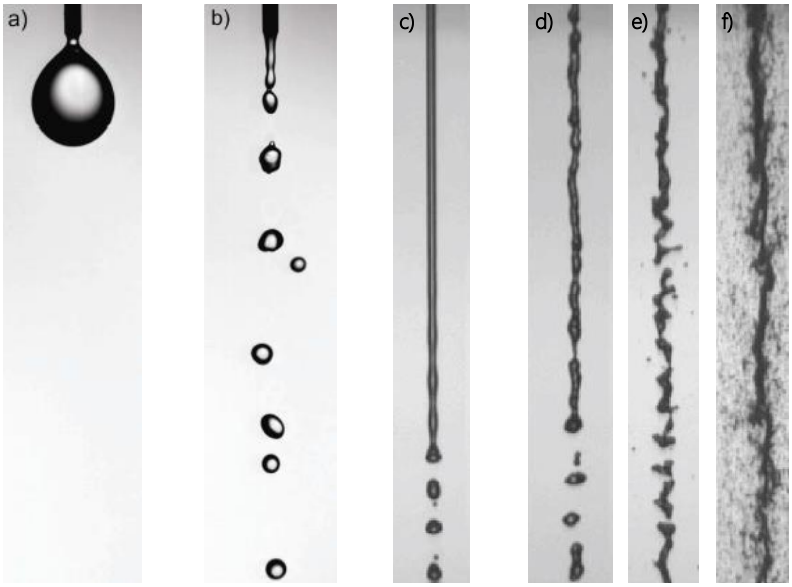


Figure 2.2: Droplet formation regimes, a) periodic dripping, b) dripping faucet, c) jetting, d) first wind-induced regime, e) second wind-induced regime, f) atomization [58].

An analysis and selection of the appropriate droplet formation regime is required for this target design since each regime has different characteristics regarding the droplet size (and thus the release fraction of isotopes), the intact length and the time dependence of the droplet formation process.

The periodic dripping regime is characterized by lower inertial forces than surface-tension forces. Pendant droplets are formed, detaching at a constant time intervals from the tip of the formation aperture when gravitational

forces become large enough. The range of pinch-off periods for this regime is however limited to large values. Droplets of a similar size are obtained. The droplet size, governed by the radius of the formation aperture is bigger than in the other regimes for a given aperture. In addition, in case of wettable formation-nozzles, the risk of droplet merging at the exit of an array of nozzles is increased [61].

The dripping faucet regime is a narrow-range transition regime characterized by a quasi-balance between inertial and surface tension forces. This results in a variable droplet size, a loss of periodicity in droplet formation and a detachment point slightly further away from the droplet-formation-aperture tip.

The jetting regime is characterized by inertial forces overcoming surface tension forces. The detachment point of droplets is moved downstream and a continuous jet is formed between this point and the aperture tip. This liquid jet undergoes capillary instabilities leading to the formation of droplets. Smaller droplets are obtained. The droplet size is independent of the jetting velocity and is only governed by the jet radius for a given liquid. It is therefore the favorable regime for production of monodisperse droplets with a high throughput [62].

The first and second wind-induced regimes [62, 63] are established when the inertia force of the environment surrounding the jet reaches a significant fraction of the surface tension forces. The breakup process is thus accelerated by two effects: the shear stress between the jet and its environment and the onset of turbulence in the jet flow. This results in a shortening of the distance between the pinch-off point and the aperture tip. As inertial forces are further increased, the fragmentation of the liquid jet into droplets moves upstream to the nozzle tip, indicating the onset of the atomization regime. In the current application, the droplets will be formed in a release volume under vacuum. There will therefore be no significant effect of the inertia of the surrounding environment. The wind-induced and atomization regimes are therefore not relevant for this application.

Due to the fact that the release fraction of species inside the diffusion chamber requires control over the droplet size, the dripping faucet regime is not the most suitable for this application. Its narrow range of applicability is an additional constraint. In the same way, because of the risks of droplet merging and film creation on the outer surface of the irradiation chamber, the periodic dripping regime is discarded. Though interesting from the

droplet size point of view, regimes beyond the jetting are not applicable. The jetting regime was then selected. The region of interest for droplet formation inside the release volume is indicated on Figure 2.3 by the dash-line triangle. It is bounded by a lower limit defined as $We_{liq} = \frac{\rho_{liq} v^2 r}{\alpha}$ which represents the transition to the jetting regime. The upper limit of the region of interest is defined by the requirement to limit the liquid velocity inside the apertures to ~ 2 m/s. Meeting this requirement will avoid important corrosion-erosion damage [63] to the droplet-formation apertures. Indeed, the corrosion of structural material in contact with LBE involves several processes but its rate is typically controlled by a slow molecular diffusion through the boundary film. As the velocity of the liquid is increased, the rate-controlling effect of molecular diffusion is restricted to the smaller viscous sublayer of the turbulent boundary layer. This results in an increased corrosion rate that is avoided here by maintaining relatively low velocities.

The dash-lines shown on Figure 2.3 correspond to different values of the Reynolds Number ($Re_{liq} = \frac{\rho_{liq} v r}{\mu}$) of LBE at 600 K, with a density $\rho_{liq}$ = 10301.8 kg/m$^3$, a viscosity $\mu$ = 1.736 mPa.s and a surface tension $\alpha$ = 0.397 N/m.

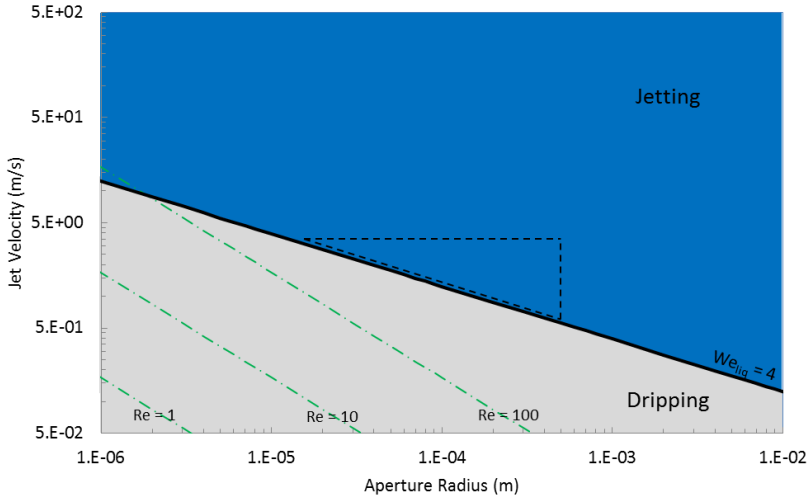


Figure 2.3: Classification of droplet formation regimes for LBE discharging from an aperture into LBE vapor at a density of 1.87 $10^{-11}$ kg/m$^3$, as a function of the jet velocity v and aperture radius r (Adapted from [62]).

The following sections present the methodology applied to study the dynamics of LBE in the irradiation volume of the target and the optimization process to meet the first requirement mentioned in section 2.1.

## 2.3 Methodology

Computational Fluid Dynamics (CFD) tools are commonly used for the thermal and hydraulic design of facilities planned to operate with a liquid-metal, e.g., MYRRHA [64], ESS [65] and EURISOL [51, 66]. Furthermore, important aspects of CFD analysis such as the turbulence modeling, pressure field and pressure drop in a liquid-metal flow have been checked. This was done by comparing experimental and computational data in the framework of thermal-hydraulics design of the MEGAPIE LBE target [51, 66]. CFD is also less expensive and faster to implement for a design-optimization procedure than prototyping each optimization step. Also, experimental R&D on targets is often complex since post-irradiation analyses are hindered by the high intrinsic radiotoxicity of the materials. Fluent (ANSYS, Canonsburg, PA, USA), has been used for the work reported in this chapter.

All the modeled CFD geometries comprise a half-symmetry of the target geometry about the XY-plane (see Figure 2.4). This assumption is explained by the fact that the distribution of evacuation apertures is symmetric with respect to the vertical mid-plane of the flow inlet. The geometries were also restricted to the fluid domain for CFD analysis and the fluid-container interaction has been modeled by adequate "no slip wall" boundary conditions. More than 22,000,000 cells are required to get mesh-independent results, e.g. in the concept discussed in section 2.4.3. The thermal effects of the proton-beam impact have not been taken into account in these calculations. This simplifies and speeds up calculations during the hydro-dynamical optimization process. Issues related to LBE-temperature profile, heat deposition and dissipation, potential occurrence of pressure waves and resonance are not treated in the present chapter. While these effects are likely to be of concern at highly-pulsed beam facilities, given the high pulse repetition rate and long pulse length (see Table 2.1), the instantaneous power densities will be rather low at ISOL@MYRRHA.

Previous calculations for liquid-metal target design, with k-$\epsilon$ and k-$\omega$ Shear Stress Transport (SST) turbulence models, have shown good agreement with experimental data (mercury target experiment for EURISOL and Lead-Bismuth for MEGAPIE) for average-flow behavior and mean-velocity fields [67, 68]. Because these models are less computationally intensive and since

no energy-mixing process is accounted for in this design-optimization process, the SST k-ω turbulence model has been used for these steady-state simulations. The settings of the calculations are summarized in Table 2.2 and details of the irradiation volume concepts studied in this chapter can be found in Appendix A.

Table 2.2: Settings of the CFD calculations

| | |
|---|---|
| Solver | Pressure based |
| Boundary condition at inlets | Specified velocity magnitude and direction normal to boundary |
| Boundary condition at outlets | Pressure outlet |
| Initial condition for steady state calculations | Hybrid Initialization |
| Initial condition for transient calculations | Flow and pressure fields from steady state calculations |
| Spatial discretization : Gradient | Least Squares Cell Based |
| Spatial discretization : Pressure | Body Force Weighted |
| Spatial discretization : Momentum | Third-Order MUSCL |
| Spatial discretization : Turbulent Kinetic Energy | Third-Order MUSCL |
| Spatial discretization : Specific Dissipation rate | Third-Order MUSCL |
| Multiphase modeling | No |

## 2.4 Results & Discussion

### 2.4.1 Starting-case geometry of the irradiation volume

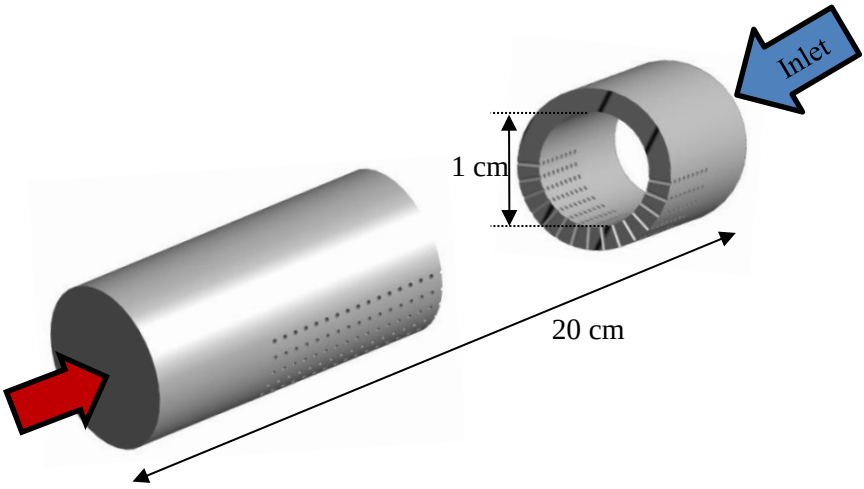


Figure 2.4: Schematic layout of the irradiation volume of concept 1.

Based on the concept presented on Figure 2.1 and described in section 2.1, the starting-case geometry presented on Figure 2.4 was used for LBE-dynamics simulation inside the irradiation volume. In this initial concept, the irradiation volume of the target consists of a 20-cm long and 1-cm diameter cylinder. The LBE flows into the irradiation volume through its base section and is evacuated through a series of apertures uniformly distributed over the lower half of the cylinder mantle. LBE-flow direction is indicated on Figure 2.4. The 1-cm diameter is selected to accommodate three standard deviations (3σ) of the proton-beam transverse Gaussian profile (FWHM ~3.5x3.5 $mm^2$ at the test facility). Potentially larger beam profiles at ISOL@MYRRHA would request correspondingly larger cross sections of the irradiation volume. The cylindrical irradiation volume and the proton-beam direction (Figure 2.4) are coaxial. This concept, called concept 1 (Figure 2.6), features 2500 evacuation apertures of 200-µm radius. These numbers are derived from the fast-evacuation (within 100 ms) requirement and the objective of reaching the jetting regime of droplet formation [57].

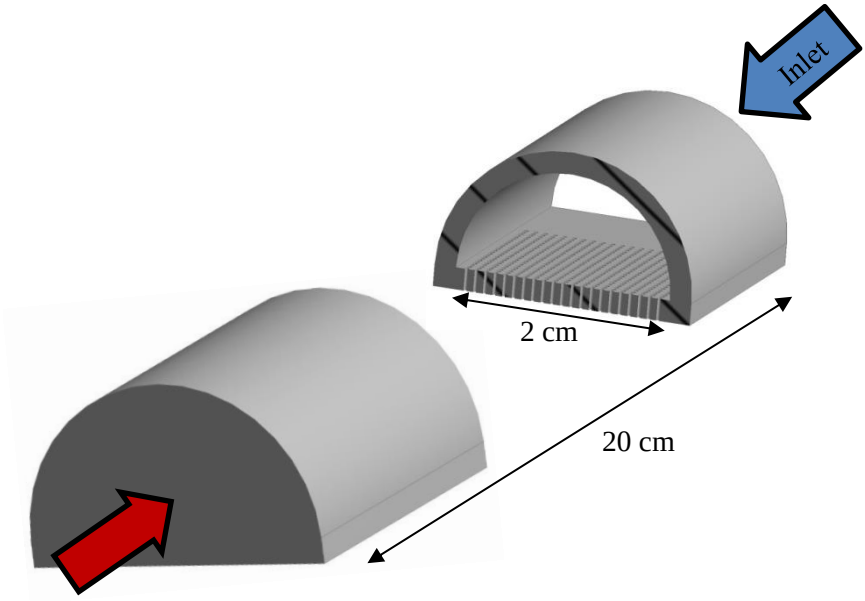


Figure 2.5: Schematic layout of the irradiation volume of concept 2.

Considering the fact that the manufacturing of the exit apertures on a cylindrical surface is quite challenging, an alternative concept 2, featuring the evacuation apertures on a flat surface (see Figure 2.5) was also analyzed. In order to accommodate 3σ for the proton beam, the cross-section area and flow rate in the irradiation volume of concept 2 are, correspondingly, twice the values in concept 1. The geometry of the irradiation volume in concept 2 is a half cylinder with 2-cm diameter. Because the flow rate is doubled, 5000 evacuation apertures are required in order to keep the formation of droplets in the same regime. Also, due to the larger irradiation volume, the average concentration of short-lived isotopes is half of that in concept 1. This affects the isotopes-diffusion efficiency.

The computed static-pressure distributions of concept 1 (Figure 2.6) and concept 2 (Figure 2.7) show very low pressure levels in the LBE inside the evacuation apertures on the inlet side of the irradiation volume. Some of these low-pressure regions have values below experimental values of the LBE saturation vapor pressure reported in literature: $10^{-6}$ Pa at 500 K [50, 69]. This poses a risk of flow-induced cavitation and erosion damage to the target structure. Evidence of cavitation erosion in a pulsed-beam liquid lead target has been reported for ISOLDE target containers [70]. While the origin of the erosion in these targets was not the flow, the risk of cavitation damage in this design should be mitigated to assure sufficient target life. Indeed,

cavitation can have the effect of limiting the target container lifetime and even lead to its failure. The envisaged lifetime of the prototype at ISOLDE is of the order of 1 – 2 weeks while EURISOL is foreseen to operate a target for 3 weeks and ISOL@MYRRHA for 4 – 8 weeks.

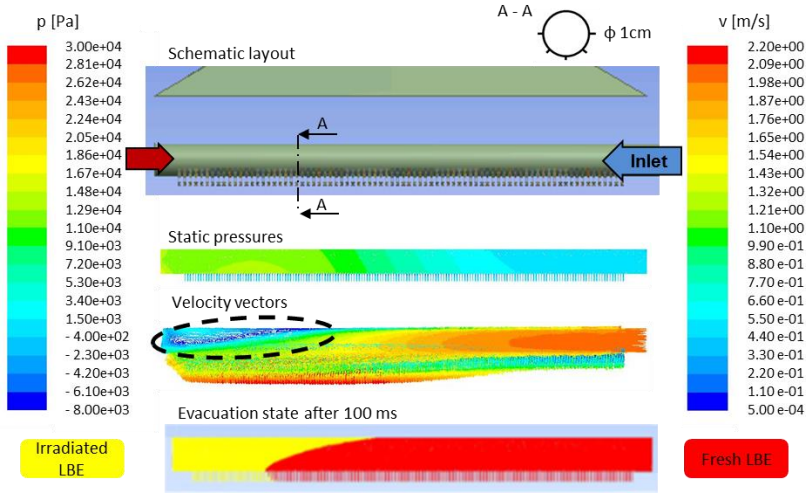


Figure 2.6: Schematic layout and CFD-analysis results (on symmetry plane) of the target design in concept 1.

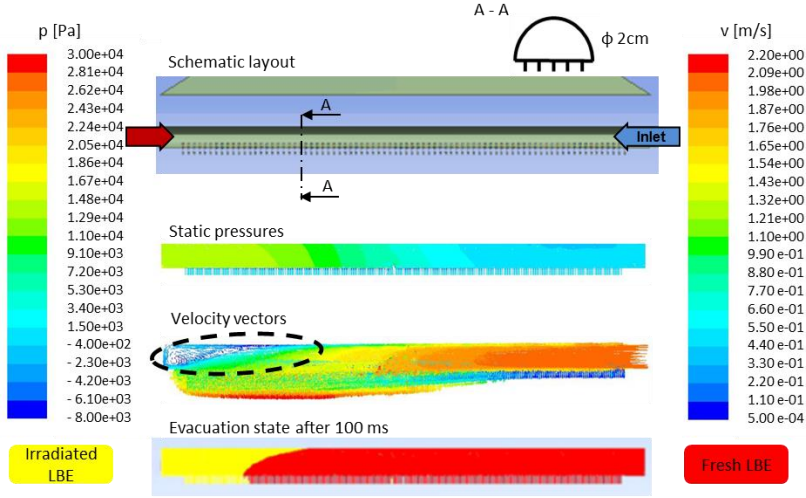


Figure 2.7: Schematic layout and CFD-analysis results (on symmetry plane) of the target design in concept 2. For consistency, pressure and velocity scales are kept the same as in Figure 2.6.

These low-pressure zones are explained by the fact that high-pressure gradients are required to bend the high-momentum LBE streamlines through the first apertures on the inlet side. The pressure values computed inside the irradiation volume at the inlet were low enough to induce almost no flow through the corresponding evacuation apertures (see velocity-vectors plots on Figure 2.6 & Figure 2.7), which also means no droplet formation through these apertures. Besides, pressure progressively builds up inside the irradiation chamber in both concepts while the average horizontal velocity decreases from right to left on Figure 2.6 & Figure 2.7. This is due to the fact that part of the inlet LBE flow is progressively lost through the evacuation apertures, and this leads to a lower flow velocity since the cross section of the flow volume is constant along the irradiation volume.

The negative values on the pressure scales are not only related to the high-momentum-streamline bending effect described earlier. Because of the stream-wise pressure build-up mentioned in the previous paragraph, an acceleration of LBE at the entrance in evacuation apertures, mostly on the left-hand side of the velocity plots (Figure 2.6 and Figure 2.7), led as well to computation of negative pressure values in the corresponding regions. Computation of these, however, unphysical negative pressure values occurs because cavitation effects were not modeled. Modeling these effects is not needed at this stage and would increase the computation time.

Recirculation zones were also noticed at the stream-wise end of the irradiation volume in both concepts because of the sudden direction change of the geometry at this end. These zones are marked by the dashed-line contours on Figure 2.6 & Figure 2.7. A close-up view on the velocities in the recirculation zone is shown on Figure 2.8 for concept 2. When they occur in the irradiation volume, these recirculation zones carry produced isotopes for extended periods of time, which leads to decay losses. For this reason, the effect of recirculation zones was studied by computing, for each concept, the portion of irradiated LBE evacuated from the irradiation volume within 100 ms after the arrival of a proton pulse. The calculation of the evacuation state was conducted in single phase, both irradiated and fresh LBE being represented by the same incompressible liquid LBE phase. These were transient calculations starting with the steady-state results as initial condition. In these calculations, a passive scalar is transported in the velocity field, setting its diffusivity to zero. The zero diffusivity corresponds to the very limited diffusion range of the isotopes of interest during the time span of the evacuation process. The fresh and irradiated LBE volumes were

then tracked by tagging them with two different values of the transported scalar.

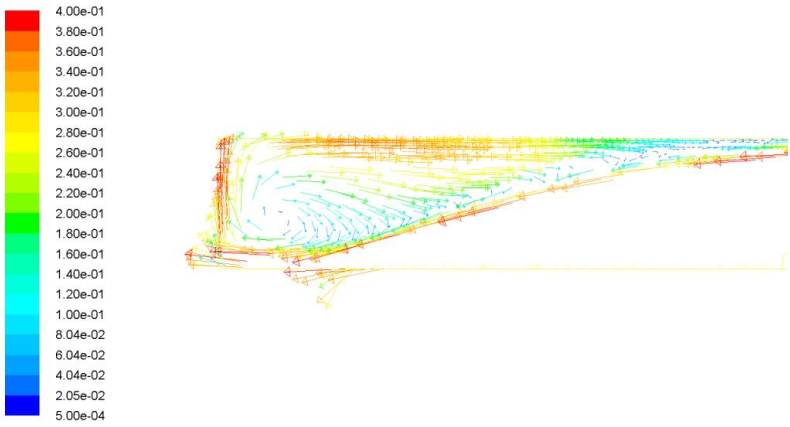


Figure 2.8: Close-up view on the velocity vectors in the recirculation zone of concept 2.

It is shown on the evacuation-state plots (Figure 2.6 and Figure 2.7) that 100 ms after the arrival of a proton pulse, portions of LBE in the recirculation zones have not been evacuated from the irradiation volume to the diffusion chamber. The turbulent mixing region at the interface between fresh and irradiated LBE is not shown on these plots since it spans over a narrow region and does not significantly affect the appreciation of the evacuation state. Throughout the chapter, a 50% threshold value is used for construction of the two-level scale evacuation-state plots.

Recirculation zones in the irradiation volume are to be avoided in order to: (1) reduce decay losses of short-lived isotopes inside the irradiation volume, as much as possible; (2) prevent occurrence of hot spots and (3) ensure a proper cooling of the beam window at high proton beam power.

In summary, the main issues detected for these two concepts are: the presence of very low pressure zones, a non-uniform distribution of evacuation velocity-vectors along the proton-beam direction and the recirculation of LBE inside the irradiation volume.

Consequently, these simple concepts cannot be used. The design optimization that will be discussed in the following sections considered successively-improved concepts to overcome these issues. From this point on, the half-cylinder design of the irradiation volume in concept 2 has been

dropped because its results have not shown any specific advantage to compensate for its major disadvantages: a larger irradiation-chamber volume, a higher flow rate (i.e. it requires more power at the pump since pressure drops are of the same order in concepts 1 and 2) and more evacuation apertures per unit surface meaning higher cost for manufacturing and higher risks of merging between closer LBE jets.

### 2.4.2 Transverse-inlet irradiation volume

Concept 3 (see Figure 2.10), features a cylindrical irradiation volume with two inlets perpendicular to the proton-beam axis. The irradiation volume is a 20-cm long and 1-cm diameter cylinder, like in concept 1. Hence, it requires the same number of evacuation apertures. Since each of the two inlets has the same cross-section area as the inlet in concept 1, the inlet velocity in concept 3 is half of that in concept 1.

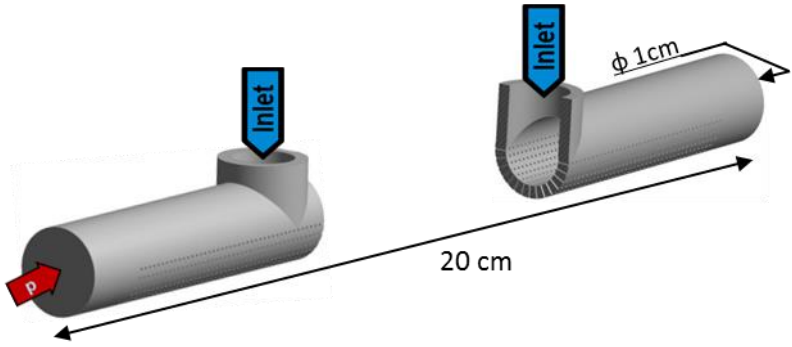


Figure 2.9: Schematic layout of the irradiation volume of concept 3.

The use of transverse inlets suppresses the need to bend streamlines over small radii of curvature at inlet and solves the related issue of low-pressure regions observed in concept 1 and 2. Results are presented in Figure 2.10. A more uniform distribution of pressure and evacuation-velocity vectors is observed.

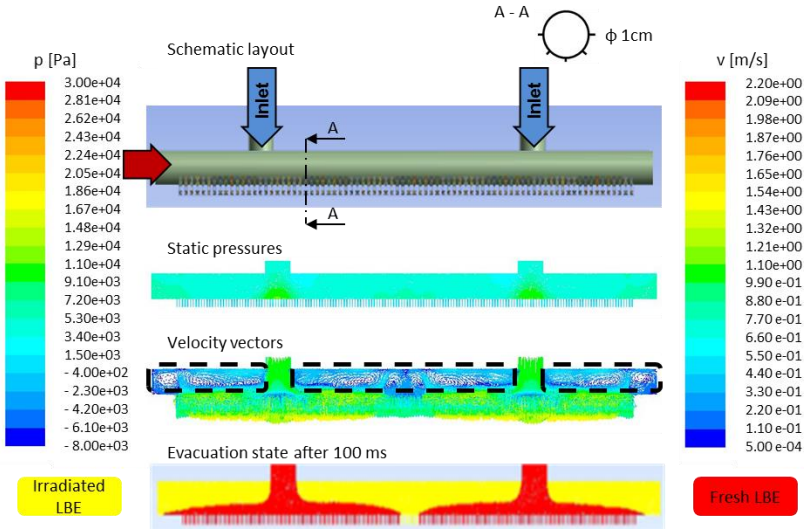


Figure 2.10: Schematic layout and CFD-analysis results (on symmetry plane) of the target design in concept 3. For consistency, pressure and velocity scales are kept the same as in Figure 2.6.

However, there were a few negative-pressure regions determined in this case, which are related to the acceleration of LBE at the entrance of few evacuation apertures. This indicates that the distribution of the evacuation-velocity vectors is still not uniform enough. Additionally, extensive recirculation zones are noticed (see dashed-line boxes on Figure 2.10). As shown on the state-of-evacuation plot of Figure 2.10, the presence of these recirculation zones inside the irradiation volume leads to slow evacuation of part of the irradiated LBE. This issue is dealt with in the next sections through more elaborate concepts.

### 2.4.3 Distributed-inlet irradiation volume

At this point, LBE recirculation in the irradiation volume is the main issue left to be solved in order to meet the 100-ms evacuation requirement. For this reason, every concept in the following sections is designed with a feeder volume (on top of the irradiation volume) that will host the recirculation zones and thereby prevent their occurrence inside the irradiation volume. In concepts 4 & 5 (Figure 2.11 & Figure 2.14), the double-inlet design of concept 3 is maintained. The inlet direction is also kept normal to the proton-beam direction, but the inlets feed the irradiation volume through the feeder volume. Feeder grids are also foreseen between the inlets and the irradiation volume. These feeder grids are designed to oppose sufficient

resistance to the inlet jets in order to uniformly distribute the LBE over the irradiation volume. This is accomplished through the use of feeder-grid apertures with small diameters.

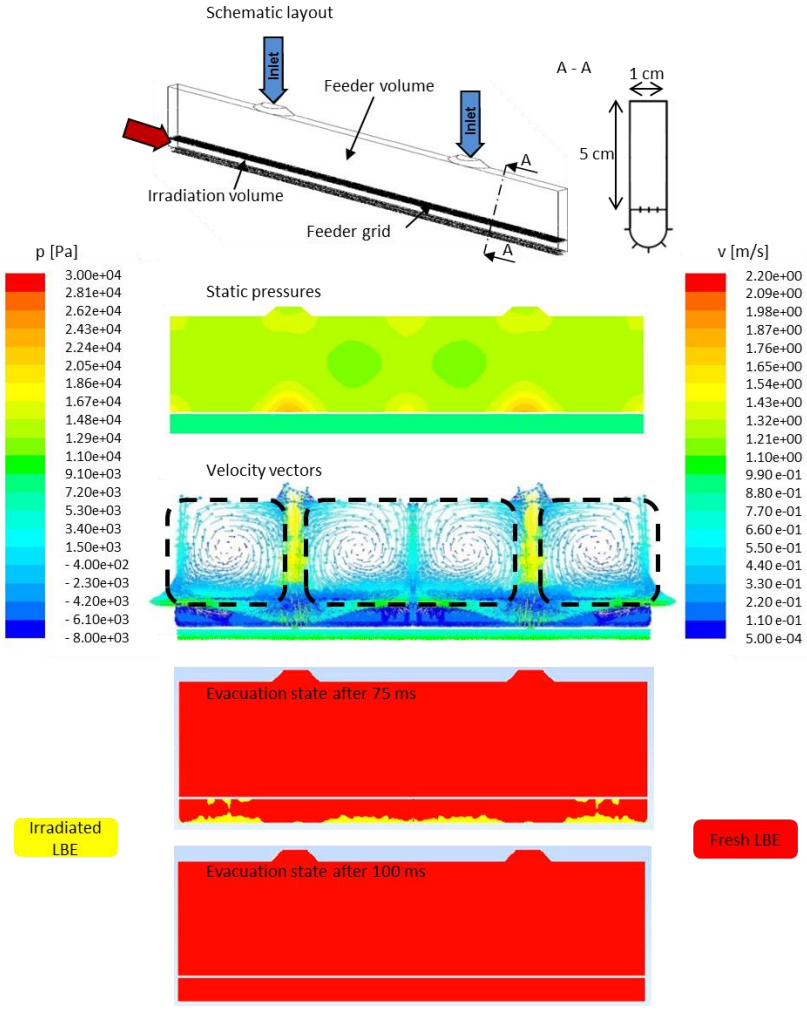


Figure 2.11: Schematic layout (half-symmetry view) and CFD-analysis results (on symmetry plane) of the target design in concept 4. For consistency, pressure and velocity scales are kept the same as in Figure 2.6.

In concept 4, a single feeder volume with a feeder grid is used. Under these conditions, preliminary simulation results (shown on Figure 2.13) show that feeder-grid apertures with radii $\leq$ 100 μm are required in order to obtain a uniform distribution over the irradiation volume. This results in a feeder grid

equipped with 10,000 apertures of 100 µm (see Figure 2.12) and a feeder volume of 5 cm in height.

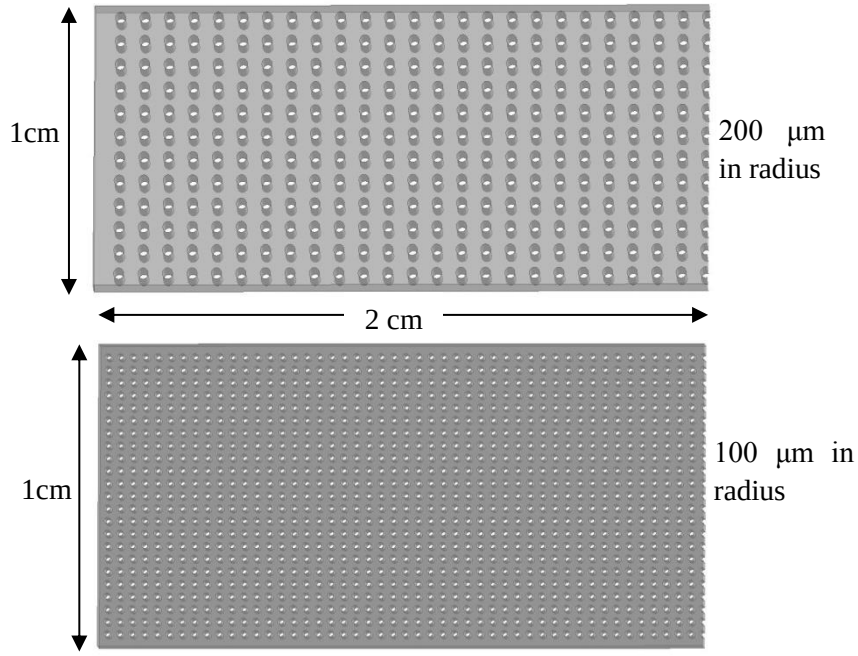


Figure 2.12: Sections of feeder grids with apertures of 200 µm and 100 µm in radius

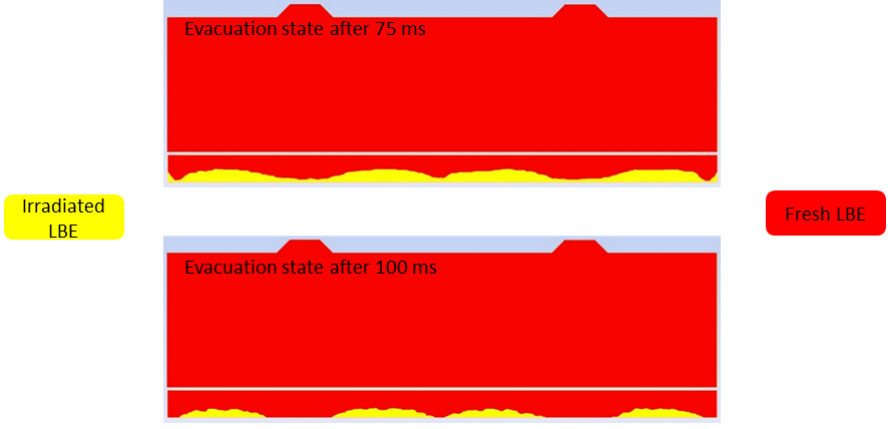


Figure 2.13: Evacuation state of concept 4, fitted with a feeder grid featuring apertures of 200 µm in radius.

Besides, to accommodate the flat feeder grid, the geometry of the irradiation volume consists of the lower half of a 20-cm long and 1-cm diameter cylinder plus a 20-cm x 1-cm x 0.5-cm parallelepiped on top.

Another concept studied (concept 5), presents two feeder grids and two feeder volumes. Each of these feeder grids is equipped with 2500 apertures of 200-μm radii and each of the feeder volumes is 2-cm high. The irradiation-volume geometry is the same as for concept 4. In both cases (concept 4 & concept 5), 1-mm thick feeder grids are used in the computation.

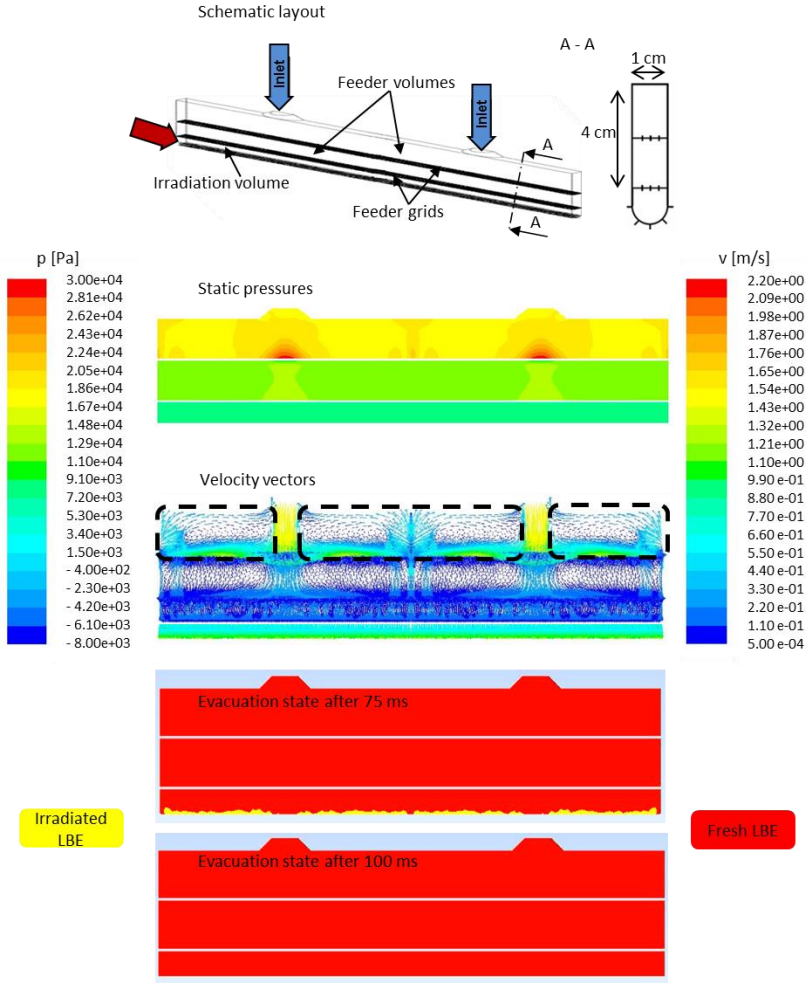


Figure 2.14: Schematic layout (half-symmetry view) and CFD-analysis results (on symmetry plane) of the target design in concept 5. For consistency, pressure and velocity scales are kept the same as in Figure 2.6.

The results of the CFD-analysis for concepts 4 and 5 are presented in Figure 2.11 and Figure 2.14, respectively. The static-pressure plots do not display any negative pressure region. In both cases, pressure differences vertically across the feeder grids are mostly constant along the proton-beam axis. This explains the uniform distribution of velocity-vectors, obtained inside the irradiation volume and at evacuation in the diffusion volume. Even though large recirculation zones have been computed (see dashed-line boxes), these have been held in the feeder volumes. Recirculation zones occurring in the feeder volume do not affect the fast evacuation of isotopes. Since the feeder

volumes are not subject to direct and intensive irradiation by the proton beam, these recirculation zones do not present a risk for occurrence of hot spots.

As a result of the absence of recirculation zones inside the irradiation volume, in both concepts 4 and 5 all the irradiated LBE is evacuated from the irradiation volume within 100 ms after a proton-pulse impact. These two acceptable solutions however imply some degree of complexity for the manufacturing, with either a doublet of feeder grids or smaller feeder-grid apertures (100 μm instead of 200 μm).

### 2.4.4 Prism-shape feeder volume

The prism-shape feeder volume concept presented here is used as an alternative to reduce the complexity of manufacturing mentioned above. It allows for larger inlets and consequently lower inlet velocity to provide the same flow rate of LBE as in concepts 4 and 5. The required inlet velocity in this concept is reduced by almost an order of magnitude compared to previous concepts, thereby reducing the strength of the inlet-jet effect. The difference between the momentum of LBE in the inlet jet and LBE in the rest of the feeder volume is thus reduced. With such a reduced inlet-jet, the design of the feeder grid can be relaxed and one single feeder grid of 200-μm radius apertures is necessary to obtain a uniform distribution of velocity vectors through the irradiation volume and at evacuation (Figure 2.15). 2500 apertures are hosted on the feeder grid which has a thickness of 1 mm, similar to concepts 4 and 5.

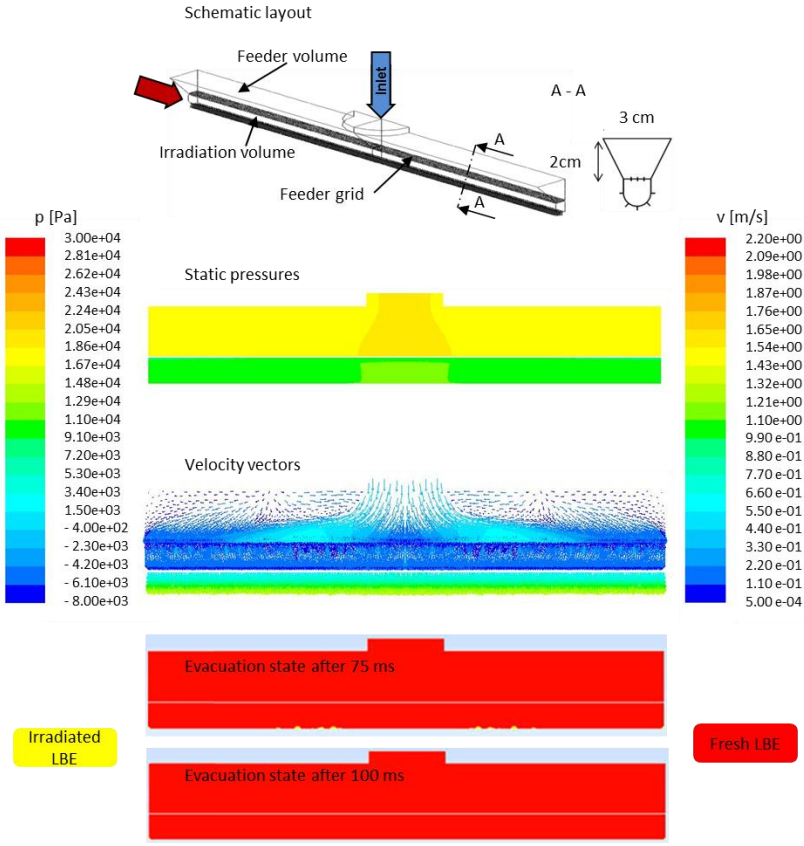


Figure 2.15: Schematic layout (half-symmetry view) and CFD-analysis results (on symmetry plane) of the target design in concept 6. For consistency, pressure and velocity scales are kept the same as in Figure 2.6.

Results of the CFD analysis are included in Figure 2.15: Velocity-vectors are uniformly distributed in the irradiation volume and at evacuation to the diffusion volume. No recirculation zone occurs in the irradiation volume and the design meets the 100-ms evacuation requirement.

## 2.5 Influence of various operational conditions

Thin feeder grids have been foreseen in the current design since this reduces the pressure drop across the grids. However, the uniform flow computed is not negatively affected by the use of thicker feeder grids that may be required for the LIEBE prototype in order to make the design more resistant to pressure waves generated by the pulsed proton beam at the test facility. Thicker feeder grids will simply have the effect of increasing the pressure drops.

The release of nuclides out of an ISOL target typically shows an exponential dependence on temperature, being more efficient at higher temperature. For this reason, the satisfactory concepts (4, 5 and 6) have been simulated with LBE data at different temperatures ranging from 500 K to 1200 K. It results from these calculations that the uniform flow of LBE in the irradiation volume is maintained over this range of temperatures for concepts 5 & 6 but not for concept 4 (see Figure 2.16). This can be explained since LBE viscosity decreases by more than a factor of two with increased temperature over this range (0.00223 Pa.s at 500 K and 0.000926 Pa.s at 1200 K [69]). More importantly, a reduction in turbulent viscosity is also observed in the inlet-jets. The lower viscosity reduces the dissipation of the inlet-jets energy to adjacent LBE by momentum diffusion. For temperatures higher than 600 K this effect disrupts the uniform flow of LBE in concept 4.

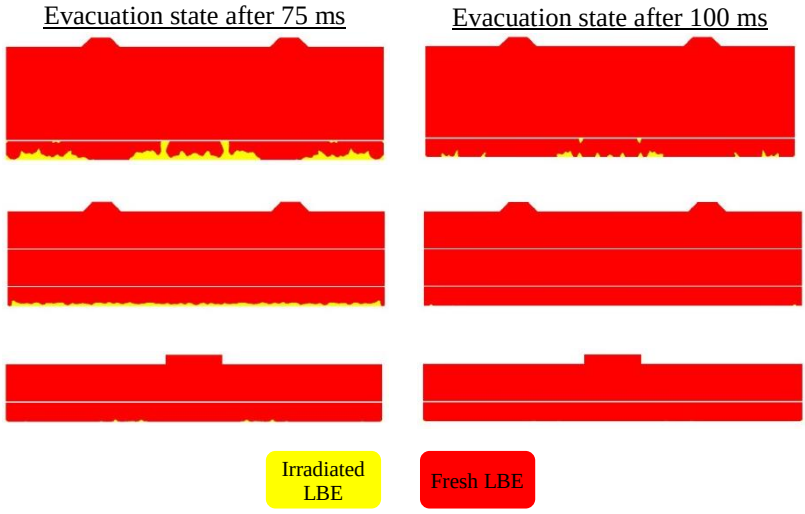


Figure 2.16: Evacuation state of concepts 4, 5 and 6 at 1200K.

The use of smaller feeder-grid apertures (100-μm radii) in concept 4 makes it more prone to clogging of the feeder grids than concepts 5 and 6. The effect of such a clogging of the feeder grid, due to impurities carried on by the inlet flow of LBE, has been assessed. Simulations were run for the three concepts (4, 5 and 6) with a partial clogging of the feeder-grid apertures. Assuming the impurities are brought in with the inlet stream, only the first feeder grid of concept 5 was partially clogged while for concepts 4 and 6 the single grid was partially clogged in the simulation. In all the concepts the clogged apertures were simulated in line with the inlets, by suppressing the apertures over a compact portion of the feeder-grid (i.e. replacing them by a

volume representing a metal piece as shown on Figure 2.17). The results have shown that even with 30% clogging of its first feeder grid, the uniform flow of LBE in the irradiation volume is maintained for concept 5. Because concepts 4 and 6 are only equipped with a single feeder grid, the uniform flow of LBE in the irradiation volume as well as the complete LBE evacuation determined in nominal conditions are already disrupted with a 10% clogging.

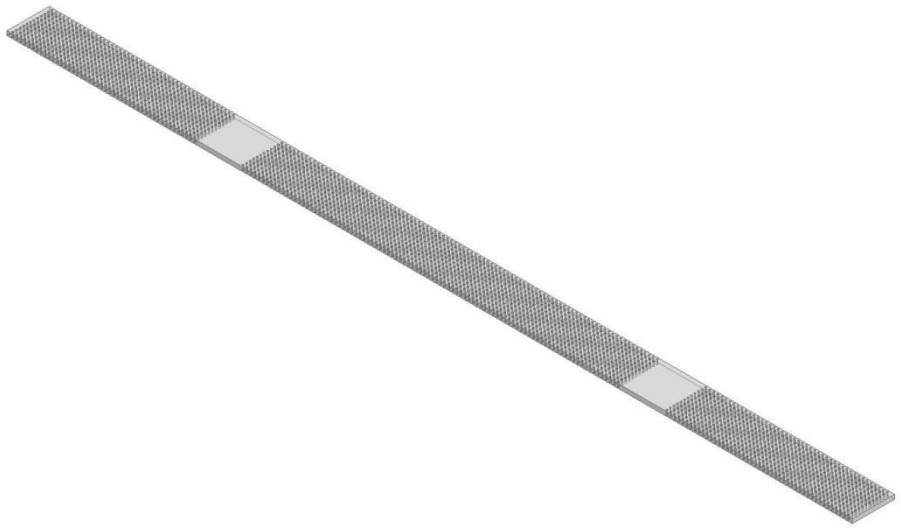

Figure 2.17: Feeder grid with 10% clogged apertures in line with the inlets.

Out of the three concepts that meet the preset design requirements, concept 5 proves to be the most robust. However, it is quite demanding in terms of complexity in manufacturing. On the other hand, concept 6 can be made more robust through the use of a filter on the feeder line. These two concepts will be prototyped for tests at CERN-ISOLDE. Because, unlike ISOL@MYRRHA the proton beam at CERN-ISOLDE is highly pulsed, specific issues improbable in CW mode and related to the pulsed-beam time structure of ISOLDE will therefore be studied for the prototype.

## 2.6 Conclusion

The CFD simulations presented in this chapter have been carried out in support of the design and optimization process of a molten-LBE target loop for the production of beams of short-lived radioactive ions at high-power ISOL facilities. A CFD analysis was used since it has been successfully compared in the past with experimental data for liquid-metal flow. This

analysis allowed us to avoid a lengthy and costly process of prototyping and testing every investigated design.

The target-design optimization reported here was conducted with the aim of a complete evacuation of the irradiated LBE from the irradiation volume within 100 ms after the impact of a proton pulse. Unforeseen issues have been revealed through simulations of the starting-case geometries proposed for the irradiation volume. The available amount of data resulting from these initial simulations provided a unique insight on the causes and potential solutions of these issues. As a result, a key feature of the optimized concepts is the need for a set of feeder volumes and feeder grids.

Three designs meeting this requirement have been developed. In each of these cases the inlet-jet effect was solved with a combination of two approaches: (1) increasing the size of inlet sections in order to reduce inlet velocities; (2) opposing one or two high-resistance feeder grids to the inlet jet. With this strategy, within a compact geometry, the jet flow with high-momentum that enters at the inlets is transformed into a uniform flow in the irradiation volume and at evacuation. Issues of low-pressure zones have been solved by avoiding unnecessary bending of the flow inside the compact geometry of the target.

Out of the three concepts that meet the pre-set design requirements, concept 5 proved to be the most robust with regards to risks of clogging.

# 3 Isotope-Release calculations – the method

The production of RIBs of nuclides away from the valley of stability is often confronted with very low production cross sections, the massive production of undesirable species and the short half-lives of the nuclides of interest. In this chapter, a computational approach to predict the release of nuclides out of a dynamic liquid metal target is presented. The chapter is divided in two parts. In the first part, an overview of the overall release of nuclides from production to delivery for an experiment is given, for current ISOL targets. The computational approach developed and used through this thesis to predict the efficiency of isotope release from production to ionization is explained in the second part. This method combines the advantages of an analytical solution with the benefits of the supporting detailed Monte Carlo (MC) calculations. One of the objectives for studying the dynamic target is to improve on the release efficiencies achievable with the current static bath liquid targets. In this objective, all the processes occurring in the target shall be properly modelled.

## 3.1 Modeling the release from the dynamic liquid target

In the ISOL technique, the isotopes of interest are produced and released from a thick target, kept at high temperature. The reaction products are subsequently ionized, extracted in the form of a RIB and mass separated. The production of RIBs of nuclei away from the valley of stability through the ISOL technique is confronted with decay losses between the production target and the experimental setup.

The figures of merit of a RIB for users are: the availability of isotope beams along with the intensity and purity. The RIB intensity $I_{RIB}$, in particles per second at an ISOL facility is typically described as the product of the in-target production rate with an overall efficiency characterizing the transport of the nuclides from their location of production to an experimental setup (see expression (3.1)) [71, 72].

$$I_{RIB} \equiv I\ \sigma\ N_{target}\ \varepsilon_{rel}\ \varepsilon_{ion}\ \varepsilon_{sep}\ \varepsilon_{transp}\ \varepsilon_{stor}\ \varepsilon_{post-acc} \tag{3.1}$$

The product of $I$ the intensity of the driver beam [particles/s], $\sigma$ the cross section for production of a nuclide [$m^2$] and $N_{target}$, the number of target atoms per unit area of beam spot [atoms/$m^2$] defines the in-target production rate. Both $\sigma$ and $I$ actually evolve with the longitudinal target depth, as a result of the stopping power and scattering in dense targets. This indicates that the in-target production rate as expressed is a simplification.

Several processes, undergone by the isotopes of interest from nuclear production until delivery to the experimental setup, contribute to the overall efficiency of the technique. These processes are:

- the release of nuclides from their production location to the ion source represented by $\varepsilon_{rel}$,
- the ionization of the nuclides in preparation of an electromagnetic transport represented by $\varepsilon_{ion}$,
- the electromagnetic mass separation of the ions represented by $\varepsilon_{sep}$,
- the ion-optical transport of the selected ions through the beam line system represented by $\varepsilon_{transp}$,

In addition, if necessary the ion beam can be stored, cooled, bunched of post-accelerated. Note that no storage or post-acceleration is currently foreseen for ISOL@MYRRHA.

While the ionization process efficiency varies between 0.1 % and 90 %, the efficiencies of all the processes that follow ionization would typically be above 10 %. In contrast, the efficiency of nuclide release from the target to the ion source is often as low as $10^{-6}$ or less [72]. In some cases, this step can fully prevent the production of a RIB, even at high temperatures and with in-target production rates of the order of $10^{11}$ $s^{-1}$. Therefore, the main research goal of this work is to improve the efficiency of this crucial step in the dynamic molten-metal target.

At a specific facility, $N_{target}$ and $\varepsilon_{rel}$ are the parameters to be tuned in order to optimize the design of a certain target. Together, these two parameters constitute a figure of merit for the target that ought to be the aim of the target design and optimization. Among others, $N_{target}$ depends on the length of the target.

In current ISOL targets, the produced nuclides undergo two processes during their release from the target to the ion source. These processes are: the diffusion from the target material inside which the nuclides are produced and the following effusion in the target container and transfer line. In this target there is an extra process prior to the two mentioned, consisting of the evacuation of the nuclides from the irradiation volume to the release volume. All three processes contribute to $\varepsilon_{rel}$ and are to be accounted for in optimizing the release of nuclides out of the target. Note that these processes are often linked and it is therefore not possible to optimize them independently.

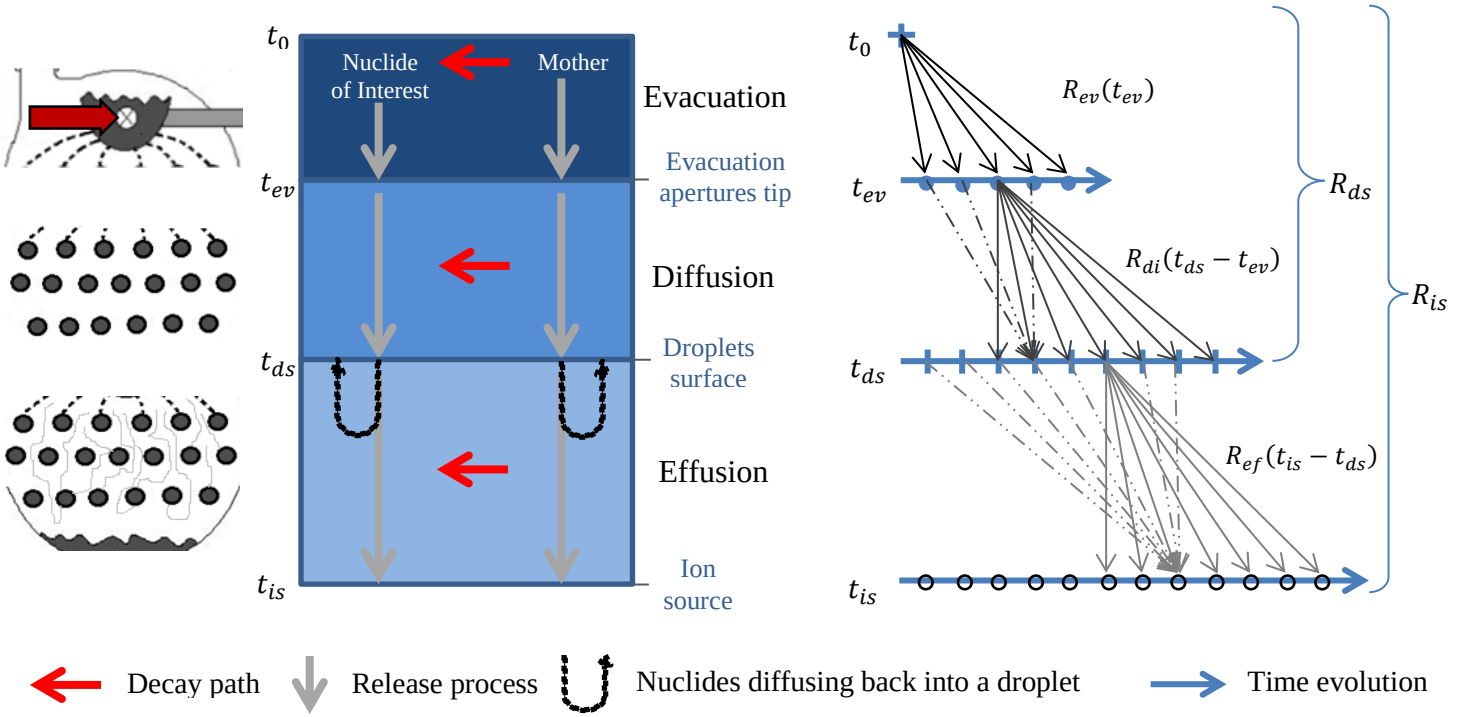


Figure 3.1: Release model for the dynamic molten metal target. $\mathbf{t_0}$ represents the creation time of nuclides in the irradiation volume, $\mathbf{t_{ev}}$ is the time of evacuation of nuclides into droplets, $\mathbf{t_{ds}}$ is the time of arrival of nuclides at the droplets surface and $\mathbf{t_{is}}$ is the time of arrival of nuclides at the ion source.

The sketch on Figure 3.1 illustrates the method developed and implemented to model the release of nuclides out of the target. Each of the processes contributing to $\varepsilon_{rel}$ is modelled separately to capture its specific features.

For each process, the probability density function (***pdf***) that a nuclide spends a specific time duration in the process is modelled and expressed analytically. Analytical descriptions of the ***pdf***s for evacuation diffusion denoted $R_{ev}$ and $R_{di}$ are then convoluted into a ***pdf*** for arrival of nuclides at the droplets surface indicated by $R_{ds}$. This function is in turn convoluted with the analytical description of the effusion ***pdf*** denoted $R_{ef}$ to obtain an overall delay-time distribution indicated by $R_{is}$. The convolution is a mathematical operation on two functions that gives the integral of the pointwise multiplication of the two initial functions. In probability [73], it defines the density function of two independent random variables. In isotope-release calculations for classical ISOL targets [74-76], the convolution operation has been proposed to combine diffusion and effusion distributions.

At most ISOL facilities the pulse length is in the order of few tens of microseconds ( ~2 µs at CERN-ISOLDE and 200 µs at ISOL@MYRRHA). In comparison, the complete evacuation time and the half-life of the isotopes of interest are of the order of 100 ms. Therefore the effect of either radioactive decay or evacuation of isotopes is negligible on this time scale. It can be considered that all the nuclides are still present in the irradiation volume at the end of the proton pulse. As illustrated on Figure 3.1, $R_{is}$ describes the release of nuclides after a single proton pulse.

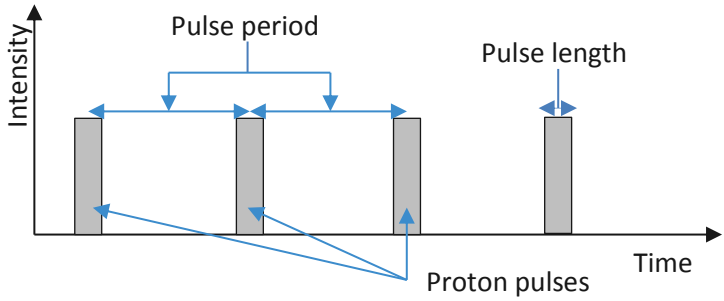


Figure 3.2: Time structure of a proton beam.

Multiple proton pulses are typically directed on a target for RIB production. In case the pulse period at a facility is very large, compared to either the mean release time or the half-life of the isotope of interest, the release curve

for multiple pulses will simply be a repetition in time of the single-pulse release curve (i.e. with a different value of $t_0$, Figure 3.1). This will be the case for $^{177}$Hg ($t_{1/2}$ = 118 ms) isotopes produced at CERN-ISOLDE which has a super-cycle period of 14.4 s, composed of several 1.2-s spaced pulses. Recall that this is the facility where the prototype of this loop-type molten metal target will be tested.

In contrast, at ISOL@MYRRHA the pulse period being 2 ~4 ms. This pulse period is significantly smaller than both the mean release time and the half-life of the isotope of interest. Therefore, convolution operations have to be carried out between the beam structure and the single-pulse release curve in order to obtain the release curve for multiple pulses. Indeed, in this case, the nuclides of interest would pile up in the irradiation volume at each pulse until the depletion effect of radioactive decay and LBE evacuation compensates the buildup effect of the quasi continuous production of these nuclides. A dynamic equilibrium concentration of the nuclides of interest will then be reached in the irradiation volume, depending on the half-life, the LBE flow rate and pulse period.

### 3.1.1 Evacuation of the freshly-irradiated LBE

The irradiation chamber is designed to operate under a constant flow rate of LBE (see chapter 2) determined by its volume $V_{irr}$ and the required duration $\Delta t_{fev}$ for full-evacuation of irradiated LBE. Within any element of time $[t\,;t+dt]$ with $t_0 \leq t < t_0 + \Delta t_{fev}$, the amount of any produced nuclide that exits the irradiation volume is proportional to the flow rate of LBE and defined as $\frac{CV_{irr}}{\Delta t_{fev}}dt$. Here, $t_0$ represents the time right at the end of a proton pulse and $C$ is the average concentration of a specific nuclide in the irradiation volume after arrival of a proton pulse.

In the following, the total amount of a specific nuclide present in the irradiation volume at $t_0$ is called the "initial amount" of the nuclide. Since the volume of irradiation is fully evacuated in a time period $\Delta t_{fev}$, the fraction of the initial amount of any nuclide that is evacuated within the time period $[t_{ev}\,;t_{ev}+dt]$ with $t_0 \leq t_{ev} < t_0 + \Delta t_{fev}$ is:

$$dEvac = \frac{1}{C_i V_{irr}} \times \frac{C_i V_{irr}}{\Delta t_{fev}} dt_{ev} = \frac{1}{\Delta t_{fev}} dt_{ev}, \qquad t_0 < t_{ev} \leq t_0 + \Delta t_{fev} \tag{3.2}$$

The subscript $_{ev}$ used on the time parameter relates to the evacuation time of a nuclide. Because the irradiation volume is fully evacuated within $\Delta t_{fev}$, for a nuclide present in the irradiation volume at $t_0$, the probability of being

evacuated from the irradiation volume within a time period $[t_{ev}\,; t_{ev} + dt]$ is zero if $t_{ev} \geq t_0 + \Delta t_{fev}$. Thus, the ***pdf*** for the process of nuclide evacuation from the irradiation volume can be derived as:

$$R_{ev}(t_{ev}) = \frac{dEvac}{dt_{ev}} = \begin{cases} \dfrac{1}{\Delta t_{fev}} \;, & t_0 < t_{ev} \leq t_0 + \Delta t_{fev} \\ 0, & t_{ev} \leq t_0 \; or \; t_{ev} \geq t_0 + \Delta t_{fev} \end{cases} \qquad (3.3)$$

Also known as the delay time distribution, in this case for the irradiated-LBE evacuation process, this density function is constant while evacuation is occurring and drops to zero afterward (Figure 3.3).

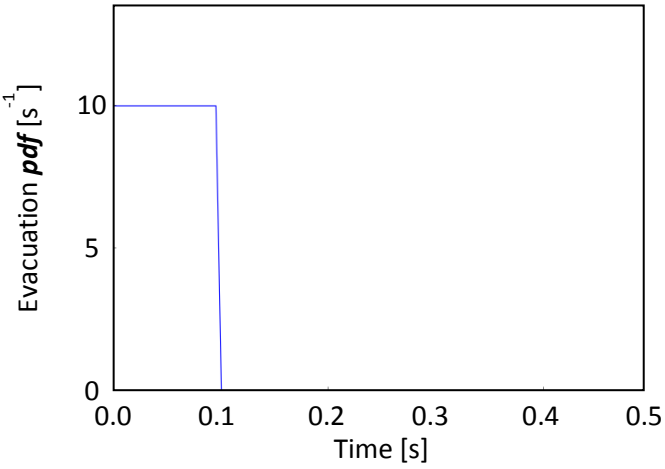


Figure 3.3: Evacuation pdf.

Once evacuated from the irradiation volume, the nuclides diffuse out of LBE droplets falling in the release volume. This process is the subject of next section.

### 3.1.2 Diffusion

In current liquid targets, diffusion is commonly the main delaying process between the production of nuclides in the target and arrival at the ion source. Diffusion is the process by which particles of matter (liquids, gases, or solids) are transported from one region of a system to another as a result of random molecular motion. In case of dissolved substances, this random motion results in a net transfer of solute particles from regions of higher to those of lower concentration. In gases, diffusion coefficients are typically around $10^{-5}$ $m^2s^{-1}$. In liquids, diffusion coefficients are about $10^{-9}$ $m^2s^{-1}$. In solids, diffusion is usually even slower [77, 78]. The release of nuclides out of this loop-target takes advantage of this faster diffusion in the liquid

droplets produced after evacuation of the irradiated LBE. Whence the need for a thorough understanding and modeling of diffusion in order to estimate and improve the efficiency of this process.

#### *3.1.2.1 Mechanisms of diffusion in liquids*

Molecules and atoms in a liquid randomly move and interact with each other, which complicates the understanding of the mechanisms of diffusion in liquids. Early descriptions of diffusion in liquids were based on the idea that matter rearranges after surmounting a potential energy barrier [79]. In this description, it is assumed that the diffusing atom/molecule must have enough energy at some point in time, to move its neighbors. Because of inconsistencies between these activation-energy based models and experiments [80], a free-volume based description was proposed [81, 82]. The latter is based on the idea that in a liquid, molecules or atoms are normally closely surrounded by other atoms or molecules preventing their motion. Still, because these atoms/molecules are also in constant Brownian motion with a frequency of the order of $10^{12}$ - $10^{13}$ Hz [83], random fluctuations may momentarily create an adjacent vacancy large enough for a step motion of the diffusing species [84]. It is thus assumed in a free volume based description that in liquids, free volume is constantly being redistributed. This description was later extended [84, 85] in order to include the fact that the diffusing atom/molecule first needs to break free from the rest of its neighbors before it can make the diffusion step.

#### *3.1.2.2 Fundamentals of diffusion*

This section presents the relevant laws and hypothesis required for describing the transport of nuclides through the diffusion step in a liquid droplet. Diffusion in matter is a common phenomenon that has amply been studied in literature [78, 86-91]. The mathematical formalism to describe diffusion was pioneered by Fick [92]. In isotropic substances, this theory derives from the initial hypothesis that the rate of transfer of diffusing species through a unit section of the substance is proportional to the concentration gradient normal to this section. This hypothesis translates mathematically in the following expression, known as Fick's first law of diffusion:

$$F = -D\frac{\partial C}{\partial x}, \tag{3.4}$$

where $F$ is the rate of transfer per unit area of section, $C$ the concentration of diffusing nuclide, $x$ the space coordinate normal to the section and $D$ is the

diffusion coefficient. In our case, because of their limited production rates, the produced isotopes are in a dilute solution with LBE, which means that the diffusion coefficient can reasonably be considered constant in space [86]. Combined with equation (3.4), mass-conservation law applied to an elementary volume results in a second fundamental equation for diffusion. This is the Fick's second law of diffusion, expressed as follows:

$$\frac{\partial C}{\partial t} = \left[\frac{\partial}{\partial x}\left(D\frac{\partial C}{\partial x}\right) + \frac{\partial}{\partial y}\left(D\frac{\partial C}{\partial y}\right) + \frac{\partial}{\partial z}\left(D\frac{\partial C}{\partial z}\right)\right], \tag{3.5}$$

with $x$, $y$, and $z$ the space coordinates and $t$ the time coordinate. Other forms of the second law can be obtained by transformation of coordinates. Thus, the equation corresponding to diffusion in spherical droplets follows by putting

$$x = r\sin\theta\cos\emptyset\,, \tag{3.6}$$

$$y = r\sin\theta\sin\emptyset\,, \tag{3.7}$$

$$z = r\cos\theta\,, \tag{3.8}$$

where $r$, $\theta$ and $\emptyset$ are respectively the radial coordinate, the zenith angle and the azimuthal angle. Considering the diffusion coefficient in the dilute solution as constant in space, Fick's second law of diffusion can be written in spherical coordinates as:

$$\frac{\partial C}{\partial t} = D\left[\frac{1}{r^2}\frac{\partial}{\partial r}\left(r^2\frac{\partial C}{\partial r}\right) + \frac{1}{r^2\sin\theta}\frac{\partial}{\partial\theta}\left(\sin\theta\frac{\partial C}{\partial\theta}\right) + \frac{1}{r^2\sin^2\theta}\frac{\partial^2 C}{\partial\emptyset^2}\right]. \tag{3.9}$$

Because production rates only gradually change with space, $C$ can be considered initially uniform within a 200-µm radius droplet. Also, as the droplet fall in vacuum, the rate of desorption per unit area should be uniform over the droplet surface. Spherical-symmetry conditions can therefore be assumed, allowing the restriction of the case to a pure radial-diffusion problem. Equation (3.9) is then simplified to:

$$\frac{\partial C}{\partial t} = D\left(\frac{\partial^2 C}{\partial r^2} + \frac{2}{r}\frac{\partial C}{\partial r}\right). \tag{3.10}$$

The solution of this equation under relevant initial and boundary conditions is the subject of next section.

### *3.1.2.3 Modeling diffusion*

Provided the constant diffusion coefficient stated earlier, solutions to the partial differential diffusion equation can in general be found for different initial and boundary conditions [86]. Such a solution can be found in two different forms. Solutions presented in the form of a series of error functions or related integrals are meant for numerical evaluations of diffusion yields in the early stages of diffusion. When converging solutions at later stages of diffusion are of interest, they are more suitably presented in the form of a trigonometrical series. This second presentation of the solution, obtained through the method of separation of variables, is adopted in this work.

On putting $u = rC$, equation (3.10) becomes

$$\frac{\partial u}{\partial t} = D\frac{\partial^2 u}{\partial r^2}. \tag{3.11}$$

Obtaining a particular solution to equation (3.11) requires setting the initial and boundary conditions of the problem. The gradual change in space of the production rates induces a fairly uniform initial concentration of a specific nuclide in a 200-μm radius droplet. The initial condition of the diffusion problem is therefore set to:

$$u = rC_i\,, \qquad t = 0\,, \qquad 0 < r < a \tag{3.12}$$

At the surface of the droplet $r = a$, the boundary condition applied, the constant surface concentration $C_s$ is expressed as:

$$u = aC_s\,, \qquad r = a\,, \qquad t > 0 \tag{3.13}$$

This condition signifies that upon reaching the surface of the droplet, diffusing nuclides are desorbed nearly immediately. Extensive studies on diffusion of radioisotopes from several irradiated targets [21, 87, 93, 94] indicate this is a suitable condition. The applicability of the constant surface concentration in this case can be checked by comparing the mean diffusion time of nuclides in the droplets to their average residence time at the surface of the droplets. The mean diffusion time $\langle \Delta t_{di} \rangle$ for Cd atoms out of a 200-μm radius sphere of Pb with constant surface concentration is given by [87]:

$$\langle \Delta t_{di} \rangle = \frac{a^2}{15\,D} = 0.68\ s \tag{3.14}$$

The diffusion coefficient of Hg in Pb-Bi was not found in literature. Instead, the diffusion coefficient of the chemical equivalent Cd in Pb, 3.9 $10^{-9}$ $m^2/s$ at

723 K [95] is used in this work. Similar values of diffusion coefficients have been reported for several solutes (Au, Ag, Cu, Sn) in Pb [95, 96].

Based on its exponential dependence on temperature [74, 97, 98], the mean surface residence time $\tau_a$ of Hg on Pb was determined as:

$$\tau_a = 2.4\ 10^{-15} \exp\left(\frac{11605 \Delta H_a}{T}\right) \tag{3.15}$$

where $\Delta H_a = 0.685$ eV is the adsorption enthalpy taken from [99] for Hg on Pb, and $T$ is the temperature in [K]. Applying this, one obtains mean surface residence time of 4.75 $10^{-8}$ s at 473 K and 2.16 $10^{-11}$ s at 873 K. The application of the constant-surface-concentration boundary-condition is justified by the several orders of magnitude between $\tau_a$ and $\langle \Delta t_{di} \rangle$.

Applying these boundary conditions to solve equation (3.11), the following solution is obtained [86]:

$$\frac{C - C_i}{C_s - C_i} = 1 + \frac{2a}{\pi r} \sum_{m=1}^{\infty} \frac{(-1)^m}{m} \sin\frac{m\pi r}{a} \exp\left(-\frac{m^2 \pi^2 D}{a^2} t\right) \tag{3.16}$$

The amount per unit area of diffusing substance that has left the droplet at any time $t$ is defined as [86]:

$$\frac{dM(t)}{dt} = -\left(D \frac{\partial C}{\partial r}\right)_{r=a} \tag{3.17}$$

The ratio of $M(t)$ to $M(\infty)$ the corresponding amount at infinite time determines the fraction of diffusing nuclides that have left a droplet. On substituting for $C$ the expression obtained from equation (3.16) one obtains [86, 89]:

$$\frac{M(t)}{M(\infty)} = 1 - \frac{6}{\pi^2} \sum_{m=1}^{\infty} \frac{1}{m^2} e^{-\frac{m^2 \pi^2 D}{a^2} t} \tag{3.18}$$

For any time period $\Delta t_{di}$ elapsed since the start of diffusion in the droplet, the fraction of the initial amount of a nuclide still remaining inside the droplet is then:

$$f(\Delta t_{di}) = \frac{6}{\pi^2} \sum_{m=1}^{\infty} \frac{1}{m^2} e^{-\frac{m^2 \pi^2 D}{a^2} \Delta t_{di}} \tag{3.19}$$

The fraction of nuclide diffusing out through a droplet surface in a time period $[\Delta t_{di}\ ; \Delta t_{di} + dt]$, called $Diff(\Delta t_{di})$ is then:

$$Diff(\Delta t_{di}) = f'(\Delta t_{di})\, dt = \frac{6D}{a^2} \sum_{m=1}^{\infty} e^{-\frac{m^2\pi^2 D}{a^2}\Delta t_{di}} \times dt \qquad (3.20)$$

Eventually, the droplets and the nuclides still contained inside reach the surface of the LBE bath at the bottom of the release chamber. This LBE volume is subsequently pumped out of the release chamber. It then flows for few seconds in the piping and through the heat exchanger and the pump. For the short-lived isotopes this typically represents more than 10 half-lives and indicates a nearly zero probability of survival to decay in the rest of the loop. Thus, the main contribution of diffusion to the release of nuclides occurs essentially while the droplets are still falling in the release volume. For this reason, diffusion is only considered in the droplets and the ***pdf*** of a nuclide reaching the surface of droplet after diffusing for a period $\Delta t_{di}$ can be defined as:

$$R_{di}(\Delta t_{di}) = \begin{cases} \dfrac{6D}{a^2} \displaystyle\sum_{m=1}^{\infty} e^{-\frac{m^2\pi^2 D}{a^2}\Delta t_{di}} , & \Delta t_{di} < \Delta t_{fall} \\ 0 , & \Delta t_{fall} \leq \Delta t_{di} \end{cases} , \qquad (3.21)$$

with $\Delta t_{fall}$ the time it requires a droplet to fall from an evacuation-aperture tip to the bath surface at the bottom of the release volume.

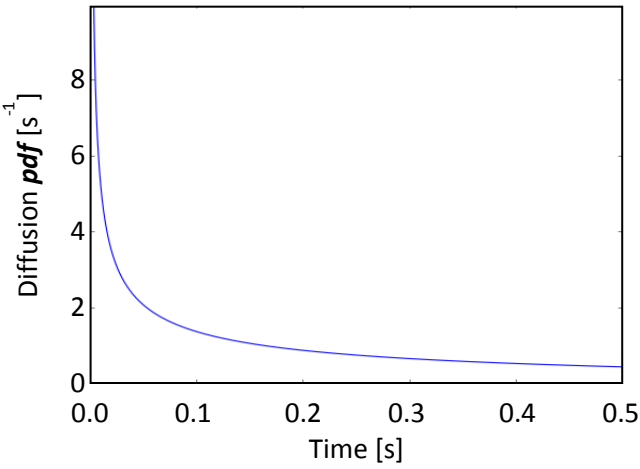


Figure 3.4: Diffusion pdf for droplets of 200 µm in radius. The second portion of expression (3.21) is not represented.

This delay time distribution for diffusion (Figure 3.4) is convoluted with $R_{ev}$ in the following section, to model the combined delay induced by the evacuation and diffusion processes.

### *3.1.2.4 Delay time distribution at droplets surface*

The separate ***pdf***s for the evacuation and diffusion processes can be convoluted in the following combined delay time distribution for a nuclide reaching at $t$ the surface of the droplet in which it was evacuated:

$$R_{ds}(t_{ds}) = \int_{t_{ev\,min}}^{t_{ev\,max}} R_{ev}(t_{ev}) \times R_{di}(t_{ds} - t_{ev}) dt_{ev} \tag{3.22}$$

In equation (3.22), $R_{ev}(t_{ev}) \times R_{di}(t - t_{ev}) dt_{ev}$ can be interpreted as the probability density of a nuclide to reach the droplet surface at $t$, knowing that the nuclide was evacuated from the irradiation volume in the interval $[t_{ev}, t_{ev} + dt_{ev}]$, and consequently spent $t - t_{ev}$ in the diffusion process. The integral $R_{DS}$ can thus be viewed as the summation of this probability over all the possible evacuation times of a nuclide that can lead to this nuclide reaching at time $t$, the surface of the droplet in which it was evacuated. The upper limit of the integration $t_{ev\,max}$, is $t_{ds}$ the arrival time of the nuclide at the droplet surface as long as the freshly-irradiated LBE is not fully evacuated. Also, only droplets formed before $t_0 + \Delta t_{fev}$ contain short-lived nuclides that can contribute to populating a droplet surface. $t_{ev\,max}$ is thus defined as:

$$t_{ev\,max} = \begin{cases} t_{ds} & , \quad t_0 \le t_{ds} \le t_0 + \Delta t_{fev} \\ t_0 + \Delta t_{fev}, & t_0 + \Delta t_{fev} \le t_{ds} \le t_0 + \Delta t_{fev} + \Delta t_{fall} \end{cases} \tag{3.23}$$

The lower limit on the other hand is defined by the fact that once the droplets merge with the release-volume-bath, the nuclides that are still contained in cannot contribute to populating a droplet surface. In this model, the potential contribution from the release-volume bath is ignored and $t_{ev\,min}$ is defined as:

$$t_{ev\,min} = \begin{cases} t_0 & , \quad t_0 < t_{ds} \le t_0 + \Delta t_{fall} \\ t_{ds} - \Delta t_{fall}, & t_0 + \Delta t_{fall} \le t_{ds} \le t_0 + \Delta t_{fall} + \Delta t_{fev} \end{cases} \tag{3.24}$$

Neither $t_{ev\,max}$ nor $t_{ev\,min}$ is defined for $t_{ds} > t_0 + \Delta t_{fall} + \Delta t_{fev}$ since all the droplets containing short lived nuclides have already merged with the release-volume-bath.

In light of this, the delay time distribution at droplets surface can be evaluated. From this point on, we will consider the end of a proton pulse as the origin of time, i.e. $t_0 = 0$. The distributions for arrival of Hg isotopes at the droplets surface are shown on Figure 3.5. The distributions start from zero initially. In both cases the curve rises fast, mostly due to evacuation of irradiated LBE (shown in yellow on the inserts). A smaller contribution to

this rise comes from diffusion of isotopes to the droplets surface. In case $\Delta t_{fall} > \Delta t_{fev}$, after full evacuation, diffusion is the only process populating the droplets surfaces with nuclides. This explains the shape of the second portion of the curve. Then, the first freshly-irradiated-LBE droplets merge with the bath below and are pumped away. This is the reason for the steeper slope of the third section. In case $\Delta t_{fev} > \Delta t_{fall}$, the initial rise of the curve stops when the first freshly-irradiated-LBE droplets merge with the bath at the bottom of the release volume. It is followed by a second portion where the steady evacuation of irradiated LBE compensates the effects of diffusion and the merger of droplets with the release volume bath. This flat portion of the curve stops as soon as all the irradiated LBE is evacuated. The shape of the curve on the third portion is thus defined only by diffusion and the merger of droplets with the bath. Eventually, in both cases, all the droplets formed with irradiated LBE will merge with the bath at the bottom of the release volume and get pumped away, explaining that both curves drop to zero.

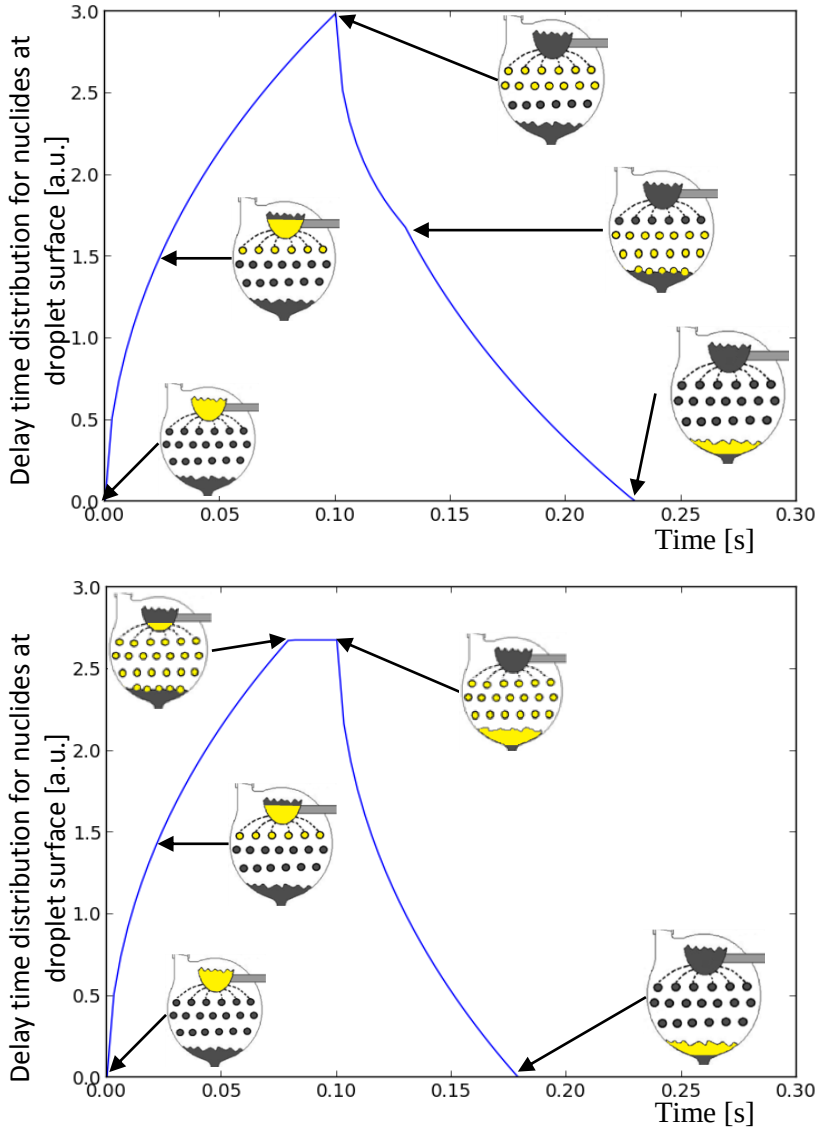


Figure 3.5: Delay time distribution for nuclides reaching the surface of the droplet in which they were evacuated. The top picture corresponds to the case $\Delta \mathbf{t_{fall}} > \Delta \mathbf{t_{fev}}$ and the bottom picture represents the case $\Delta \mathbf{t_{fev}} > \Delta \mathbf{t_{fall}}$.

### 3.1.3 Effusion

Upon reaching the boundaries of the diffusing medium, nuclides undergo another transport process called effusion [74, 98, 100-104]. This section describes the mechanism of effusion as well as its basics. A numerical solution based on Monte Carlo modeling is presented. The modeling of

effusion as implemented in this work is also described, which includes fitting the output of the Monte Carlo simulation with an analytical model.

#### *3.1.3.1 Mechanisms of effusion*

Effusion is the random migration of atoms or molecules in the vacuum volumes of a target and a transfer line. Due to a very low pressure, these volumes are under rarefied-gas conditions and the flow behavior cannot be treated with the continuum-media assumption. Indeed, different flow regimes can be distinguished according to the value of the Knudsen number of the system [105, 106].

$$Kn = \frac{\lambda}{L_c} \tag{3.25}$$

where $\lambda$ is the molecular mean free path and $L_c$ is the characteristic scale of the gas flow often taken as the transversal dimension of the flow section. From the kinetic theory of gases, using the Maxwell-Boltzmann distribution and the ideal gas law, $\lambda$ is given by:

$$\lambda = \frac{k_B T}{\sqrt{2}\pi d^2 p}, \tag{3.26}$$

where $d(m)$ is the molecular diameter in meters, $k_B$ is the Boltzmann constant, $T(K)$ is the temperature and $p(Pa)$ is the pressure. For a target ($L_c \sim 1$ cm) at a pressure of ~5 $10^{-5}$ Pa, a temperature above 400 K, and a molecular diameter of ~1.5 Å [107], a Knudsen number above $10^3$ is obtained which classifies the effusion flow in typical ISOL targets as a molecular flow. This indicates that the collisions of the atoms or molecules with the walls of the target and transfer line occur much more frequently than the collisions between atoms or molecules. As a result, atoms or molecules move independent of each other.

Approaches to analytically describe the effusion process, albeit each with different limitations, have been proposed in literature [94, 100, 102, 108]. In reference [102], effusion is described with diffusion models resulting from Fick's laws. This description implies the definition of a diffusion coefficient for the effusion process, the value of which was determined by fitting the model to experimental data. Such a description is not applicable for the design and optimization of new targets since it requires experimental data on that particular target. A different approach to analytically describe the effusion process is proposed in [94, 100, 108]. This approach is based on the vacuum-theory description of the flow rate through cylindrical tubes. This

very simplified geometry is not representative of the internal structure of ISOL targets which are too complex for analytical formulation and, therefore, require numerical solutions.

Depending on the value of the Knudsen number of the system, different numerical schemes have been proposed for rarefied gas flow calculations. For a system in the transition regime, $0.01 < Kn < 1$, the Direct Simulation Monte Carlo (DSMC) method [109, 110] is typically applied. Recently, an extension of the Test Particle Monte Carlo (TPMC) method has been proposed to solve transition-regime flow problems as well [111]. For a system in the free molecular flow regime, $Kn > 10$ as in this case, two main approaches are available. The first is a deterministic approach called Angular Coefficient (AC) method [112]. In this method the boundary defining the gas flow is subdivided into a network of surface elements, depending on their relative orientations defined by angular coefficients. The second approach is the probabilistic TPMC method [113, 114] by which virtual test particles from a statistically significant ensemble are tracked from the gas source to a pumping location.

The AC method requires meshing of the gas-flow boundaries and the creation of a matrix to store angular coefficients defining the view factor of each mesh element with respect to all the other elements. Ensuring a mesh-independent result of a calculation then generally requires a large-memory especially for complex geometries with many curved surfaces. In contrast, in the TPMC method, only the coordinates of the vertices and normal vectors of the surfaces bounding the gas flow need to be stored. In addition, because no meshing is required on planar surfaces in the TPMC method [115], its memory requirement is significantly lower than that of the AC method. Besides, the TPMC method is more easily parallelized and applicable to time-dependent calculations. It also offers the possibility to define many different gas-surface interaction models, representative of different surface conditions. However, with the TPMC method, long computations can be required in case of complex geometries.

For these reasons, the TPMC method was applied in this work through the use of the Molflow+ code [116]. The TPMC method implemented in the code follows the algorithm described in Figure **3.6**.Since molecular-flow conditions are assumed in the code, intermolecular collisions are discarded and the trajectories of particles are rectilinear between two points of interaction with the system walls. The test particles representing the effusive atoms or molecules are individually and sequentially desorbed according to

the space and time distributions set by the user. Upon generation of a test particle, the emission direction of the particle is sampled from a user-defined angular distribution. This distribution can be uniform, or follow a cosine law. In the cosine law, the zenithal and azimuthal angles of the emission direction, denoted $\theta$ and $\emptyset$ are defined as [115]:

$$\theta = \cos^{-1}\left(\sqrt{1 - rnd}\right) \tag{3.27}$$

$$\emptyset = 2\pi . rnd \tag{3.28}$$

where $rnd$ is a random number generated uniformly between 0 and 1, with a period of $(2^{19937} - 1)$ [115]. Based on the sample emission direction of the particles the location of the next collision with the boundaries of the computational domain is determined. From the collision location the flight duration is determined and stored among other parameters. The sticking probability defined by the user on the surface on which the particle has collided, is used by the code to determine if the tracking of the particle should be terminated or continued. After each collision with the walls of the system, the speed and direction of effusing atoms are generated according to statistical distributions. The speed distribution follows the Maxwell-Boltzmann distribution or its average value [117], while the distribution of the re-emission direction can be described with different models [101, 103] depending on the system-walls surface-structure.

The steps in Figure **3.6** are repeated for several hundred thousands of test particles. The stored flight duration all the simulated particles can then be used to construct the effusion ***pdf***. Some basic concepts on modeling particle-wall interactions in rarefied gas flow calculations are outlined below.

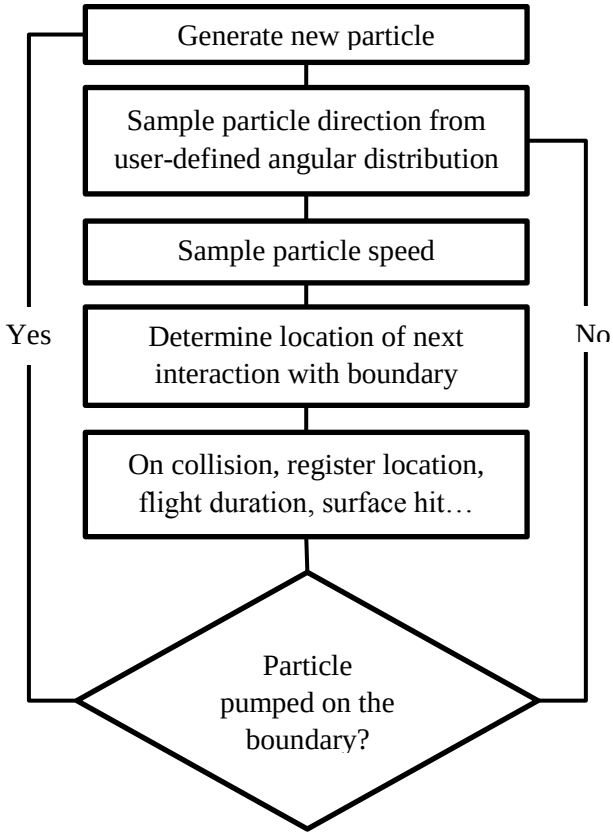


Figure 3.6: Implementation algorithm for TPMC in Molflow+, information from [115].

### *3.1.3.2 Fundamentals of effusion – Accounting for sticking times*

Upon interaction with a surface, atoms or molecules can undergo sorption phenomena by which they get temporarily attached on the sorbent surface. Two separate sorption mechanisms can be distinguished: adsorption and absorption [118, 119]. While absorption means that the atom or molecule is dissolved by or permeates the structure of the sorbent, adsorption is a surface interaction and is generally a faster process. Sorption effects apply to both solid and liquid surfaces, and under certain energy and temperature conditions, the adsorbate can re-desorb.

Depending on the interaction energy between the surface atoms and gas particles, the binding can be considered weak or strong. This differentiation stems from the nature of the interaction which can be either physical or chemical. The process is termed physisorption when based on physical

interactions and chemisorption when based on chemical interactions. Physisorption is due to weak Van der Waals or electrostatic attractive forces. It is an exothermic process and the adsorbate can interact either with a single adsorbent atom or diffusely with the adsorbate substrate. In contrast, when covalent bonds between adsorbate and adsorbent atoms are involved, as in chemisorption, larger energies are involved.

The nature and strength of the adsorption interaction is reflected in the rate of re-desorption of adsorbates through the desorption activation energy. A mean sticking time $\tau_s$ before re-desorption of adsorbate is expressed by the Frenkel Equation [120, 121]:

$$\tau_s = \tau_0 \exp(E_{des}/k_B T_s) \tag{3.29}$$

where the pre-exponential factor $\tau_0$ is the vibration period of adsorbent surface atoms, $E_{des}$ is the activation energy for desorption and $T_s$ is the surface temperature.

#### *3.1.3.3 Fundamentals of effusion – Desorption models*

An accurate description of the distribution of directions for re-desorbed particles requires the knowledge of the general bidirectional reflectance probability distribution for a specific atom or molecule on the specified adsorbent surface. This function that describes the re-desorption direction as a function of the incident particle direction is difficult to measure and hence scarcely available in literature. Different approximations of this function are therefore implemented in MC codes depending on the potential loss of energy during the interaction.

If elastic, the kinetic energy of the test particle is conserved and the interaction is described as a specular reflection [120]. In the interaction, the component of the velocity vector that is perpendicular to the adsorbent surface is inverted while the tangential component is conserved. It is thus a mirror-like reflection where the angle of reflection is defined by the angle of incidence. An elastic description of the collision is best suitable for cases where the projectile does not chemically interact with the adsorbent surface. Additionally, elastic reflections at the macroscopic level as described in MC codes are only valid for micro-polished adsorbent surfaces. However, the hotter the adsorbent surface, the closer the reflection is to being specular.

In contrast, if the interaction is inelastic, it is described as a diffuse reflection. This inelastic nature of the interaction can be due to either the chemical nature of the interaction or the roughness of the surface. A specific

case of diffuse reflection occurs when the atom is considered to thermalize fully with the adsorbate. In this case, the Lorentz-Lambert model [122] or cosine law [123] is applied. This means that the probability of test particle to be re-desorbed at a certain angle with the normal vector to the adsorbate surface scales with the cosine of this angle. Unless otherwise stated, this re-desorption law was used in all the effusion calculations of this work.

Apart from pure specular and ideally diffuse reflection descriptions, other models have been proposed. These are mostly models mixing properties of the specular and diffuse reflections and circumstantially tend to either of the two. Most of these descriptions are adapted from light transport studies. They include the Maxwell model [124], the Phong model [125], the Torrance-Sparrow model [126], the Blinn model [127] and the Inelastic semi classical model [128]. While the Phong model is based on a weighted combination of the pure specular and diffuse models, the others are mostly based on combining a specular reflection description with a surface-orientation probability-distribution. However, the application of these models to gas dynamics often suffers from missing and unknown parameters.

#### *3.1.3.4 Modeling effusion*

For modelling effusion, the release volume is simulated with droplets inside as illustrated on Figure 3.7. Nuclides desorbed from the surface of the droplets are tracked until the entry of the transfer line, shown here by the red circle. Note that effusion in the transfer line is not modeled in this work because at this point, the ion source to be operated with this target is not yet defined. However, for the validation calculation (see section 4.2), effusion in the transfer line was modeled as the ion source operated in the online experiments was known.

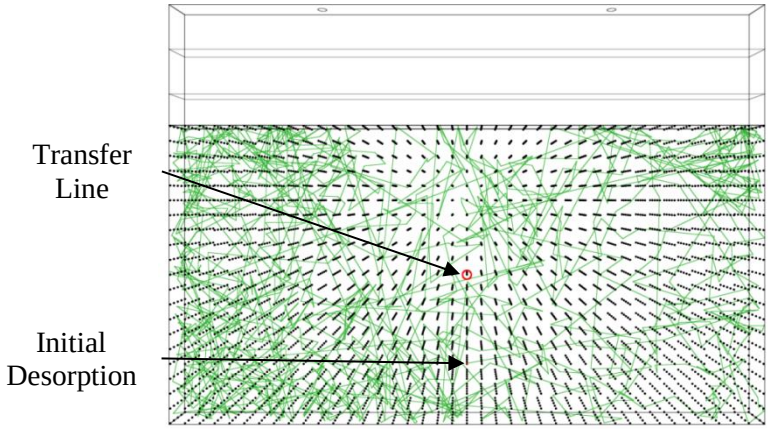


Figure 3.7: Illustration of particle tracking in the release volume.

The release volume shown on Figure 3.7 is a parallelepiped with a flat horizontal grid at the top, used for evacuation of irradiated LBE out of the irradiation volume. For reasons of a simpler manufacturing, this geometry is the one foreseen for the prototype of the target. A flow rate of 160 $cm^3/s$ of LBE coming out of the irradiation volume corresponds to ~600 000 droplets of 200-µm diameter. Geometries in Molflow+ are defined with elementary constituents that are polygons and called facets. This means that the simplest representation of droplets as tetrahedra would yield a model with 2 000 000 facets, which could not be handled by the code because of issues with memory allocation. Indeed, on a Windows operating system, such a 32-bit application can only allocate up to 4 GB of RAM. In addition, because of the ray tracing algorithm implemented in the code, the calculation speed per particle is inversely proportional to the number of facets.

For these reasons, each vertical string of droplets in the model was approximated as a cylinder with an opacity factor defined by the ratio of droplets to cylinder volume. The speed of calculation was also improved by modeling only the vertical half symmetry of the release volume. Validation of these approximations is shown in chapter 4.

On average, a nuclide makes few tens of thousands of collisions on its effusion track. The main output of the calculation is a set of points representing the effusion delay time distribution (see Figure 3.8). Zooming on the first microseconds of the distribution, one can notice a time period with a probability density equal to zero. This time period represents the time required for the first nuclide to reach the pumping surface in the calculation.

An increase of this zero-probability time-period is observed if effusion in the transfer line is modeled.

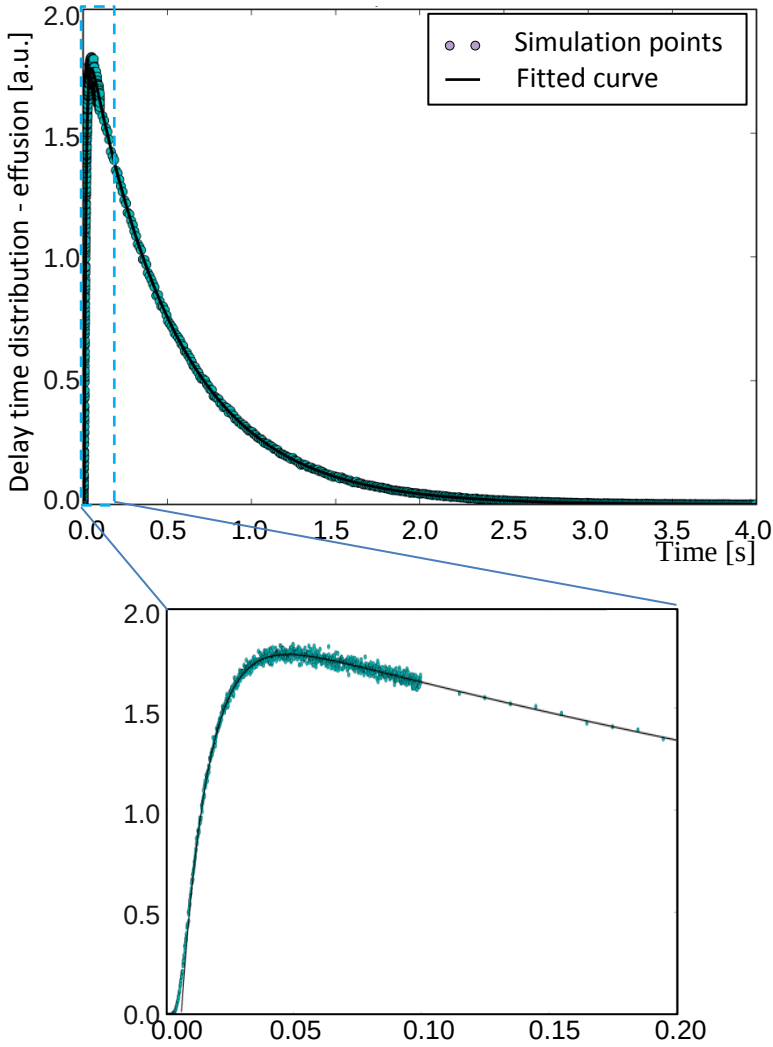


Figure 3.8: Effusion delay time distribution.

The numerical effusion delay time distribution computed with Molflow+ is fitted with expression (3.30) in order to obtain an analytical model for effusion.

$$R_{ef}(\Delta t_{ef}) = \begin{cases} 0 & 0 \le \Delta t_{ef} \le \Delta t_{0ef} \\ i\left(1 - e^{-j(\Delta t_{ef} - \Delta t_{0ef})}\right) e^{-k(\Delta t_{ef} - \Delta t_{0ef})} & \Delta t_{ef} \ge \Delta t_{0ef} \end{cases} \quad (3.30)$$

The first portion of the expression reflects the zero-probability time-period $\Delta t_{0ef}$ determined from the Monte Carlo calculation. The rest of the distribution is typically fitted with a combination of a rising and a decreasing exponentials with $i, j$ and $k$ the fitting parameters. In most calculations the rise of the distribution is too fast ( ~$10^{-6}$ s) to be captured in the MC calculation with a low enough uncertainty within reasonable calculation time. Because the figure of merit in these calculations is the area below these ***pdf***s, such a sharp rise could be treated as a step in the analytical description. The function fitted to those calculations thus becomes:

$$R_{ef}(\Delta t_{ef}) = \begin{cases} 0 & 0 \le \Delta t_{ef} \le \Delta t_{0ef} \\ ie^{-k(\Delta t_{ef} - \Delta t_{0ef})} & \Delta t_{ef} \ge \Delta t_{0ef} \end{cases} \quad (3.31)$$

The idea behind this process is to combine the accuracy of modeling of a numerical MC tool with the simplicity of an analytical description. It also enables comparing the results of the time dependent MC simulation with approximations proposed in literature (see section 4.1.6).

#### *3.1.3.5 Delay time distribution at transfer line*

The last step in the construction of the overall delay time distribution of the target is the convolution of the ***pdf*** of the effusion process with the delay time distribution for nuclides reaching the surface of the droplets in which they were evacuated:

$$R_{is}(t_{is}) = \int_0^{t_{is}} R_{ds}(t_{ds}) \times R_{ef}(t_{is} - t_{ds}) dt_{ds} \quad (3.32)$$

The different calculations required in evaluating the overall delay time distribution (see Figure 3.9) of the target are performed by Python scripts.

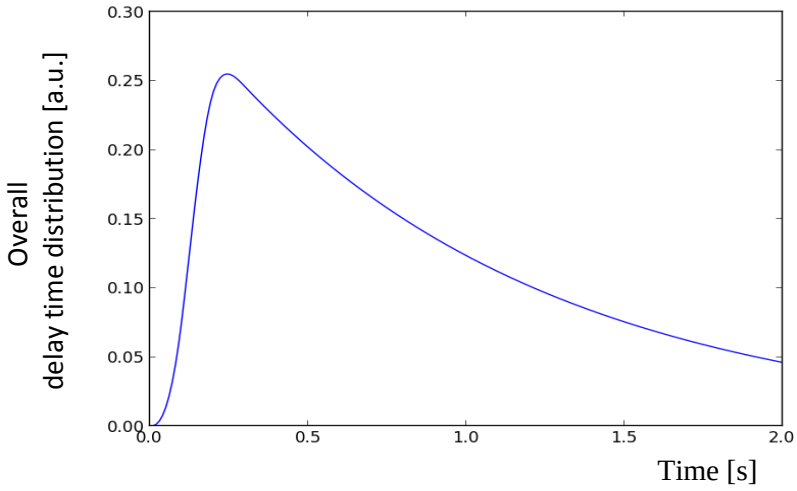


Figure 3.9: Delay time distribution for nuclides reaching the inlet of the transfer line. The release volume dimensions are: 20 cm x 12 cm x 2 cm.

The probability of nuclides surviving radioactive decay during the time $t_{is}$ required for their release can then be assessed, resulting in the fractional-release function defined as:

$$F(t) = \int_0^t R_{is} \exp(-\lambda \times t_{is})\ dt_{is} \tag{3.33}$$

In expression (3.33), $\lambda$ is the decay constant of the nuclide of interest and $F(t)$ is the fraction of atoms of this nuclide produced at $t = 0$ that has survived decay and already reached the ion source at a time $t$. Since both the delay time distribution and the survival rate to radioactive decay decrease exponentially with time, the fractional-release function illustrated on Figure 3.10 shows an asymptotic behavior at large time values.

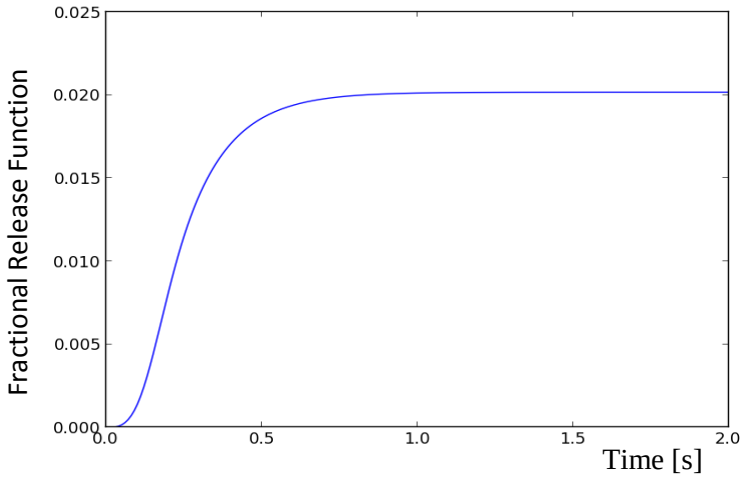


Figure 3.10: Fractional release function with an asymptote value of ~2%. The release volume dimensions are: 20 cm x 12 cm x 2 cm.

The asymptote value of the fractional release function corresponds to the overall release efficiency defined as:

$$\varepsilon_{rel} = \int_0^{\infty} R_{is} \exp(-\lambda \times t_{is})\ dt_{is} \tag{3.34}$$

The overall release efficiency is the parameter used in the optimization process (see chapter 4) to compare different design options.

## 3.2 Conclusion

Beside the development of a high power target for next generation ISOL facilities, the second objective of the LIEBE prototype is to improve the yield of nuclides in comparison with the current static bath targets operated at CERN/ISOLDE. This target specifically aims at the production of short-lived Hg isotopes with a half-life in the order of 100 ms. For this reason, a very efficient release of nuclides is crucial in order to minimize decay losses.

In order to model the release of nuclides out of the target and assess its efficiency, the comprehensive model presented in this chapter was constructed. In the method developed, existing analytical descriptions of the diffusion process are used, in combination with an analytical fit of the numerical distribution obtained from Monte Carlo simulations of the effusion process. This gives as output an analytical model that is supported by detailed Monte Carlo calculations when required.

The analytical approach used has the advantage that it implies no cutoff of the distribution tail as it is the case with a numerical convolution or the diffusion sampling approach. This renders more accurate the computation of release efficiency.

# 4 Target design & optimization – Isotopes-release aspects

In the previous chapter, the method developed to model the release of nuclides out of the LBE-loop target was presented. The method includes a Monte Carlo simulation of the effusing nuclides, the results of which are potentially affected by the simulation settings and approximations. In the first section of this chapter, the validity of approximations made to simplify or speed up the simulations is investigated. In this section, the sensitivity of the MC simulation to parameters such as the desorption or reflection distributions, that are not precisely known is also studied.

Before the method developed for modeling the release of nuclides is applied to the optimization of the LBE loop target, it first had to be validated. For this purpose, the method is applied to three different cases and its results compared with experimental data. This is discussed in the second section. Since no loop-type target has been operated online yet, the selection of cases for validation is limited to static targets. The first case is a validation of the method against experimental data for the liquid-Pb target operated at ISOLDE-SC. The other cases show the possibilities of this method by applying it to two thin-foils solid targets with different internal layouts.

As mentioned before, a crucial point with a thick target for the production of short-lived nuclei is to design it with good release properties. Indeed, isotope release is known to be slow out of a static thick liquid target [33]. To circumvent this issue, a so-called release volume is foreseen in the current design, inside which the target material is spread into a shower of small droplets. The efficiency of the release of isotopes will be affected by parameters including the size and number of droplets as well as the size and geometry of the release volume. Design and optimization studies are therefore required in order to maximize the yields out of this novel target. In the third section of the chapter, the influence of key geometrical parameters on the release efficiency of the target is presented.

## 4.1 Effects not specifically modelled with the effusion process

### 4.1.1 Transparent cylinders approximation of the droplets

One crucial aspect of Molflow+, the Monte Carlo code used for the effusion calculations, is the limitation on memory allocation related to the 32-bit format of this Windows application. Additionally, it is intrinsic to the ray tracing algorithm implemented in the code that the calculation speed per particle is inversely proportional to the number of facets. The reason for this is that, following each interaction of a test particle with a facet, the code first determines its re-emission direction and then looks for the next interaction in this direction. To do so, the code first searches for potential collisions with all facets of the geometry and then selects the closest as the next interaction point.

Because of the large number of droplets ( ~ 600 000 droplets of 200-µm diameter for a flow rate of 160 $cm^3/s$), modeling the release volume even with a tetrahedral representation of the droplets requires the code to allocate more than its maximum memory and results in the code crashing. To solve this problem and at the same time speed up the simulations, vertical strings of droplets were approximated as cylinders with an opacity factor defined by the ratio of droplets to cylinder volume. The opacity factor of a facet is defined as the probability (0 - 1) that a particle with a flight direction intersecting the facet makes a collision with the facet. This factor defines a transparent facet through which particles will pass without interaction with a probability equal to one minus the opacity value. The vertical motion of falling droplets, assumed here and throughout the chapter, corresponds to droplets formed at the tip of vertical apertures distributed over a flat horizontal surface as present in the prototype.

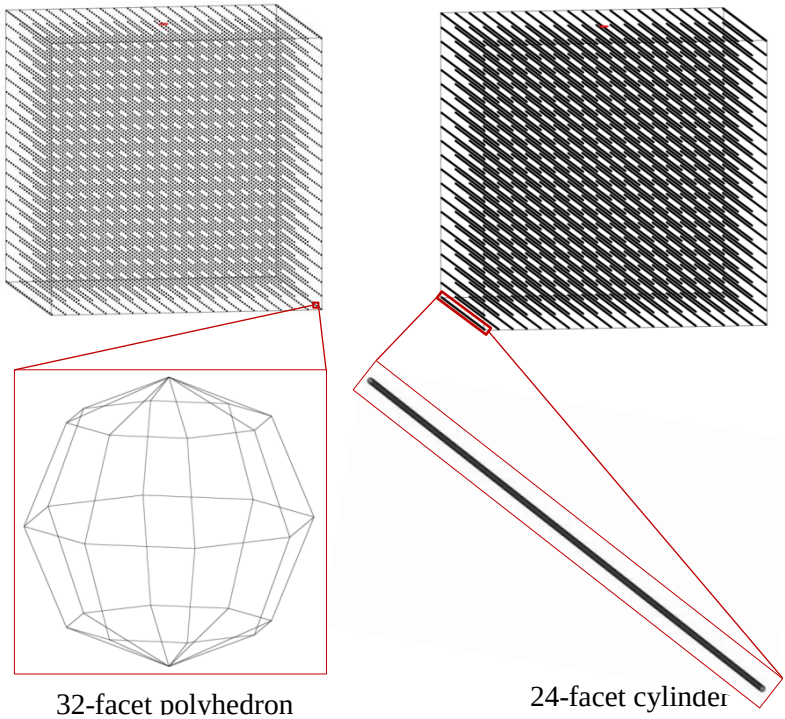


Figure 4.1: Transparent cylinders approximation of the droplets. The 21x21x21 array of 32-facet polyhedra is approximated by a 21x21 array of 24-facet transparent cylinders with an opacity defined by the ratio of droplets to cylinder volume.

To validate this approximate representation of the geometry, the test illustrated on Figure 4.1 was set. A 21x21x21 array of 32-facet polyhedra representing the droplets is approximated by a 21x21 array of 24-facet transparent cylinders. This array size was selected, not to exceed the memory limitation. To visualize the influence of the opacity factor, the 21x21 array of 24-facet cylinders geometry is all simulated with an opacity factor equal to one for the facets of the cylinders. Both the droplets and cylinders are 200 μm in radius. In all cases, the probability density function (***pdf***) of particles reaching a pumping aperture that mimics the entrance of a transfer line is computed. The test was run for different values of droplets spacing, ranging from 500 μm to 5 mm and covering potential values of interest for the optimization of the target design. The same value of spacing is applied to the corresponding cylinders simulations.

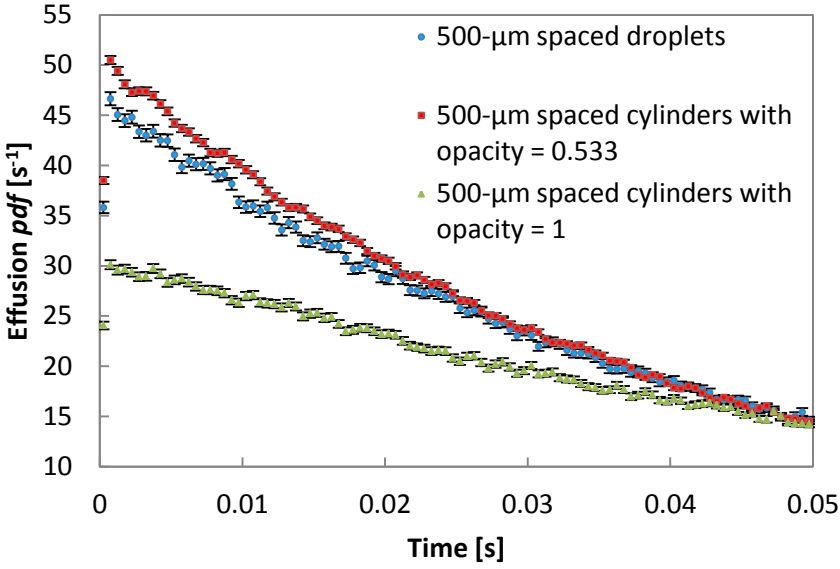


Figure 4.2: Effusion pdfs for the 500-µm spaced droplets case.

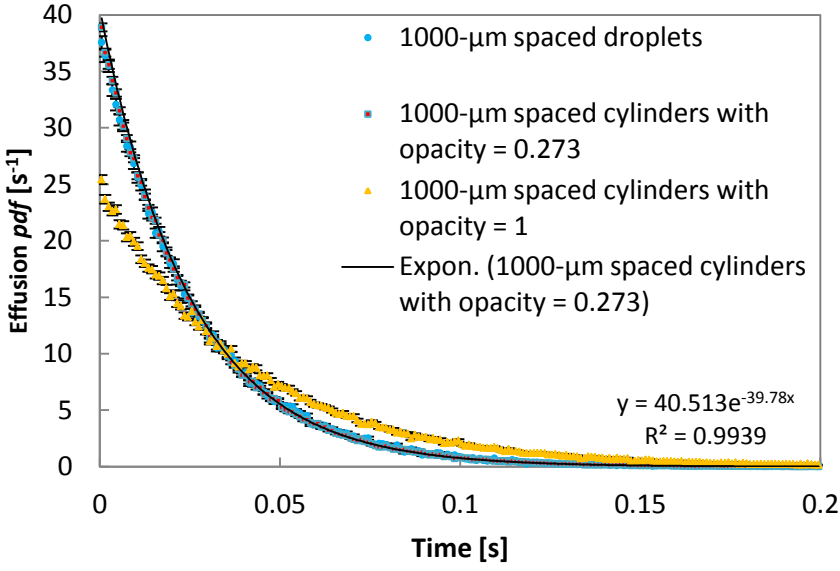


Figure 4.3: Effusion pdfs for the 1000-µm spaced droplets case.

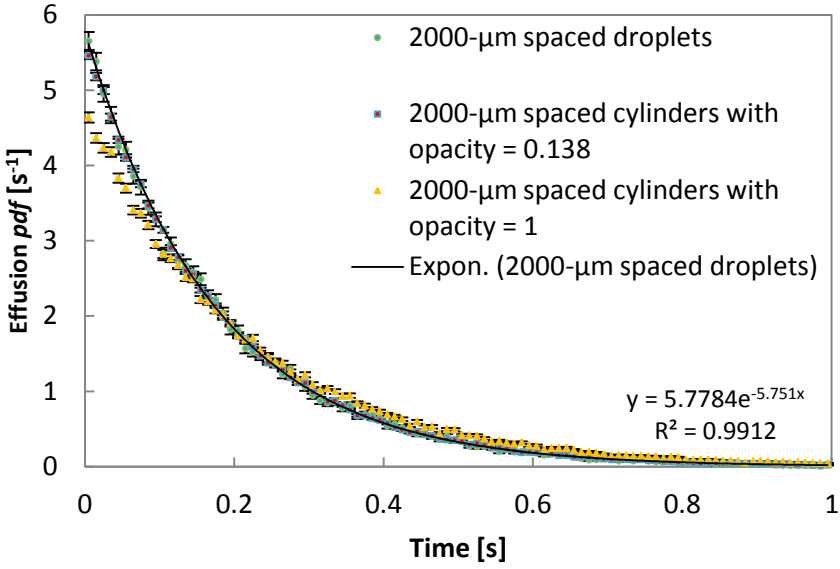


Figure 4.4: Effusion pdfs for the 2000-µm spaced droplets case.

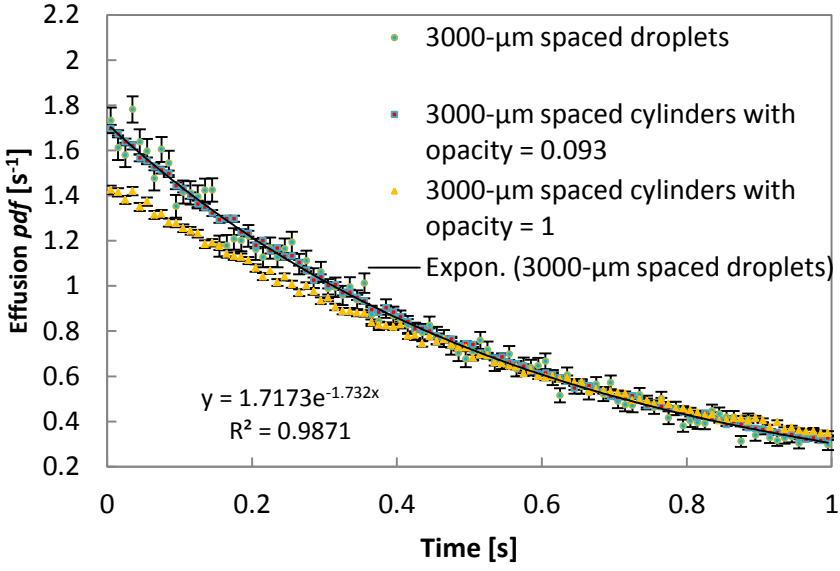


Figure 4.5: Effusion pdfs for the 3000-µm spaced droplets case.

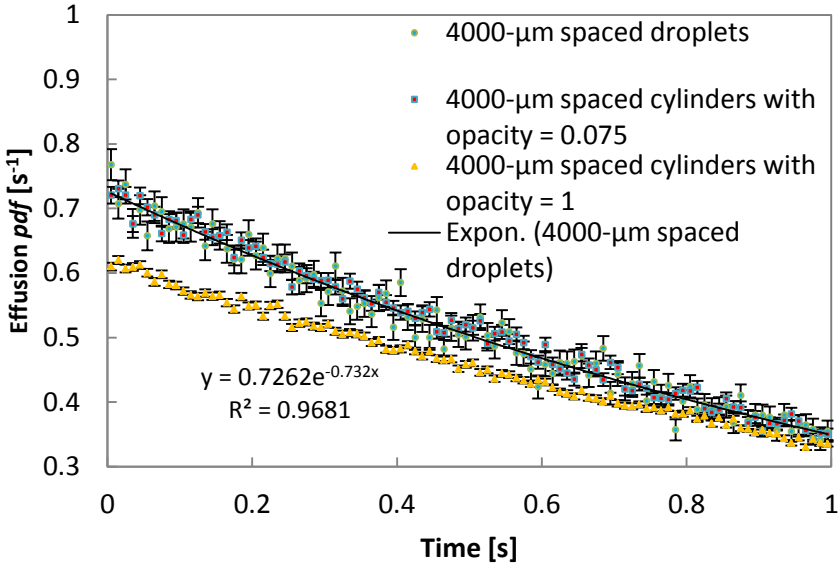


Figure 4.6: Effusion pdfs for the 4000-µm spaced droplets case.

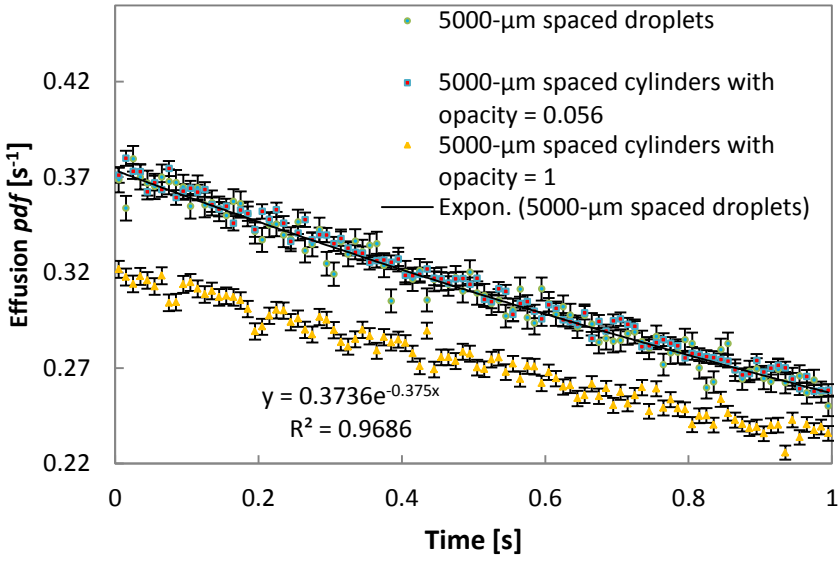


Figure 4.7: Effusion pdfs for the 5000-µm spaced droplets case.

The results shown on Figure 4.2 through Figure 4.7 validate the transparent cylinders approximation as the ***pdf***s correspond within statistical uncertainty to the functions obtained for droplets simulations. On Figure 4.3 through

Figure 4.6, the fit of expression (3.31) to the data, with $\Delta t_{0ef} = 0$ is displayed. These cases have the particularity that the pumping surfaces are of the same size, 3 mm in diameter like the ISOLDE transfer line. It is shown on Figure 4.8 that both $i$ and $k$ parameters of expression (3.31) scale with the inverse of the simulation volume.

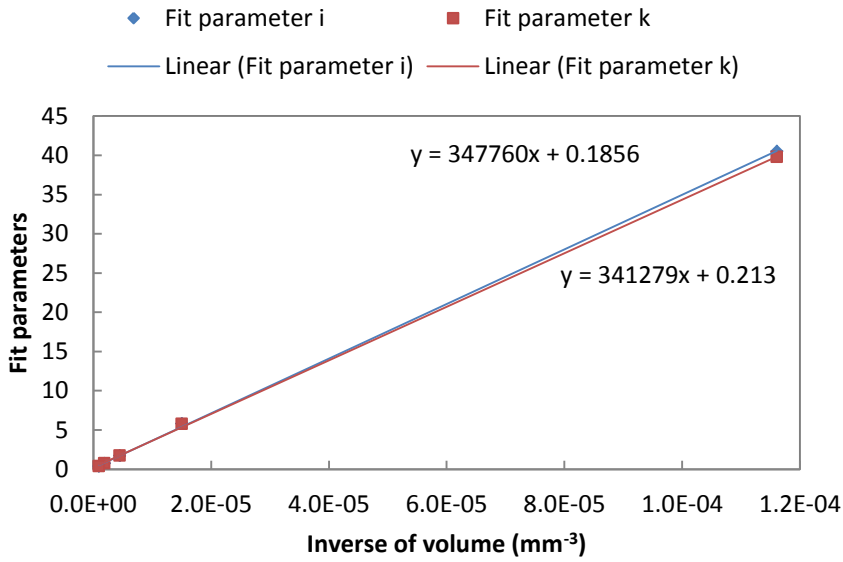


Figure 4.8: Fit parameters from expression (3.30) fit to the data on Figure 4.3 through Figure 4.6.

### 4.1.2 Half-symmetry approximation

An additional approximation implemented to speed up the calculations is to take advantage of symmetry in the geometry. Due to the gravitational acceleration of the droplets and the position of the transfer line, the symmetry implemented in this case is the mirror symmetry relative to the vertical mid-plane of the chamber perpendicular to the beam. The symmetry is illustrated in Figure 4.9. The circular pumping surface at the entrance of the transfer line in the full geometry is replaced in the approximate half geometry by a half circle.

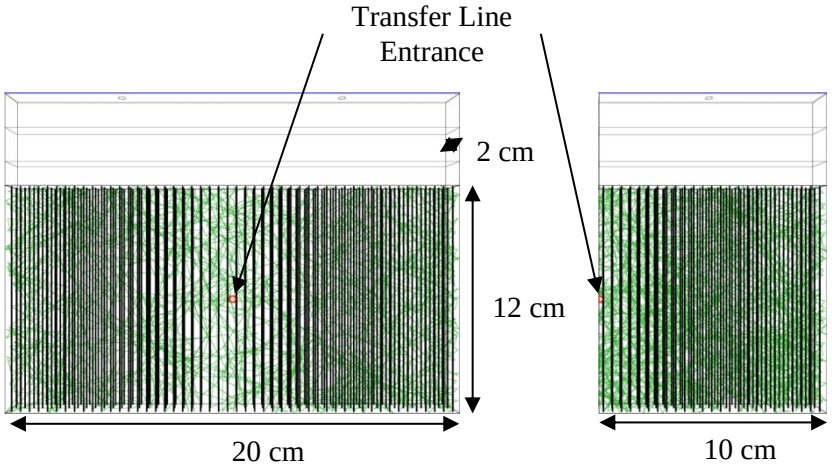


Figure 4.9: Half symmetry approximation.

The full geometry includes 2520 cylinders of 200-μm radius uniformly spaced by 1.2 mm in each horizontal direction. In both geometries, the mean free path of MC particles was 6.3 mm and, on average a particle travels 188 m from its initial desorption to its arrival at the transfer line entrance. It derives from this that on average a particle makes ~ 30 000 surface interactions on its effusion track. Given by the average of the Maxwell-Boltzmann distribution, the mean flight velocity of the particles is 236 m/s at 473 K and 320 m/s at 873 K. From this, the mean flight time between two surface interactions can be determined to be ~27 μs at 473 K and ~20 μs at 873 K.

The effusion delay time distribution of the half symmetry is compared to the distribution obtained for the full geometry case on Figure 4.10. The comparison shows that the half symmetry geometry with specular reflection on the symmetry plane is a valid representation of the full geometry.

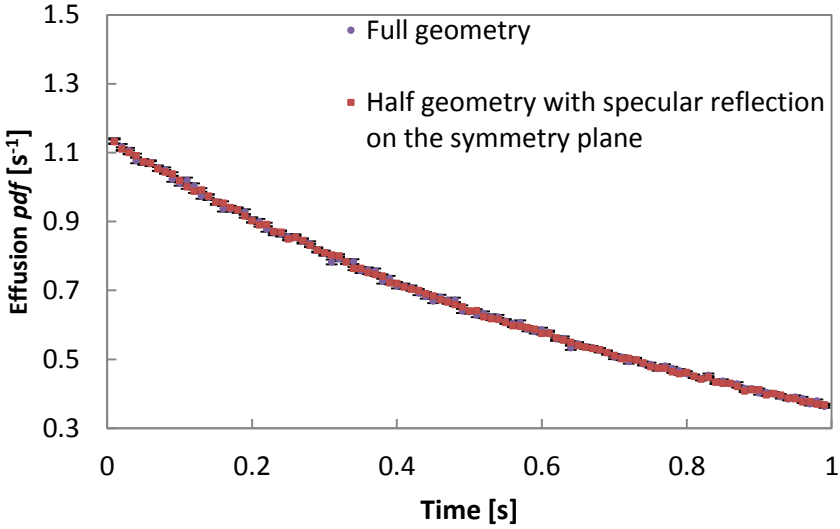


Figure 4.10: Effusion pdfs for the half symmetry approximation.

### 4.1.3 Gravitational acceleration

Because of the gravitational acceleration, falling droplets will be vertically more spaced as they get closer to the bottom of the release volume. The vertical velocity $v(t)$ and position $z(t)$ of a droplet in such a free fall condition can be expressed as $v(t) = gt + v_0$ and $z(t) = \frac{1}{2}gt^2 + v_0 t + z_0$ respectively. In these expressions $t$ represents the time elapsed since the droplet detached from the tip of the evacuation aperture while $v_0$ and $z_0$ are the respective initial vertical velocity and position.

The mean evacuation velocity can be derived from the flow rate, the size and number of evacuation apertures. It is used here as an approximate of the initial vertical velocity $v_0$. In addition, by combining the average size of the droplets and the flow rate one finds the average time period $t_{period}$ between two consecutive droplets formed at a single aperture. The value of this time spacing between two consecutive droplets formed at a single aperture is kept constant along the fall of the droplets, provided the droplets are formed with the same initial vertical velocity.

During their fall, the vertical distance between two consecutive droplets formed at a single aperture can then be approximated as the product of $v(t)$ and $t_{period}$. Also, the number density of droplets along such a vertical structure scales inversely with the vertical distance between two consecutive

droplets which means that it inversely scales with $v(t)$. It can be derived from this that the opacity factor defined in section 4.1.1 and introduced for the transparent-cylinder approximation scales linearly with $1/v(t)$ as well. Because the Molflow+ code only allows the definition of a single opacity value per facet, accounting for this effect of gravity in modeling the release volume would induce models with larger memory requirement and runtime than envisaged in sections 4.1.1 and 4.1.2.

To check the influence of the gravitational acceleration effect on the effusion delay time distribution and thus evaluate whether a valid approximation can be obtained while neglecting this effect, a validation test was conducted. The half symmetry geometry (similar to Figure 4.9) of a 30-cm high release volume was simulated both with and without accounting for the vertical density change due to gravity. For the simulation with vertical density change, the single vertical cylinders shown on Figure 4.9 are broken vertically into multiple sections as shown on Figure 4.11.

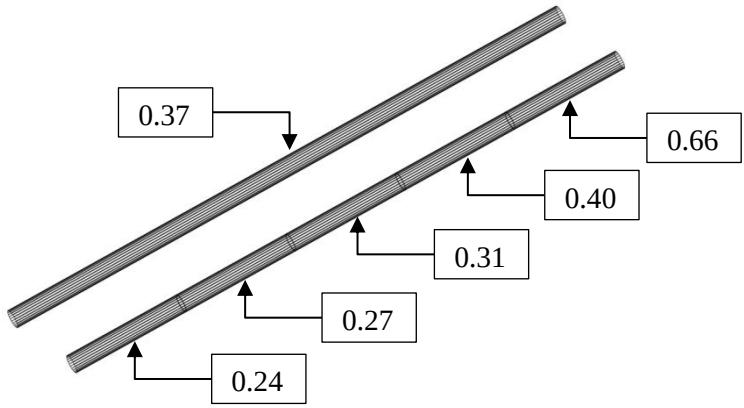


Figure 4.11: A 30-cm long cylinder sectioned in 5 portions. The corresponding opacity values are mentioned for an initial vertical velocity of 0.56 m/s.

Each of the equal-size sections is characterized by a different value of opacity. To determine the opacity value of a section, as defined in paragraph 4.1.1, it is required to compute the volume of droplets in suspension inside the section. To this end, the number of droplets in suspension inside the section is determined by multiplying the rate of droplet formation at an aperture by the time it takes a droplet to fall the length of the section. The volume of droplets in the section can subsequently be determined, knowing the volume of a single droplet. To ensure that the result is independent of the

number of vertical sections, different simulations were run, each with a different number of vertical sections.

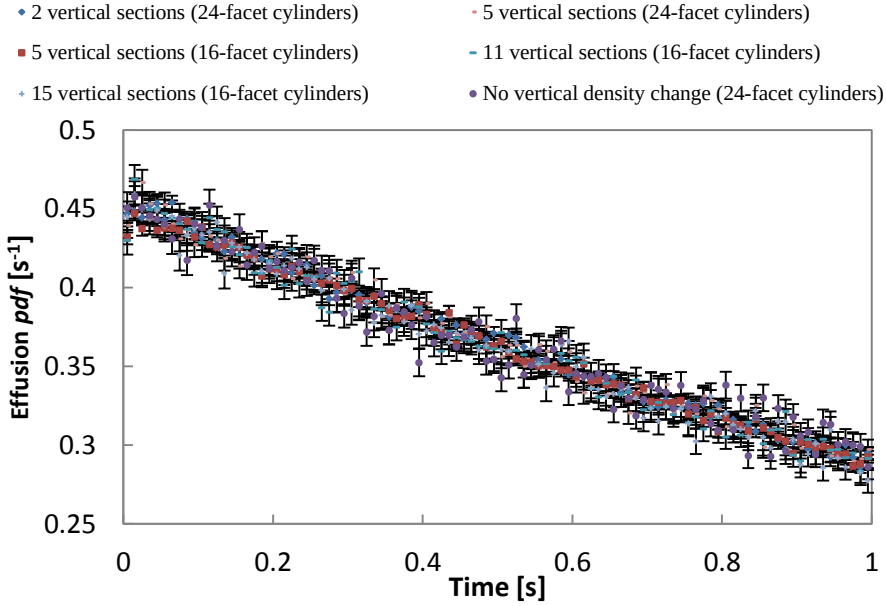


Figure 4.12: Effusion pdfs, accounting or not for the vertical density change due to gravity.

The results, on Figure 4.12, show that the effusion ***pdf***s agree with each other within the statistical uncertainty, independently of the number of vertical sections. It is also noticeable on this figure that a valid effusion delay time distribution is obtained even when the vertical density change due to gravity is not accounted for. In addition, since a coarser representation was required for the cases with many vertical sections, the 5-vertical-sections case was simulated both with a fine and a coarser representation of the cylinders. Whether simulated with 24-facet or 16-facet cylinders, the results are consistent within the statistical uncertainty of about ± 4%.

### 4.1.4 Non-uniform spatial desorption

One more source of complexity in the simulation of the release volume is induced by diffusion. The ***pdf*** of a nuclide diffusing to the surface of the droplet in which it was evacuated presents an exponential decrease over time. Because diffusion occurs during the fall of the droplets, this means that the rate at which diffusing nuclides populate the surface of a droplet at the bottom of the release volume is smaller than the rate at which the surface

of the same droplet was populated when it was close to the irradiation volume. Since no surface accumulation of nuclides is assumed (see section 3.1.2.3), it follows that the rate of nuclide desorption from the surface of a droplet decreases as the droplet falls in the release volume.

In addition, the period between two consecutive proton-pulses irradiating the target can be large with respect to the time it takes to fully evacuate the irradiated LBE from the irradiation volume. In this case, situations where the release volume is filled partially with irradiated and partially with non-irradiated LBE droplets will occur. Short-lived nuclides are not present in the non-irradiated LBE droplets and the spatial distribution of nuclides-desorption rates can be even further away from a uniform distribution. This effect is not relevant for ISOL@MYRRHA since the pulse period of 2 ~ 4 ms is smaller than the 100 ms it takes to fully evacuate the irradiated LBE. In order to model these dynamic effects occurring on a time scale similar with the effusion process itself, the desorption rate of the transparent cylinders should be varied both in space and time during the simulation in order to reproduce the evolution illustrated on Figure 3.5, page 57.

Accounting for the effects mentioned above in this section would inevitably lead to models complex to setup and long to run. To assess the potential loss of accuracy induced by not accounting for these effects, their influence on the effusion delay time distribution was checked. The half-symmetry geometry (Figure 4.9) of a 30-cm high release volume was simulated with different spatial configurations of desorption. With respect to situations where the release volume is filled partially with irradiated and partially with non-irradiated LBE droplets, two simulations were run. In the first, particles are only initially desorbed from the first 5 mm at one extremity of the cylinders. In the second simulation, particles are only desorbed from a 5-mm section located vertically at center of the cylinders. With respect to the diffusion effect, a third simulation was run with relative desorption rates following the trend described in expression (3.21). In this case, transparent cylinders with 15 vertical sections are used, each section with a different value of desorption rate.

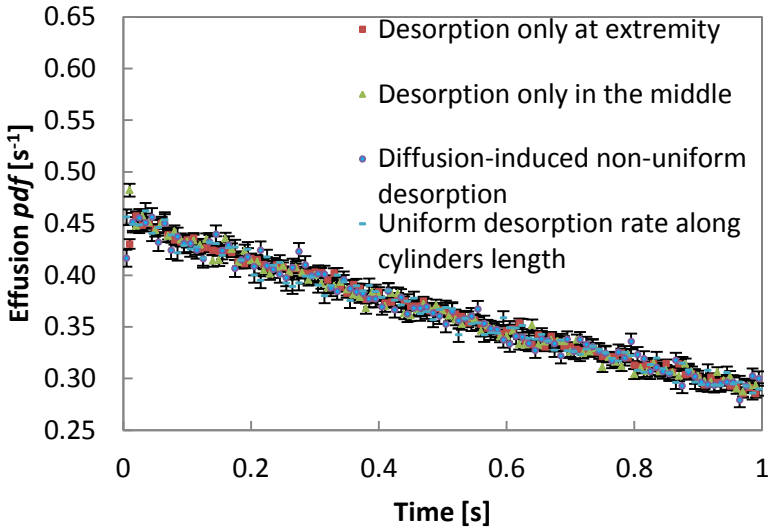


Figure 4.13: Effusion pdfs, accounting or not for different effects affecting the space and time distributions of desorption rates.

The results of these simulations are compared on Figure 4.13 with the output of an approximate simulation where particles are desorbed from the full length of the cylinders. No change in desorption rate is accounted for. Apart from the first time bin, all the ***pdf***s on Figure 4.13 are consistent within statistical uncertainty. The probability density value of the first bin is higher in case the desorbing particles only come from the middle sections of the cylinders while lower values are computed if particles are only desorbed from the extremities of the cylinders. This is expected since desorbing facets at an extremity of the cylinders see the entrance of the transfer line under a solid angle smaller than the angle under which desorbing facets in the middle of the cylinders see the same transfer-line-entrance. Note that this effect only significantly affects particles flying straight from their initial desorption-site to the entrance of the transfer line, like particles recorded in the first time bin. Understandably, when a uniform desorption rate along the cylinder length is used, the probability density value of the first bin is between the value for desorption only at an extremity and the value for desorption from the middle section. In the simulation case where non-uniform desorption rates induced by diffusion are applied, most of the particles are initially desorbed off-centered and close to the cylinders extremity at the top of the release volume. This explains why the value of the probability density in the first time bin is consistent with results for the case where desorption only occurs at an extremity.

### 4.1.5 Effect of sticking

Between their initial desorption and their potential arrival at the transfer line, atoms and molecules undergo a succession of flight steps and surface interactions in the release volume. The two sorption mechanisms that can occur upon interaction of a particle with a surface have been introduced in section 3.1.3.2. These mechanisms are currently not accounted for in Molflow+ simulations so, the effusion delay time distributions shown throughout this chapter are computed assuming that the particles immediately re-desorb after each surface adsorption.

An expression to account for the sticking time induced by adsorption/desorption is given in section 3.1.3.2 (see expression (3.15)). Applied to Hg adsorption on Pb, this expression gives a mean sticking time per surface interaction of $\tau_s = 4.75\ 10^{-8}$ s at 473 K and $\tau_s = 2.16\ 10^{-11}$ s at 873 K. To obtain an effusion delay time distribution accounting for surface sticking, each abscissa coordinate on the ***pdf*** output from Molflow+ should be increased by a shifting parameter. The shifting parameter is the product of $\tau_s$ with the mean number of collisions of particles completing their effusion track within the time bin corresponding to the abscissa value. The mean number of collisions for each time bin is obtained by dividing the abscissa value corresponding to the time bin by the mean flight time between two surface interactions (see section 4.1.2). However, because the mean sticking time in this case is lower by several orders of magnitude than the mean flight times given in section 4.1.2, they have been neglected and the uncorrected effusion delay time distributions are used throughout the work.

Apart from adsorption which is a surface interaction, particles interacting with a surface can also undergo absorption, meaning that the particle dissolves in or permeates the structure of the sorbent. In the worst case, an atom/molecule can dissolve in the sorbent for long enough to be considered permanently absorbed. Permanent dissolution in this context means that the time scale for dissolution is very long in comparison with the half-life of the nuclide. Depending on the probability of permanent dissolution for each surface interaction, absorption might significantly affect the effusion delay time distribution. Such a probability is called a sticking factor in Monte Carlo codes for particle tracking. The sensitivity of the effusion delay time distribution to the sticking factor was thus studied and the results are displayed on Figure 4.14 and Figure 4.15.

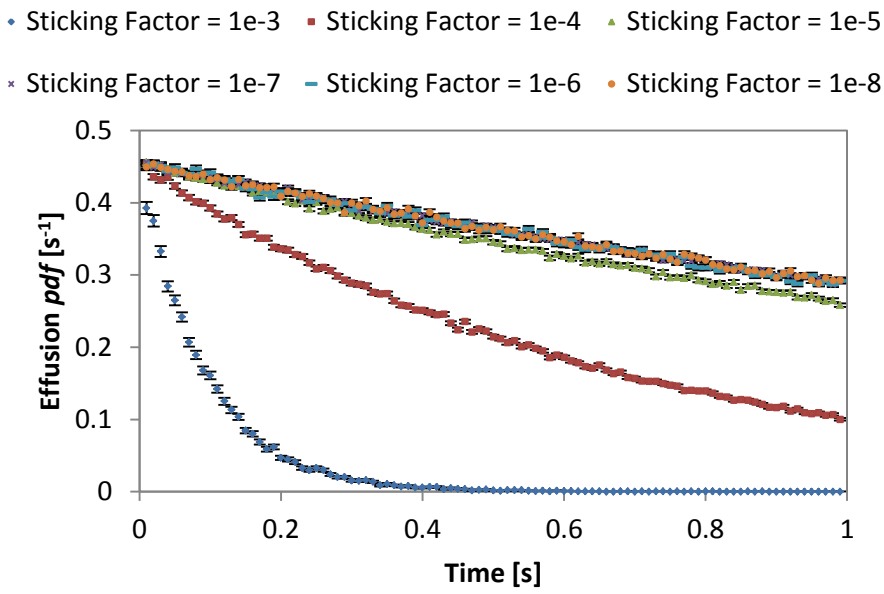


Figure 4.14: Sensitivity of the effusion delay time distribution to the sticking factor of particles on the walls of the release volume.

The half-symmetry geometry with a 30-cm high release volume was simulated with on one side, different values of the sticking factor of particles on the walls of the release volume and on the other side, different values of the sticking factor of particles on the surfaces of the transparent cylinders. It can be derived from the data on Figure 4.14 that the permanent retention of particles is only significant if the corresponding sticking factor is higher than $10^{-5}$. Similarly, from Figure 4.15, the permanent dissolution of particles in the droplets would become significant as the sticking factor rises above $10^{-6}$. The more stringent condition for particles sticking on the surfaces of the transparent cylinders can be explained by the fact that in this geometry, about 80% of the surface interactions occur on the surfaces of the cylinders.

Unable to find any straightforward method to determine the sticking factor, the probability of permanent dissolution is judged here through the ratio between sticking time before re-desorption $\tau_s = 2.16\ 10^{-11}$ s at 873 K, and the diffusion time in the droplets $\langle \Delta t_{di} \rangle = 0.44$ s at 823 K. In the absence of more precise data, based on this first order analysis, the permanent dissolution of Hg atoms in the droplets is not expected to significantly influence the effusion delay time distribution.

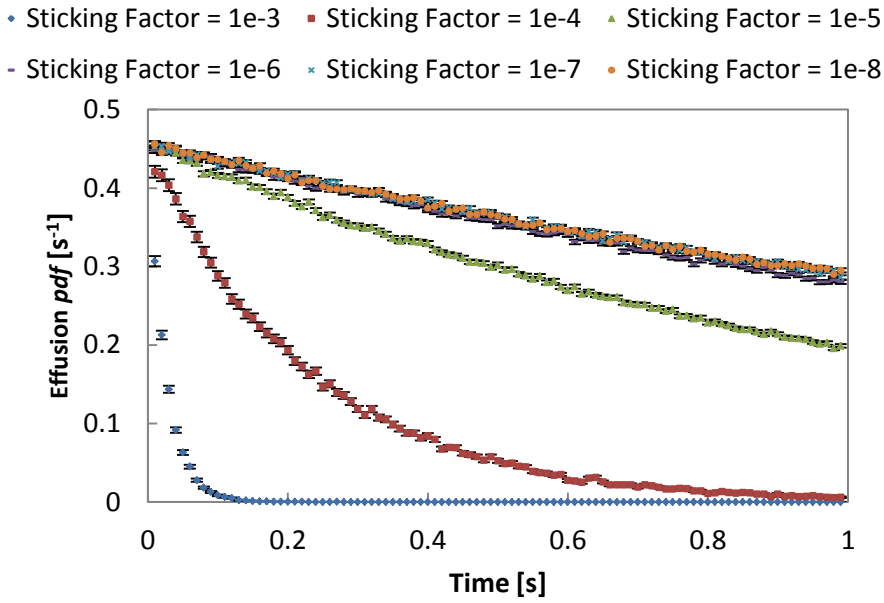


Figure 4.15: Sensitivity of the effusion delay time distribution to the sticking factor of particles on the surfaces of the transparent cylinders.

### 4.1.6 Comparison of the fit parameter k with approximations evaluated from expressions proposed in literature

By analogy with evacuation of a volume through an orifice, the delay induced by effusion was described [74, 98] as $P_v(t) = ve^{-vt}$ with $1/v = N_{col}(\tau_s + \tau_f)$. In this expression, $N_{col}$ is the mean number of collisions a particle makes with the target material surfaces and container walls before leaving the target, $\tau_s$ is the mean sticking time of particles per surface interaction and $\tau_f$ is the mean flight time between two consecutive surface interactions. A variant of this description is given in [100], where the time characteristic of the exponential is defined as $1/\tau_c$ with $\tau_c \cong 3/4\,[N_{col}\tau_s + L/v]$. $L$ in this other description is the mean length of nuclide paths from initial desorption to exit from the target while $v$ is the mean value of the Maxwell-Boltzmann speed distribution. None of these descriptions accounts for the zero-probability time-period $\Delta t_{0ef}$ or the rising section of the effusion distribution shown on Figure 3.8, but applying any of these in this work would still have required Monte Carlo calculations to determine $N_{col}$, $\tau_f$ or $L$. To check the validity of their possible application, the time characteristics $v$ and $1/\tau_c$ are compared to the fit parameter $k$ in expression

(3.31). In this comparison, the sticking part is neglected. The comparison shown on Figure 4.16 refers to the data in Figure 4.2 through Figure 4.7 and shows that though the trend seems to be reproduced, significant differences can be observed. The same conclusion can be drawn from Figure 4.17, referring to data on Figure 4.24. None of these descriptions is suitable for this study.

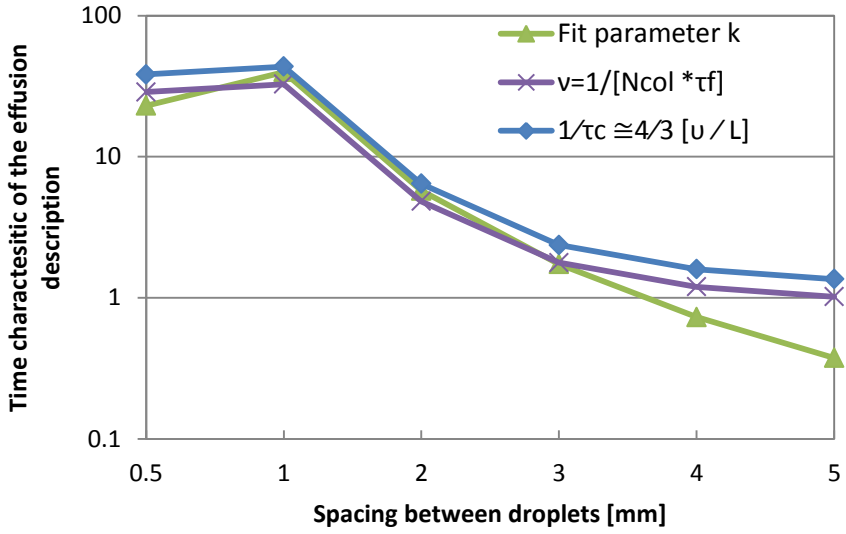


Figure 4.16: Comparison of the fit parameter k in expression (3.31) with approximations evaluated from expressions proposed in literature, for cases described in section 4.1.1.

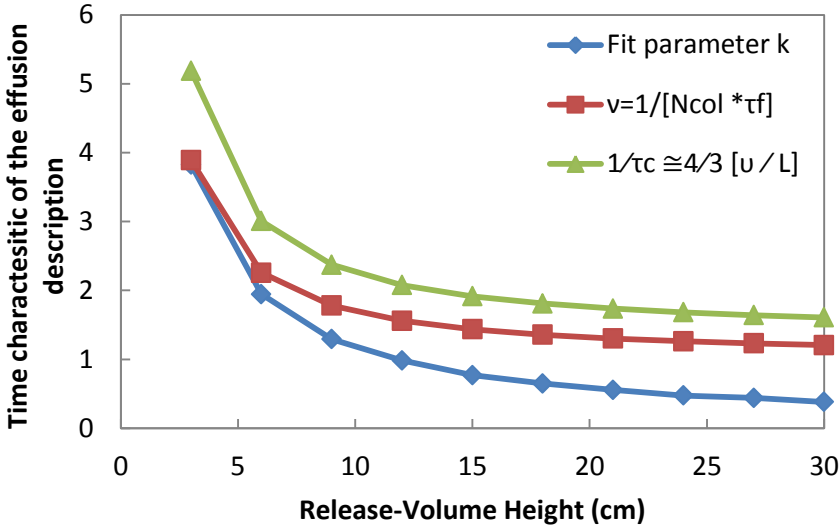


Figure 4.17: Comparison of the fit parameter k in expression (3.31) with approximations evaluated from expressions proposed in literature, for cases described in section 4.3.2.

## 4.2 Validation of the method

The methodology described in chapter 3 for modeling the release of nuclides out of the target is validated in this section by comparing its outputs to experimental data. However, no loop target has yet been operated online at an ISOL facility. The following validation cases have been selected.

### 4.2.1 ISOLDE SC static Pb bath

In this section, the release of nuclides out of the static bath Pb target used at ISOLDE-SC is modeled. The computed release efficiencies of different Hg isotopes are compared to experimental data [33]. A schematic drawing of the target and transfer line layout is presented on Figure 4.18 (top) along with a diagram of the simplified geometry defined in the simulation.

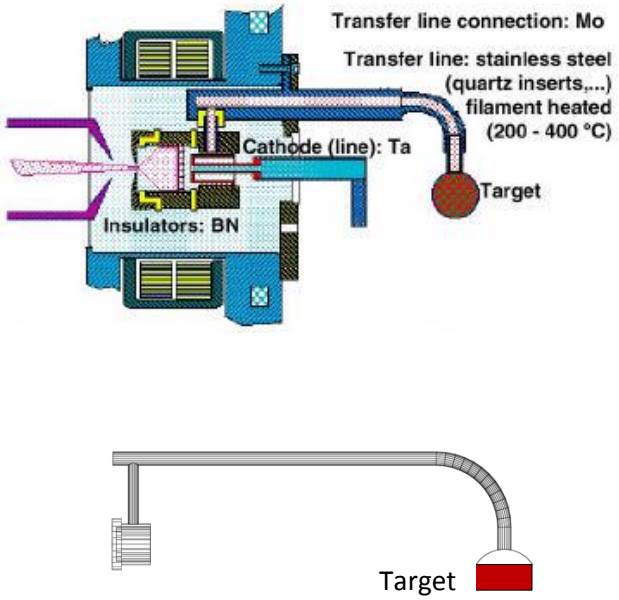


Figure 4.18: (Top) Target and transfer line layout for the static bath ISOLDE-SC Pb target. (Bottom) Diagram of the simulated geometry.

Diffusion of Hg isotopes in the Pb target was simulated with the following conditions:

Impermeability condition at the bottom surface of the bath ($x = 0$):

$$\frac{\partial C}{\partial x} = 0$$

Constant surface-concentration condition at the free surface of the bath ($x = l$):

$$C = C_s\,, \qquad x = l\,, \qquad t > 0$$

Uniform-concentration condition initially $t = 0$:

$$C = C_i\,, \qquad t = 0\,, \qquad 0 < x < l$$

Applying these boundary conditions to the solution of the one-dimensional version of Fick's second law of diffusion [86], one finds:

$$C(x,t) = \sum_{m=1}^{\infty} \frac{(-1)^m 4C_i}{\pi(2m+1)} cos\left[(2m+1)\frac{\pi x}{2l}\right] \exp\left[-(2m+1)^2 \frac{\pi^2}{4l^2} Dt\right] \qquad (4.1)$$

For any time period $\Delta t_{di}$ elapsed since the start of diffusion in the bath, the fraction of the initial amount of a nuclide still remaining inside the liquid bath is [86]:

$$f(\Delta t_{di}) = \left(\frac{8}{\pi^2 - 8}\right) \sum_{m=1}^{\infty} \frac{1}{(2m+1)^2} \exp\left[-(2m+1)^2 \frac{\pi^2}{4l^2} D \Delta t_{di}\right] \tag{4.2}$$

The fraction of the initial amount of this nuclide diffusing out through the free surface in a time period $[\Delta t_{di}\,; \Delta t_{di} + dt]$ is then:

$$Diff(\Delta t_{di}) = \left(\frac{8}{\pi^2 - 8}\right) \sum_{m=1}^{\infty} \frac{\pi^2 D}{4l^2} \exp\left[-(2m+1)^2 \frac{\pi^2}{4l^2} D \Delta t_{di}\right] \times dt \tag{4.3}$$

The ***pdf*** of a nuclide reaching the free surface of the bath after diffusing for a period $t_{bs}$ is derived as:

$$R_{di}(t_{bs}) = \left(\frac{8}{\pi^2 - 8}\right) \sum_{m=1}^{\infty} \frac{\pi^2 D}{4l^2} \exp\left[-(2m+1)^2 \frac{\pi^2}{4l^2} D t_{bs}\right] \tag{4.4}$$

Describing effusion with expression (3.30), the overall delay time distribution for this target is obtained by convoluting expressions (3.30) and (4.4) in:

$$R_{is} = \begin{cases} \int_0^{t_{is}} R_{di}(t_{bs}) \times 0 dt_{bs} & 0 \le t_{is} \le \Delta t_{0ef} \\ \int_0^{t_{is}-\Delta t_{0ef}} R_{di}(t_{bs}) \times i\left(1 - e^{-j(\Delta t_{ef} - \Delta t_{0ef})}\right) e^{-k(\Delta t_{ef} - \Delta t_{0ef})} dt_{bs} & \\ + \int_{t_{is}-\Delta t_{0ef}}^{t_{is}} R_{di}(t_{bs}) \times 0 dt_{bs} & t_{is} \ge \Delta t_{0ef} \end{cases} \tag{4.5}$$

$\Rightarrow$

$$R_{is} = \begin{cases} 0, & 0 \le t_{is} \le \Delta t_{0ef} \\ \left(\left(\frac{8i}{\pi^2-8}\right)\times\left(\frac{\pi^2 D}{4l^2}\right)\right)\sum_{m=1}^{\infty}\left[\begin{array}{l}\left(\left(e^{-\left((2m+1)^2\frac{\pi^2 D}{4l^2}-j-k\right)(t_{is}-\Delta t_{0ef})}-1\right)\right. \\ \left.\times\frac{e^{-(j+k)(t_{is}-\Delta t_{0ef})}}{\left((2m+1)^2\frac{\pi^2 D}{4l^2}-j-k\right)}\right) \\ -\left(\left(e^{-\left((2m+1)^2\frac{\pi^2 D}{4l^2}-k\right)(t_{is}-\Delta t_{0ef})}-1\right)\right. \\ \left.\times\frac{e^{-k(t_{is}-\Delta t_{0ef})}}{\left((2m+1)^2\frac{\pi^2 D}{4l^2}-k\right)}\right)\end{array}\right], & t_{is} \ge \Delta t_{0ef} \end{cases} \quad (4.6)$$

The release efficiency of any nuclide can then be obtained, applying expression (3.34). For Hg isotopes, the efficiencies computed with $D = 2\ 10^{-9}$ m$^2$/s are compared in Table 4.1 with experimental data [33]. Note that the experimental efficiencies as published in [33] are normalized values while the initially computed values (second column of Table 4.1) are not. Because the normalization constant is not specified in [33], a direct comparison with the experimental efficiencies was not possible. Nonetheless, a good match (within a factor 1.3) is observed between normalized, computed and experimental release efficiencies for the different Hg isotopes.

Table 4.1: Computed and experimental release efficiencies for different Hg isotopes. The obtained values are normalized for comparison.

| Isotopes | Computed Efficiencies | Normalized Computed Efficiencies | Normalized Experimental Efficiencies [33] | Re-Normalized Experimental Efficiencies |
|---|---|---|---|---|
| $^{190}$Hg (20 min.) | 54.83% | 100.00% | 96.80% | 100.00% |
| $^{180}$Hg (2.58 s) | 2.99% | 5.46% | 6.00% | 6.20% |
| $^{179}$Hg (1.05 s) | 1.67% | 3.05% | 2.60% | 2.69% |
| $^{178}$Hg (0.266 s) | 0.44% | 0.81% | 0.60% | 0.62% |
| $^{177}$Hg (0.118 s) | 0.27% | 0.49% | 0.40% | 0.41% |

### 4.2.2 RIST ISOLDE and Ta129 targets

The method was also validated on other targets. The computed release curves are compared on Figure 4.20 with experimental data for solid targets with two different internal structures [129]. In both cases, the target material is contained in a 20-cm long Ta cylinder with a radius of 1 cm and operated

at T = 2400 K [129]. The first geometry (Ta129) shown in a simplified way in Fig. 2a consists of 200 Ta foils (2-µm thick, 15-cm long and 1-cm high) placed in the direction of the proton beam with 50-µm spacing between them. The second geometry (RIST-ISOLDE) shown in Fig. 2b consists of 3600 Ta annular discs( 25-µm thick, 9.5 mm external diameter and 2.5 mm internal diameter), placed perpendicular to the proton beam and spread over the entire length of the container.

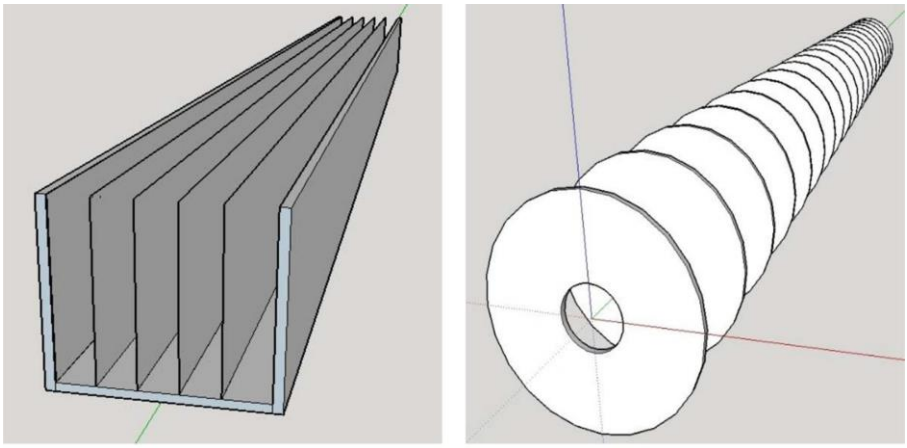

(a) Ta129 target geometry. (b) RIST-ISOLDE target geometry.

Figure 4.19: Representation of the different Ta-foils target geometries. The proton beam impinges parallel to the foils in geometry (a) and perpendicular in case (b). The number of foils and annular discs is reduced for visualization purposes.

In these two geometries, the thickness of each foil is much smaller than its other dimensions. Therefore, diffusion is only considered in the direction perpendicular to the surface of the foil. Similar to the previous section, the boundary and initial conditions are a constant surface-concentration and a uniform initial-concentration. Applying these in the solution of the one-dimensional form of Fick's second law of diffusion, one finds [86]:

$$C = \frac{4C_i}{\pi}\sum_{m=0}^{\infty}\frac{1}{2m+1}exp\left[-\frac{(2m+1)^2\pi^2 D}{l^2}t\right]\sin\left[\frac{(2m+1)\pi x}{l}\right]. \qquad (4.7)$$

In this expression, $x$ is the position along the main diffusion axis, perpendicular to the foils and $l$ is the foils thickness. The flux of particles at the surface of a foil $J$ is then derived as:

$$J(t_{fs}) = \frac{4C_i D}{l} \sum_{m=0}^{\infty} exp\left[-\frac{(2m+1)^2\pi^2 D}{l^2} t_{fs}\right], \tag{4.8}$$

where $t_{fs}$ is the diffusion time to the foil surface. The Monte carlo calculations for effusion are fitted as described in section 3.1.3.4 by the expression (3.30) with $\Delta t_{0ef} = 0$. Combining the diffusion and effusion models, the following expression is derived for the current of a stable nuclide at the ion source;

$$I(t_{is}) = \frac{8C_i D i}{l} \left\{ \begin{array}{l} \sum_{m=0}^{\infty} \left[ \frac{exp\left[-\frac{(2m+1)^2\pi^2 D}{l^2} t_{is}\right] - exp(-k t_{is})}{k - \frac{(2m+1)^2\pi^2 D}{l^2}} \right] \\ -\sum_{m=0}^{\infty} \left[ \frac{exp\left[-\frac{(2m+1)^2\pi^2 D}{l^2} t_{is}\right] - exp(-(j+k) t_{is})}{j + k - \frac{(2m+1)^2\pi^2 D}{l^2}} \right] \end{array} \right\}, \tag{4.9}$$

with $t_{is}$ the release time to the ion source, while $i$, $j$ and $k$ are effusion fit parameters defined with expression (3.30). A formulation in terms of current is used here rather than a probability density function as it is more suitable for comparison with experimental measurements which give as output a count rate. The release efficiency of nuclides out of the targets is then obtained as:

$$\varepsilon_{rel} = \frac{\int_0^{\infty} I(t_{is}) e^{-\lambda t_{is}} dt_{is}}{\int_0^{\infty} I(t_{is})\, dt_{is}} \tag{4.10}$$

For both of these geometries, experimental release curves were available in literature for the same isotope, $^{8}$Li. However, the diffusion coefficient for Li in Ta was not found in literature. As a consequence, the diffusion coefficient was considered a free parameter in the comparison with the experimental release curve of $^{8}$Li in the case of the Ta129 target and was determined by fitting the data. In the case of the RIST-ISOLDE target, the release curve was found to be much less sensitive to the value of the diffusion coefficient as compared to the Ta129-target geometry. A reliable determination of the diffusion coefficient through the same procedure was therefore prohibited. The diffusion coefficient value of 5.4 $10^{-14}$ $m^2/s$ determined for the Ta129 target was thus applied to the RIST-ISOLDE target (see Figure 4.20).

In both cases, a good match was obtained between the modelled release curve and the experimental points.

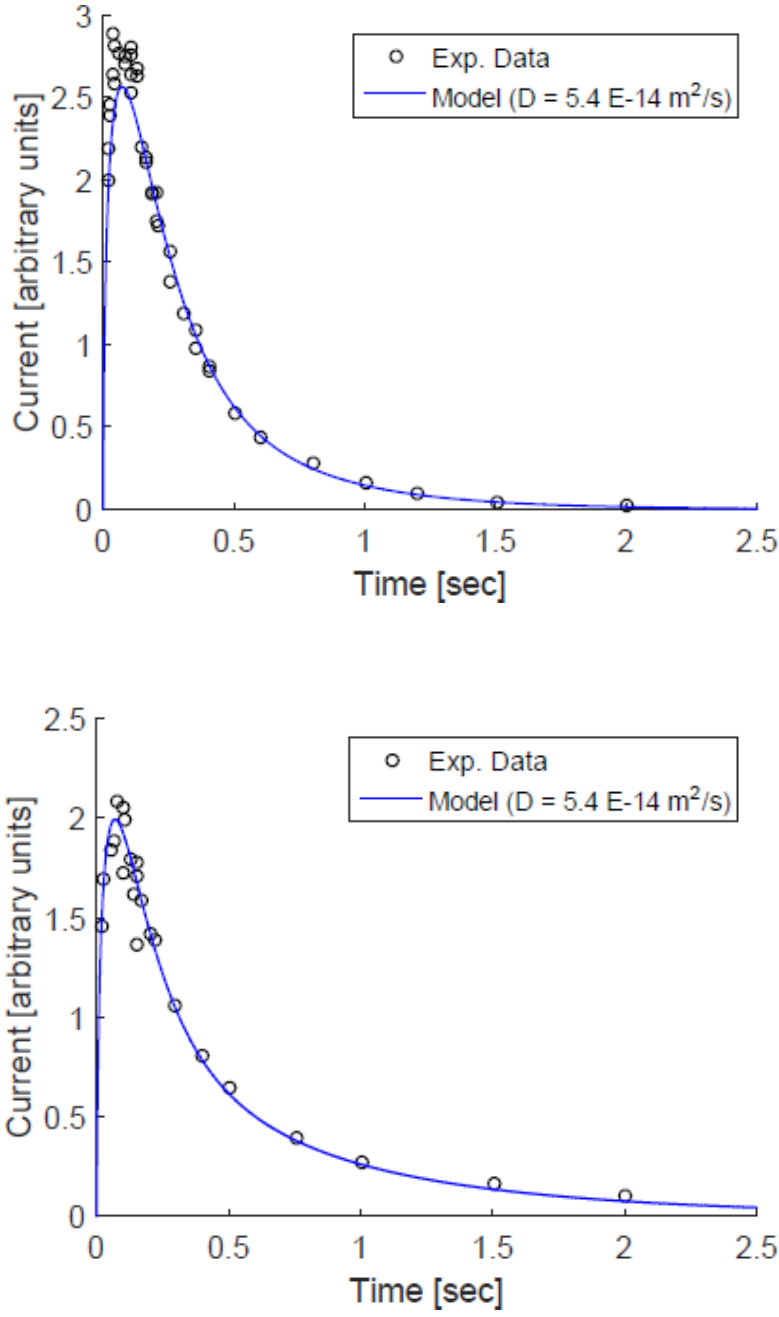


Figure 4.20: Computed and experimental normalized release curve of 8Li, (top) for the Ta129 target and (bottom) for the RIST-ISOLDE target using a diffusion coefficient (D = 5.4 10-14 $m^2s^{-1}$). Plots reproduced from [129].

## 4.3 Influence of geometrical parameters on the release efficiency

The influence the target geometry on the release efficiency of short lived Hg isotopes is investigated in this section.

### 4.3.1 Target length

In chapter 3, the nuclide-production rate inside an ISOL target is shown to scale with different parameters. Among these, cross sections are nature-given values for a specific target beam configuration and little can be done concerning the primary-beam intensity at a given facility. Still, an increase of the in-target production rate of nuclides can be achieved through an increase of the number of target atoms exposed to the primary beam. Such an increase of the number of target atoms exposed to the primary beam can be obtained by increasing the length of the target.

However, while passing through a dense target material, both the mean energy and fluence of a proton beam decrease due to the stopping power and scattering in dense target material. The production rate per unit volume of a constant-density target material is therefore expected to gradually diminish along the target. This phenomenon is visible in the plot of the in-target production-density of Hg isotopes along the target-length, shown on Figure 4.21. These calculation results, obtained with two different Monte Carlo codes (FLUKA and MCNP [130]) are shown for comparison. Even though at high energies, different models are used in these codes for proton-induced reaction cross sections, the results are in good agreement. This means that the gain in in-target production of Hg isotopes per unit length of the irradiation volume decreases as well for long targets, see Figure 4.22 (left).

On the other hand longer targets result in correspondingly larger release volumes which will increase the effusion path and thus the delay losses of short-lived nuclei. Combined, these two effects imply that an optimum target length exists. This optimum depends, among other factors, on the beam energy, the density of the target material and the energy dependence of the production cross sections. By increasing the length of the irradiation volume and hence the length of the release volume, the efficiency of the target is decreased as shown on the right hand side of Figure 4.22 for short-lived Hg isotopes.

Combining the evolution of both the in-target production with release efficiencies as a function of the target length, the optimum length of the target for production of $^{177}$Hg and $^{178}$Hg was found to be about 10 cm. Even though the optimum is half-life dependent, in these cases, a target optimized for one isotope would still produce significant amounts of the second.

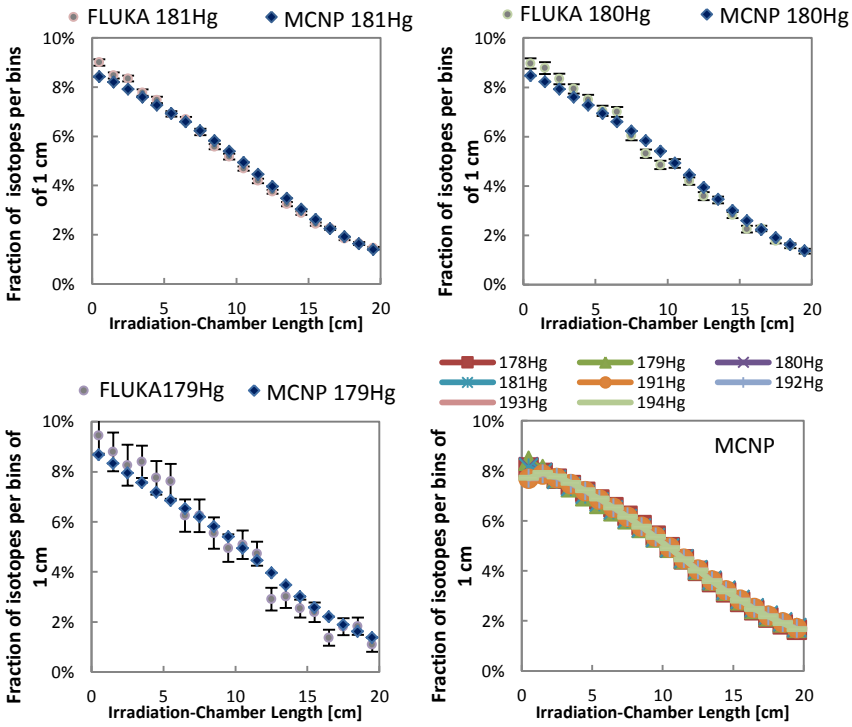


Figure 4.21: Fraction of several Hg isotopes produced per bins of 1 cm, along the length of the target. Results from FLUKA and MCNP [130] are given for comparison.

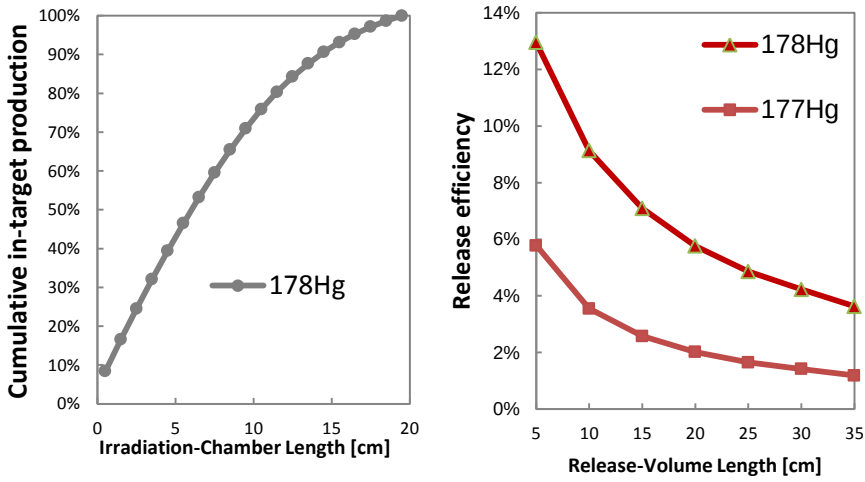


Figure 4.22: (Left) Cumulative in-target production of $^{178}$Hg isotopes along the 20-cm long irradiation chamber. (Right) $^{177, 178}$Hg release efficiency of the target for different values of release-volume length.

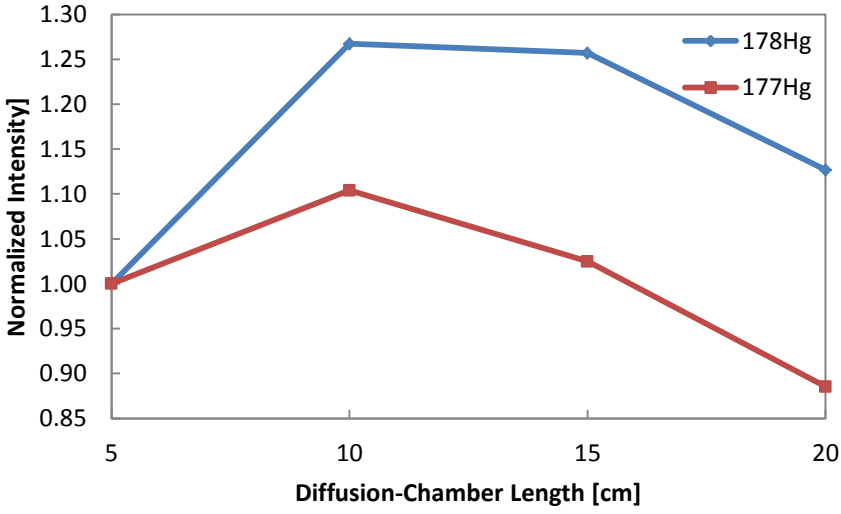


Figure 4.23: Normalized intensity of $^{178}$Hg (left) and $^{177}$Hg (right) RIBs for different lengths of the irradiation and release volumes.

### 4.3.2 Release volume height

A second parameter of interest is the height of the diffusion chamber. A smaller height of the diffusion chamber increases the effusion efficiency as it means a smaller release volume. However a smaller height of the diffusion chamber also reduces the efficiency of the diffusion process as it provides

less fall-time for the droplets. This explains the presence of an optimum diffusion-chamber height on Figure 4.24. For the production of $^{179}$Hg ($t_{1/2}$ = 1.05 s) an optimum diffusion-chamber height of ~ 9 cm was determined while the optimum values for $^{178}$Hg ($t_{1/2}$ = 0.266 s) and $^{177}$Hg ($t_{1/2}$ = 0.118 s) are around 3 cm.

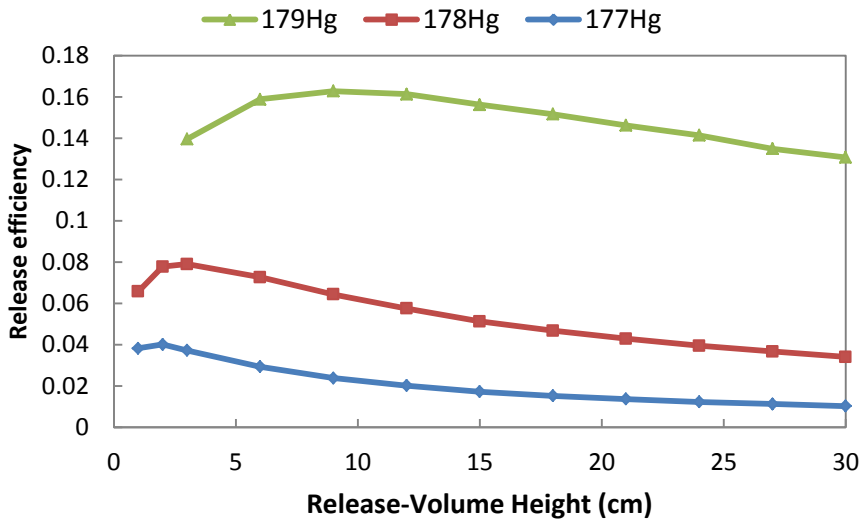


Figure 4.24: $^{177\text{-}179}$Hg Release efficiency of the target for different values of release volume height.

### 4.3.3 Droplets radii

A third parameter studied is the radii of the droplets. Larger droplets reduce the diffusion efficiency but are expected to increase the effusion efficiency by reducing the number of droplets in the release volume. Indeed, a larger number of droplets means more obstacles on the track of particles which will increase the mean number of collisions. Simulations were therefore run for droplet radii ranging from 200 to 50 µm. The number of evacuation apertures is adapted in these simulations in order to keep the overall area of the evacuation apertures, and thus the flow rate and full-evacuation time of LBE out of the irradiation volume constant. The results shown in Table 4.2 indicate that the release efficiency of $^{177}$Hg increased while reducing the droplets radii from 200 to 50 µm. This monotonous increase is explained by the fact that the ***pdf*** of the effusion process is not significantly affected by the radii of the cylinders on this range (see Figure 4.25), while the diffusion efficiency is increased for smaller droplets.

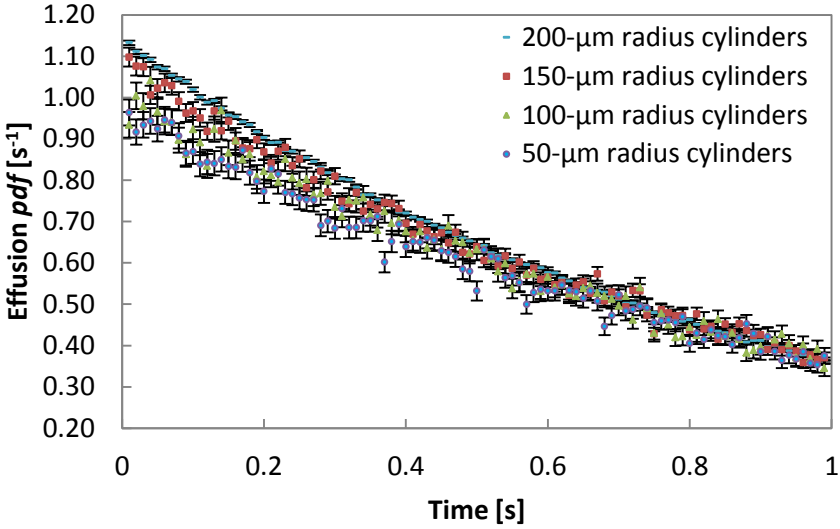


Figure 4.25: Effusion pdfs, with droplet radii ranging from 200 to 50 µm. The larger uncertainties on the data for droplet radii ranging from 150 to 50 µm are related to the fact that the computation time scales inversely with the square of the transparent-cylinders radii.

Indeed, though the simulation of more droplets significantly increases the mean number of collisions during effusion, this increase is compensated in a great part by the reduced values of the mean free path between two consecutive collisions (see Table 4.2). These results seem to indicate that the optimum droplet radius is below 50 µm.

Table 4.2: Simulation results for droplet radii ranging from 200 to 50 µm.

| | 200-µm radius cylinders | 150-µm radius cylinders | 100-µm radius cylinders | 50-µm radius cylinders |
|---|---|---|---|---|
| Release Efficiency (%) | 2 | 2.7 | 3.7 | 5.7 |
| Mean Pumping Path (cm) | 18812.9 | 17190.9 | 17357.7 | 17580 |
| Mean Free Path (cm) | 0.624 | 0.496 | 0.352 | 0.187 |
| Mean Number of collisions | 30138 | 34681 | 49366 | 93891 |

## 4.4 Improved geometry of the release volume

From the studies presented in the previous section, a more compact geometry of the release volume (Figure 4.26) has been investigated. A release efficiency of 9.6 % is computed for the target with this release volume. It corresponds to an increase of a factor 3.4 of the target yield as compared to the initial geometry. However the formation of 50-µm radius droplets constitutes a major challenge for the feasibility of this target geometry.

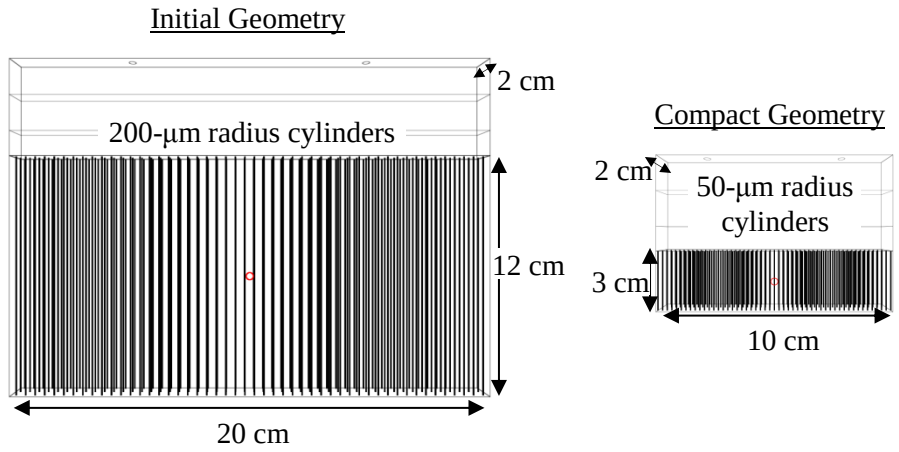


Figure 4.26: Compact geometry for the release volume. The initial geometry is shown for comparison.

## 4.5 Conclusion

In this chapter, the method described in chapter 3 for modeling the release of nuclides out of an ISOL target is applied. Validation of the method through comparison of its outputs to experimental data is conducted. In the absence of experimental data for a loop target the validation cases were the static-bath ISOLDE-SC Pb target and two solid Ta foils targets with different internal geometries. In all these cases, a good match between computed and experimental release curves and efficiencies has been observed for a variety of isotopes of different elements.

In the proposed method, the effusion step is modeled through Monte Carlo simulations which are typically long to run. Because of its large size and complexity, the simulation case for the loop target required different

simplifications and approximations of which the validity was checked in this chapter. Beside studying the influence of several effects not specifically modelled, this section also provided some insight into the physics behind the effusion-fit parameters. An attempt to further understand this physics would require a more systematic study of the effusion process than possible within the framework of this thesis.

In the last part of the chapter, the proposed method is applied to optimize the design of a molten LBE loop target. Optima of different parameters have been determined and it was found that the optimum size of the target is species and half-life dependent. In addition, the shorter the half-life of the isotope of interest, the more compact is the optimum target design. However, to obtain a globally optimum design, a multi-dimensional study is required where all the design parameters will be allowed to vary.

# 5 CFD analysis of beam-target interactions

In the context of the next generation of RIB facilities based on the ISOL method, development of production targets capable of dissipating the high power deposited by the primary beam is a major, ongoing task. These targets should withstand the high-power primary beams without compromising the reliability of the yields and the structural integrity of the target itself over extended periods of time. The LBE loop target studied in this work is one such target developed e.g. for the EURISOL and ISOL@MYRRHA facilities.

Since this target is of interest for different institutes, its detail design and prototyping is conducted within the Liquid Eutectic Lead Bismuth Loop Target for EURISOL (LIEBE) project. The pump and heat exchanger are designed by the Institute of Physics of the University of Latvia (IPUL) and CERN respectively. Online tests of the prototype will be conducted at CERN-ISOLDE. However, EURISOL envisages a CW beam while ISOLDE operates with a pulsed beam. Specific issues related to the pulsed-beam of ISOLDE are studied in this chapter for the prototype.

As a consequence of interaction of the highly pulsed 1.4-GeV protons at ISOLDE with the target, heat powers of the order of 2 GW would be instantaneously deposited in the target during a bunch. This sudden insertion of significant amounts of heat in the target is expected to result into pressure waves, propagating in the liquid target material and potentially reflecting at its boundaries. The reflection of pressure waves at different boundaries encountered in the geometry of the irradiation volume is studied in the first part of the chapter.

Because the propagation of pressure waves in the target material induces dynamic loads on the target container, the safe operation of the target requires the demonstration of its structural integrity under the conditions of the online test. As a first step in this direction, conjugate flow (CFD) and heat deposition (Monte Carlo) calculations have been conducted, not accounting for fluid-structure interactions.

## 5.1 Wave reflection at boundaries

In chapter 2, LBE flow calculations inside the irradiation volume of the target have been presented. In these calculations, the LBE domain is limited by boundaries including rigid walls, velocity inlets and pressure outlets. Because of the computational cost, especially in complex geometries, these CFD simulations have been limited to the most relevant regions of the flow domain. The velocity inlets and pressure outlets are therefore not real physical boundaries of the LBE flow. If this modeling of the computational boundaries is compatible with the LBE flow calculations, its applicability to beam target interaction calculations has to be checked.

To investigate wave reflection at the three boundaries mentioned above, simulations were run to model the Joukowski pressure jump resulting from the sudden closure of a valve in the middle of a tube. A velocity inlet boundary condition was set at one end of the tube while the other end was modeled as a pressure outlet. The valve at the middle of the tube represents a wall. Via the method of the characteristics [131], the expected velocity and pressures in the wave after reflection at these boundaries can be estimated for comparison with the computed values. The influence of friction is not included in these calculations. The mesh and initial conditions of the calculations are shown on Figure 5.1.

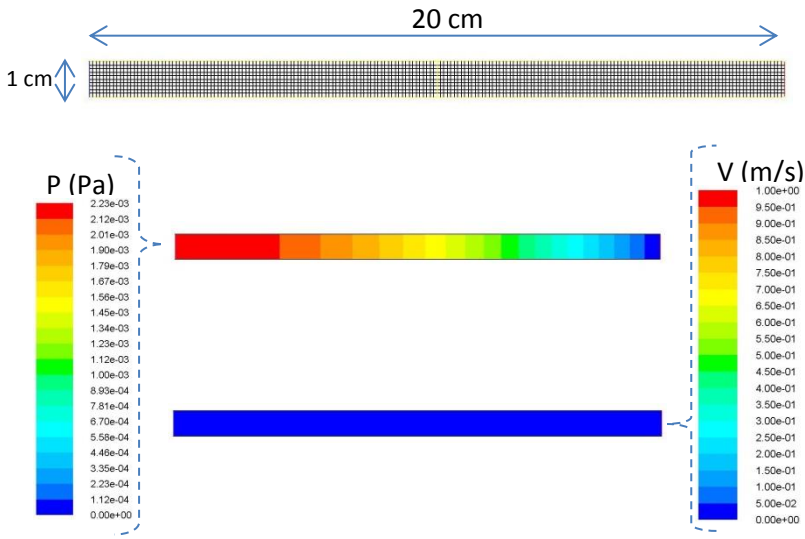


Figure 5.1: Mesh and initial conditions of the Joukowski pressure jump calculations.

The sudden closure of the valve at the center generates two pressure waves, a compression wave travelling toward the velocity inlet at the left end of the tube and an expansion wave travelling in the direction of the pressure outlet at the right end of the tube. From the method of the characteristics, the pressures in the compression $P_{L1}$ and expansion $P_{R1}$ waves are estimated to be:

$$P_{L1} = P_{L0} + \rho c_{eff} v_{L0} \quad \& \quad P_{R1} = P_{R0} - \rho c_{eff} v_{R0} \tag{5.1}$$

With $P_{L0} = P_{R0}$ the pressure at the center of the tube before closure of the valve, $P_{L1}$ & $P_{R1}$ the respective pressures on the left and right hand side of the closed valve, $v_{L0} = v_{R0}$ the velocity at the center of the tube before closure of the valve, $\rho$ the density of LBE and $c_{eff}$ the propagation speed of the waves which in this case is the speed of sound since rigid tube walls are considered. The velocities $v_{R1}$ and $v_{L1}$ in the wave after closure of the valve are considered equal to zero. The values of $P_{L1} = 1.829\ 10^5$ Pa & $P_{R1} = -1.829\ 10^5$ Pa derived from expression (5.1) for LBE at 500 K match well the results obtained with the CFD calculations (see Figure 5.2).

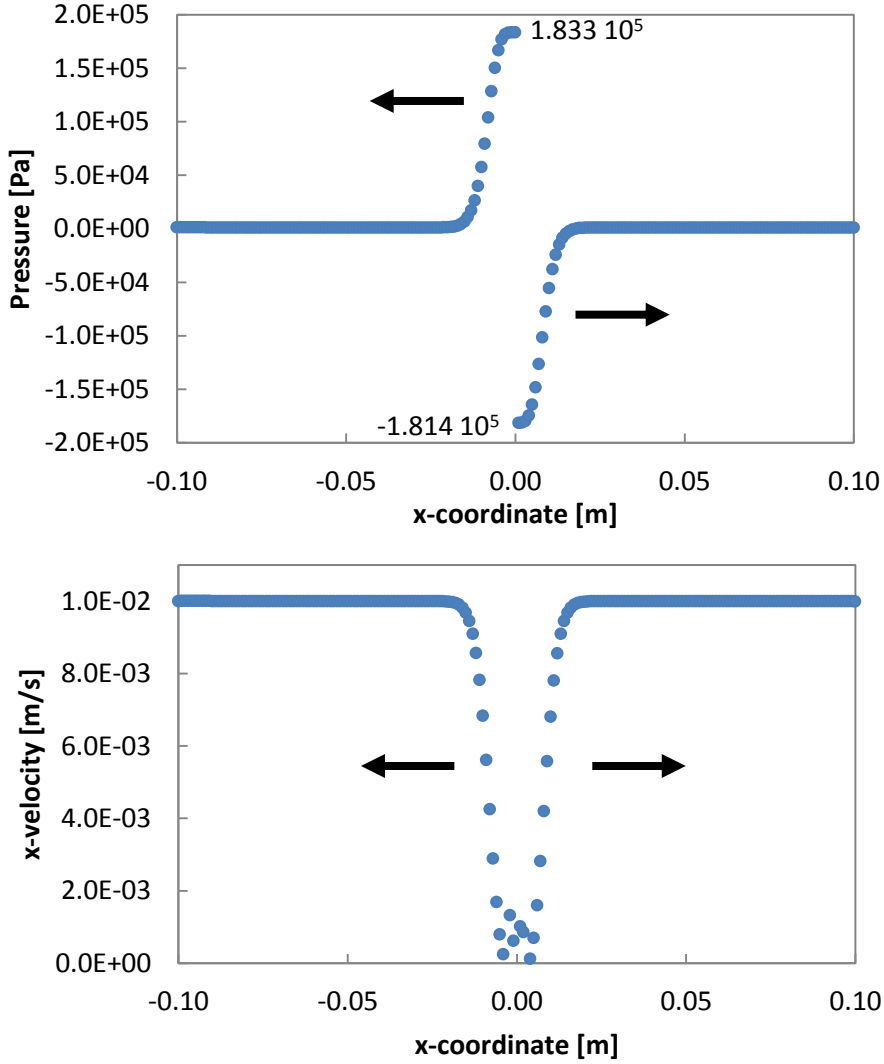


Figure 5.2: Centerline pressure & velocity distribution (node values) 5 μs after valve closure.

At the pressure outlet, right end of the tube, the expansion wave is expected to reflect as a compression wave with a velocity $v_{R2} = 2v_{R1} - v_{R0}$ and a pressure $P_{R2} = P_{R0}$. This simulates an open end where the pressure is prescribed. As a velocity is imposed at the velocity inlet of the tube, the compression wave is expected to reflect at this end as a compression wave with a velocity $v_{L2} = v_{L0}$ and a pressure $P_{L2} = 2P_{L1} - P_{L0}$. Figure 5.3 shows that the CFD calculations agree well with the pressure values

$P_{R2} = 10^3$ Pa and $P_{L2} = 3.659\ 10^5$ Pa. The reflection at the velocity inlet is the same as one would expect from a physically closed end.

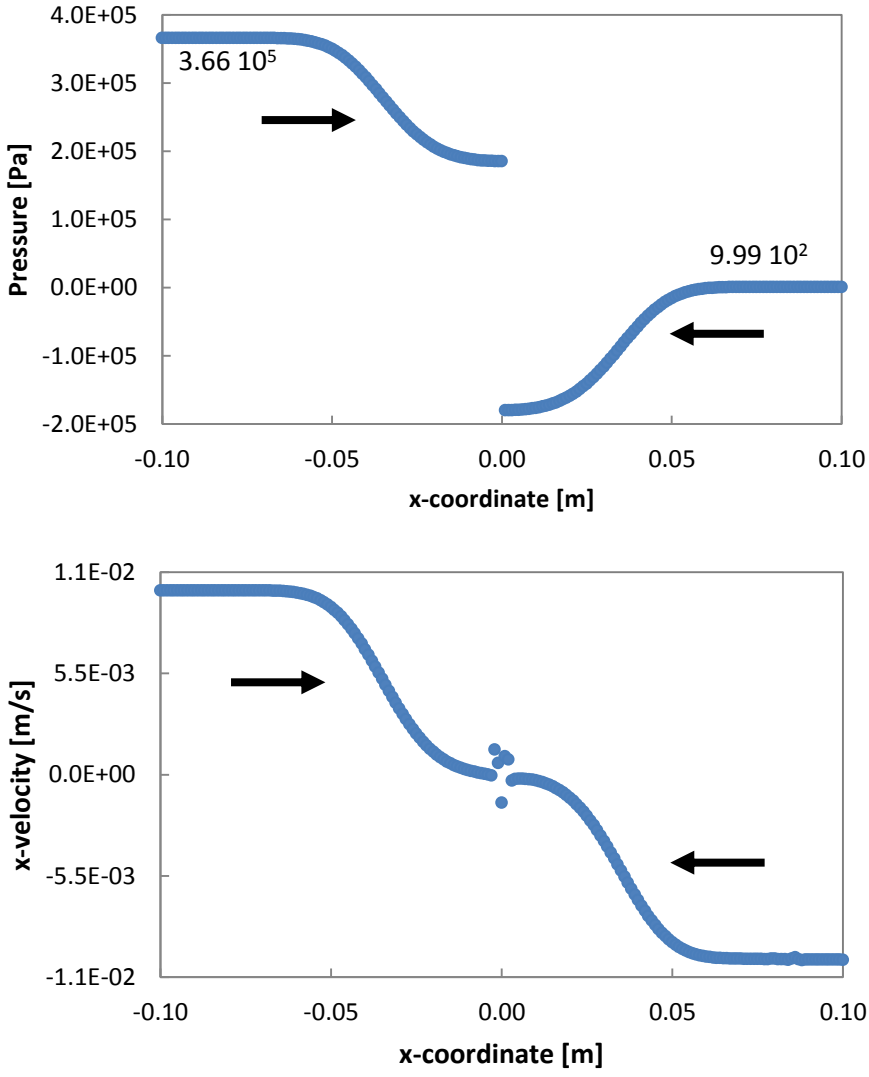


Figure 5.3: Centerline pressure & velocity distribution (node values) 95 μs after valve closure.

The two compression waves resulting from reflection at the ends of the tube travel back toward the valve. After reflection of these on the valve, two compression waves in the opposite direction are expected, with $P_{R3} = 2P_{R2} - P_{R1}$ and $P_{L3} = 2P_{L2} - P_{L1}$. The comparable results obtained with CFD calculations are shown on Figure 5.4.

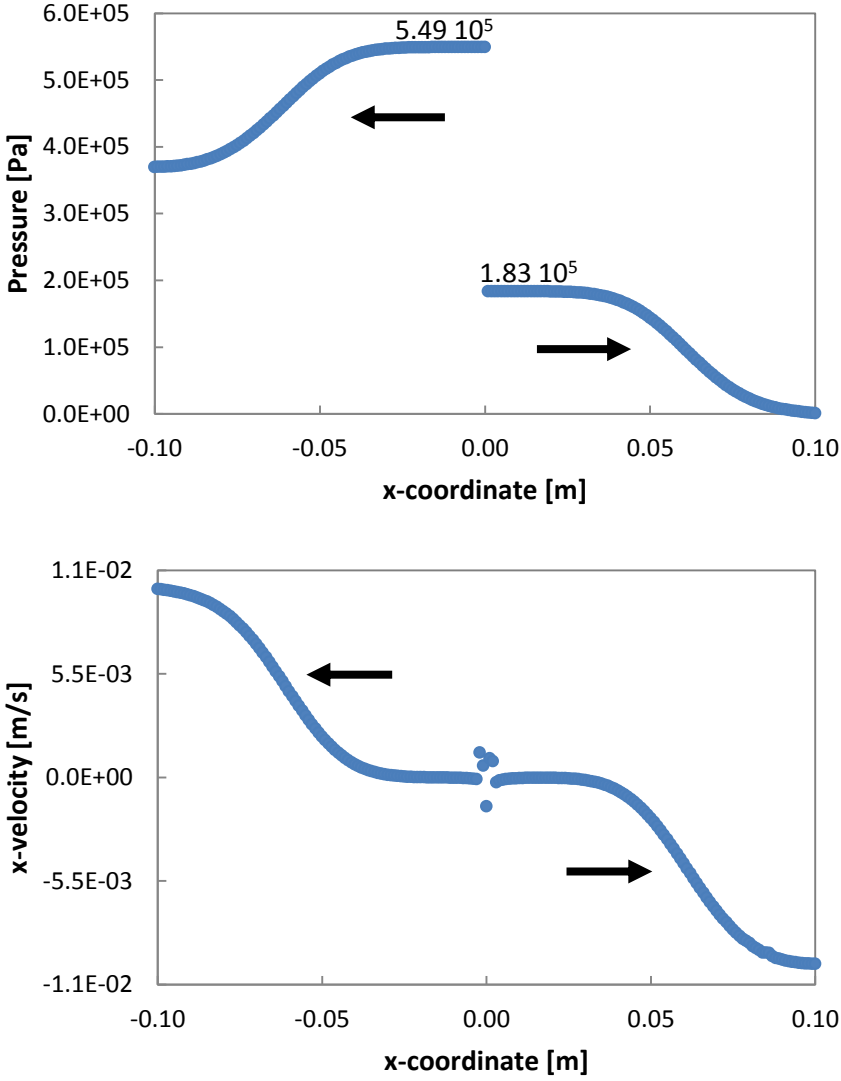


Figure 5.4: Centerline pressure & velocity distribution (node values) 150 µs after valve closure.

On Figure 5.2 through Figure 5.4, a discrepancy can be observed in the velocity distribution around x = 0 m. This discrepancy is explained by the use of a pressure interpolation scheme that is not monotonicity preserving.

## 5.2 Proton-target interaction

Prototypes of the target will be tested at CERN-ISOLDE, where the available proton beam is of similar energy (1.4 GeV) as foreseen for

EURISOL (1 GeV). The proton beam energy is an important parameter for the choice of the online test facility as the spatial distribution of the in-target production rate of exotic Hg isotopes depends significantly on it. Indeed, calculations of the spatial distribution of the in-target production rate of $^{180}$Hg at 0.5, 1, 1.5 and 2 GeV [132] indicate that the spatial distribution at 1 GeV is most closely reproduced by results at 1.5 GeV. In addition, virtually no production of Hg isotopes lighter than $^{179}$Hg is expected at 0.5 GeV [132] while $^{177}$Hg is the reference isotope for this target. Furthermore, because of the larger beam spot foreseen for EURISOL ($\sigma$ = 3 - 20 mm [49]), energy-deposition-density values are closer at the two facilities than one can infer simply from beam intensities (see Figure 5.5).

The beam parameters used in the simulations correspond to the staggered mode at ISOLDE. Energy deposition was computed with FLUKA [133] and a peak value around 8 $10^{-2}$ GeV/(cm$^3$.proton) was determined. As a comparison, the energy deposition from a 1 GeV EURISOL proton beam ($\sigma$ = 3 & 20 mm) is also shown on Figure 5.5. It shows that because the peak energy-deposition-density per proton is one to three orders of magnitude lower under EURISOL conditions, ISOLDE beam conditions are comparable in energy-deposition-density to those at EURISOL although the proton intensity is two orders of magnitude lower.

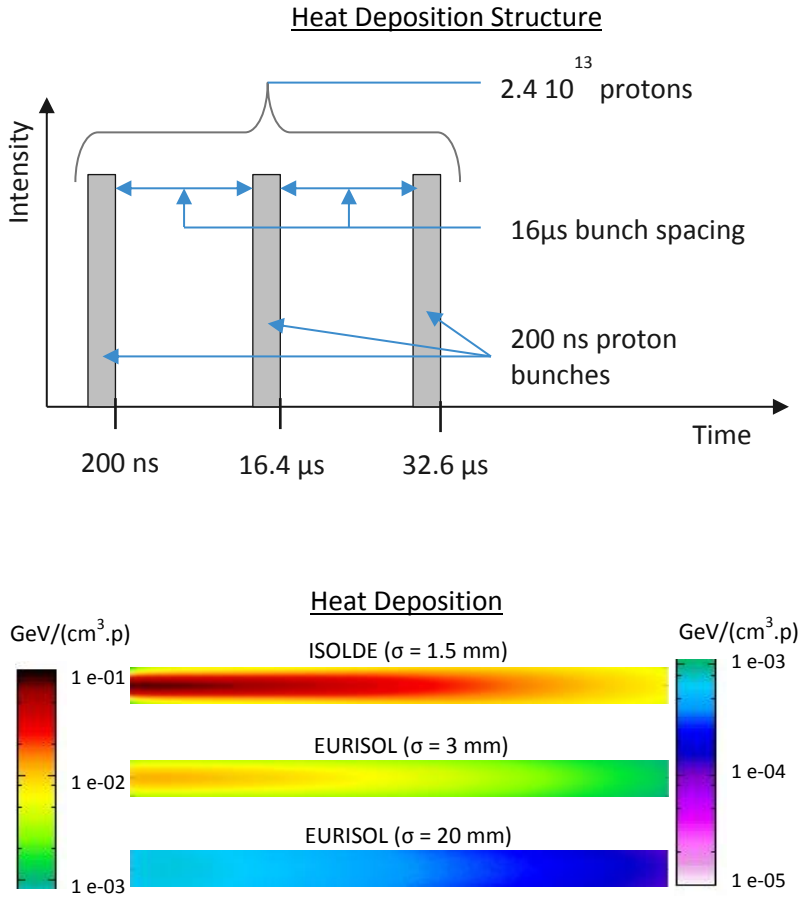


Figure 5.5: ISOLDE Staggered mode beam parameters (top) & Heat deposition (bottom). Computed heat-deposition plots for EURISOL are also shown.

The resulting power densities were imported in Fluent and applied with a trilinear interpolation method as an input internal energy load for the computation of pressure waves. The scoring bins in FLUKA are rectangular cuboids while a tetrahedral meshing is used in Fluent. The power density is assumed constant with time within a bunch. Temperature profiles similar to the heat deposition are obtained as shown on Figure 5.6 at the end of a bunch. The maximum temperature-increase due to a single bunch of 8 $10^{12}$ protons amounts to ~ 60 K. The following linear equation of state with pressure and temperature dependence is used:

$$\rho = \rho_0 + \left(\frac{\partial \rho}{\partial T}\right)_0 (T - T_0) + \frac{1}{c_0^2}(p - p_0) \qquad (5.2)$$

where the reference parameters $\rho_0 = 10496.4$ kg/m$^3$, $c_0 = 1762.5$ m/s, $T_0 = 453$ K, $p_0 = 10^5$ Pa and $\left(\frac{\partial \rho}{\partial T}\right)_0 = -1.3236$ kg/m$^3$K from [69] were used. The temperature dependence from reference [69] is implemented for both density and viscosity. The inlet sections are modeled with a characteristic boundary condition so that waves leave the computational domain without reflection. At the outlet sections, the pressure-outlet boundary is maintained.

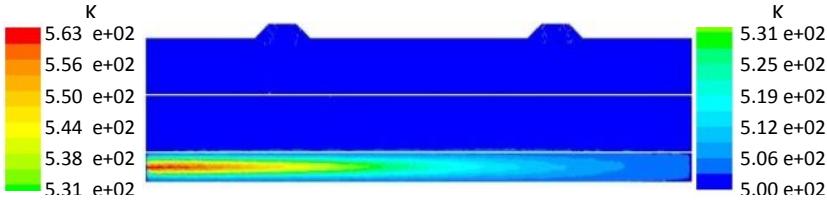


Figure 5.6: Temperature profile (on symmetry plane), shown in the geometry of concept 5 defined in chapter 2.

Figure 5.7 presents the pressure profiles computed in the LBE after each bunch for concepts 5 and 6 (Chapter 2). The energy deposition from each proton bunch generates a compression wave inside the irradiation volume. These waves travel in the LBE with a peak pressure value decreasing mostly as a function of the distance from the proton beam center line. The initial compression waves are also closely followed by expansion waves.

The peak value of the pressure profile at the end of a bunch is increased by ~43% (resp. ~30%) after the second bunch as compared to the first in the parallelepiped-shape feeder volume concept (resp. the prism-shape feeder volume concept). Between proton bunches 2 and 3, the increase in peak pressure value is of ~3% and 18% respectively. These values indicate no sign of severe constructive interference with the 16.2-µs bunch spacing used. Indeed, by the time a bunch arrives, the pressure wave generated by the previous bunch has already travelled into the feeder volume.

It can be noticed on Figure 5.7 that pressure values below the vapor pressure of LBE (~ 10-6 Pa at 600 K) are reached in the expansion waves. These low pressures would initiate cavitation, not modeled in this study.

Parallelepiped-shape feeder volume

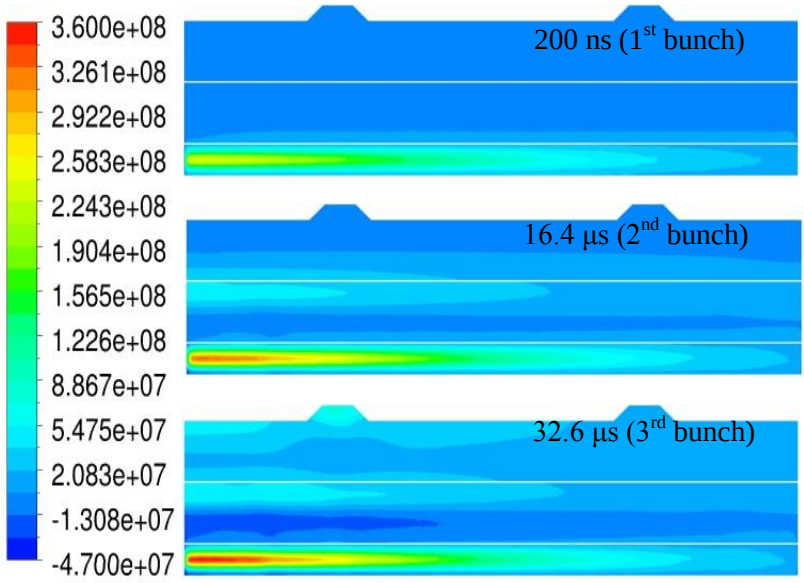


Prism-shape feeder volume

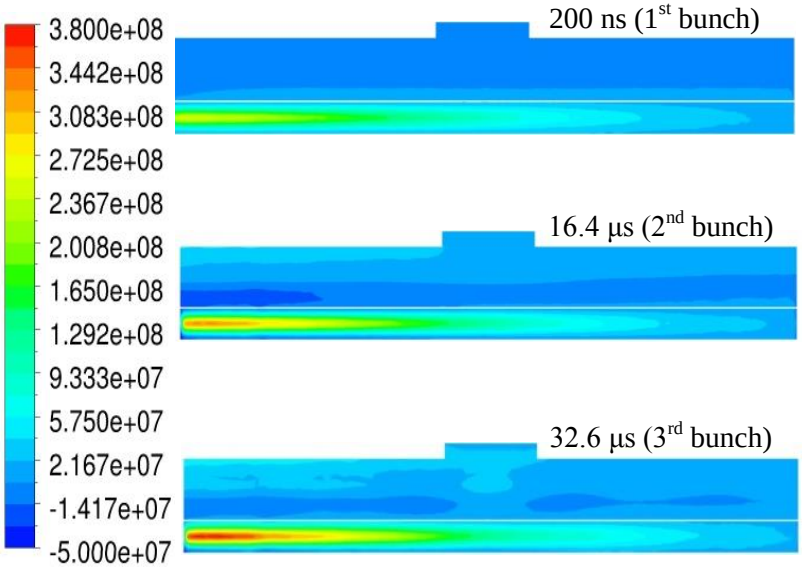


Figure 5.7: Pressure profile inside the LBE for both concepts (on symmetry plane) in Pa.

Cavitation in this case will have the dual effect of changing the time structure of wave propagation while reducing the amplitude of subsequent waves travelling through such a zone. Modeling cavitation in a later stage would therefore modify the computed percentages of increase in peak pressure value.

As the container is not explicitly modeled in these CFD simulations, it is treated as a rigid body for the flow calculations. Calculations of stresses and strains in the container require fluid structure interactions calculations that fall out of the scope of the work reported in this chapter.

## 5.3 Conclusion

This chapter presents pressure waves simulations for the LIEBE prototype of the LBE loop target. These calculations provide insight into effects generated by proton-induced shocks in this liquid metal target under a highly pulsed beam. These simulations show that strong pressure waves develop in the target but no severe constructive interference is expected from the 16.2-μs bunch spacing of the beam. The latter conclusion however needs to be further investigated in more comprehensive calculations accounting for potential cavitation effects as well as fluid structure interactions.

# 6 Conclusion and Outlook

## 6.1 Synthesis and conclusions

Judging from the imbalance between the average numbers of requested and delivered RIB hours per year, ISOL facilities are significantly oversubscribed [72]. Part of this imbalance can be explained by the need for significant R&D in order to deliver RIBs of certain nuclides. Indeed, though of high interest, RIBs of nuclides in several regions of the nuclear chart are currently not or very poorly produced (see Figure 6.1).

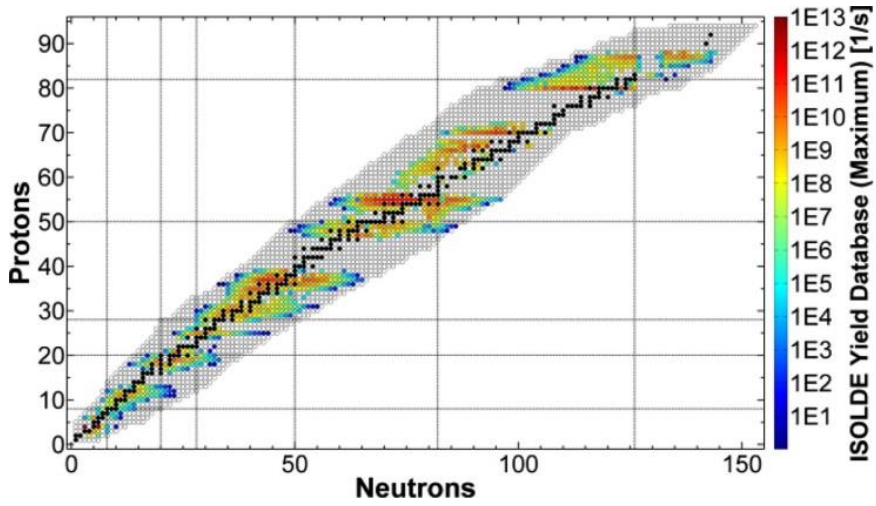


Figure 6.1: (Reproduced from [72]) RIB intensity distribution over the nuclear chart as reported in the ISOLDE Yield Database [134]. If several yields are reported for one isotope the maximum entry was used.

As a consequence, new facilities are under design and construction all over the world, e.g. ARIEL-TRIUMF (Canada) [135], HIE-ISOLDE CERN (Switzerland) [136], RISP-IBS (Korea) [137], SPES-INFN (Italy) [138], SPIRAL 2- GANIL (France) [139].

In order to increase the intensity of RIBs by the several orders of magnitude requested for certain experiments, a new generation of ISOL-based RIB facilities is currently under study worldwide. A distinct feature of these facilities is their foreseen high-power driver beam which indicates a need for

development of a new generation of targets capable to operate under this high-power condition.

The proposed concept of a liquid-metal-loop target is therefore of interest for EURISOL and ISOL@MYRRHA. This target concept is expected to handle the high primary-beam power because the target material flows in a loop equipped with a heat exchanger. In addition, liquid targets typically offer the highest thicknesses of any material ( ~200 g/cm$^2$ for Lead Bismuth Eutectic (LBE)), leading to higher in-target production rates for the isotopes of interest. Concerns for the design of this target include effects like pressure drop, cavitation, liquid-metal recirculation, instabilities and non-uniform flows. These concerns are most crucial inside the irradiation volume of the target, as they can significantly affect the performance of the target. Indeed, the main design requirement of the irradiation volume of the target is a complete evacuation of the irradiated LBE from the irradiation volume within 100 ms after the impact of a proton pulse. To ensure a proper design meeting this requirement, the dynamics of LBE in the irradiation volume was studied with CFD simulations. CFD simulation was used as the method avoids the lengthy and costly process of prototyping and testing every investigated design.

Starting from a simple cylindrical geometry, several improved layouts of the irradiation volume have been studied. Several issues have been revealed through simulations of the LBE-flow inside the starting-case geometries proposed for the irradiation volume. The available amount of data resulting from these initial simulations provided a unique insight on the causes and potential solutions of these issues. As a result, a key feature of the optimized concepts is the need for a set of feeder volumes and feeder grids. In each of the proposed satisfactory geometries, the inlet-jet effect was solved with a combination of two approaches: (1) increasing the size of inlet sections in order to reduce inlet velocities; (2) opposing one or two feeder grids to distribute the inlet jet over the length of the irradiation volume. With this strategy, within a compact geometry, the jet flow with high-momentum that enters at the inlets is transformed into a uniform flow in the irradiation volume and at evacuation. Issues of low-pressure zones have been solved by avoiding unnecessary bending of the flow inside the compact geometry of the target. The concept with a parallelepiped-shape feeder proved to be the most robust of the satisfactory concepts, with regards to risks of clogging. It has been constructed at CERN as part of the LIEBE prototype.

Upon irradiation by a proton pulse, the liquid target material is spread into a shower of droplets inside the release volume. The need to optimize the release volume of the target derives from the fact that the main objective of this target is the production of RIBs of short-lived Hg isotopes with $^{177}$Hg ($t_{1/2}$ = 0.118 s) as reference. The production of RIBs of such exotic nuclides, away from the valley of stability, is often confronted with several issues stemming from the very low production cross sections, the massive production of undesirable species and the short half-lives of the nuclides of interest. A sound engineering of the release volume is therefore crucial in order to minimize decay losses during the release of these nuclides. In this objective, a proper modeling of the release of nuclides out of the target is a requisite. A computational approach to predict the release of nuclides out of the target and to assess its efficiency has been developed. In this method, existing analytical descriptions of the diffusion process are used, in combination with an analytical fit of the numerical distribution obtained from Monte Carlo simulations for the effusion process. This gives as output an analytical model supported by detailed Monte Carlo calculations. This approach therefore combines the advantages of an analytical solution with the benefits of the supporting detailed Monte Carlo (MC) calculations. The analytical description used has the advantage that it implies no cutoff of the distribution tail as it is the case with a numerical convolution or the diffusion sampling approach. This results in a more accurate computation of the release efficiency.

The proper test case for validation of the proposed release model is a loop-type target. In the absence of experimental data for such a target, the validation cases were the static bath ISOLDE-SC Pb target and two solid Ta foils targets with different internal geometries. In all these cases, a good match between computed and experimental release curves and efficiencies has been observed for a variety of isotopes of different elements.

In the proposed method, the effusion step is modeled through Monte Carlo simulations which are typically long to run. Because of its large size and complexity, the simulation case for the loop target required different simplifications and approximations of which the validity was checked. Besides, through the study of the influence of these effects, insight can be gained into the physics behind the effusion fit parameters. The proposed method was then applied to optimize the design of a molten LBE loop target. Optima of different parameters have been determined and it was found that the optimum size of the target is species and half-life dependent. The shorter the half-life of the isotope of interest, the more compact the

optimum target design has to be. However, to obtain a globally optimum design of the release volume, a multi-dimensional study is required where all the design parameters are allowed to vary.

When passing through the target material, the driver beam can deposit significant amounts of energy in the target through Coulomb interactions. The energy loss profile was computed with FLUKA, a Monte Carlo code for particle transport in matter. This profile was then used to calculate initial temperature and pressure distributions in the target using Fluent. These calculations provide insight into effects generated by proton-induced shocks in this liquid metal target under a highly pulsed beam. The simulations show that strong pressure waves develop in the target but no severe constructive interference is expected from the 16.2-μs bunch spacing of the beam.

## 6.2 Outlook

Effusion is a crucial process typically present in all ISOL targets. Modeling this process in the complex geometries of ISOL targets requires the use of Monte Carlo tools. Also, these MC calculations often need to be long in order to achieve decent uncertainty levels. In addition, in the design & optimization process of targets, several design options need to be evaluated and the long MC calculations are to be repeated every time. One solution to reduce the time requirement of target design & optimization would be to propose accurate analytical descriptions of the process without a need to go through the MC calculations. As a first step in this direction, the analytical fit to numerical effusion delay time distribution developed in this work can provide insight into simple dependencies of the effusion process on some geometrical parameters. The repeated MC calculations for some design options would then become unnecessary to assess the changes in the effusion delay time distribution for these design options. This, however, requires a systematic study of the dependence of the effusion delay time distribution on parameters like the effusion volume and the pumping aperture size. Eventually, enough knowledge could be gained on the effusion process to predict the parameters in expressions (3.30) and (3.31) without going through a fitting to the MC calculations results. Besides, a global optimum design of the release volume of the LBE loop target for the production of a given isotope is still to be found.

Despite this optimization work, the production of RIBs of elements like Au and Pt out of an LBE target will still remain a challenge due physicochemical properties of these elements. Similarly to other liquid

targets, the LBE targets suffer from a limited release of elements less volatile than the target material, even though some isotopes of some of these elements are produced in large amounts in the target. The typical solution for this issue is to find molecular compounds of these elements that are more volatile than the target material and are stable enough at elevated temperatures. The search for molecular compounds gains in interest now that an improved design of a liquid target is available. By supplying the proper reactant through the target, transfer line or container material, significant gains in performance could be achieved for the production of RIBs of non-volatile elements out of a loop target. Besides, the maximum operating pressure of the ion source used ($10^{-4}$ – $10^{-2}$ mbar, [140, 141]) is often the limiting factor for operation of molten metal targets at high temperatures. Indeed, the maximum operation temperature of these targets is defined by the rate of evaporation of the target material that along with the flow of radioactive nuclei should not exceed $10^{-8}$ mol.s$^{-1}$ [140]. For this reason, molten lead targets at ISOLDE were equipped with a temperature controlled chimney between the target container and the ion source to prevent large amounts of target material from reaching the ion source [30]. However to our knowledge, the geometry of the gas flow inside this chimney has never been studied in detail and optimized. Since an increase in the flow of radioactive nuclei is expected with the LBE loop target, the optimization of the design of this chimney becomes more crucial. Such an optimization can be performed with the help of MC codes for molecular/transitional flow calculations.

The target design should also ensure that during operation, the target and container are sufficiently strong to withstand stresses without the onset of failures. Since in liquid targets the disruption of the liquid is not as such of structural concern the main requisite is the structural integrity of the container. As a first step toward assessing the stress level in the container, the pressure waves generated in the liquid target and resulting from primary beam impact have been computed. Potential cavitation effects as well as fluid structure interactions should now be included in this calculation to determine the evolution of stresses in the target container. In addition, strain-rate dependent failure criteria and material modeling are required.

From the application point of view, one major perspective of this LBE loop target is the production of isotopes of At, one of the rarest elements naturally occurring on earth [142]. The isotope $^{211}$At ($t_{1/2}$ = 7.2 h) is of significant interest for pharmaceutical use as an agent for targeted alpha therapy in cancer treatment. The knowledge of basic chemical properties is

absolutely necessary for this medical application, but their measurement is hindered as the estimated total abundance of At on earth is 0.07 g [142]. The study of the fundamental atomic properties of the element thus relies on artificially produced At. $^{211}$At is typically produced in a batch process through irradiation of solid Bi with alpha beams, followed by dry distillation for extraction. However, At being a halogen with high volatility, an alternative method could be the online separation of At isotopes from a liquid Bi or Pb-Bi target irradiated with an alpha beam. This method has the potential of upscaling the production due to the convective cooling of the liquid target. In addition, if irradiated with $^{6,7}$Li beams, such a target could lead to the production of $^{211}$Rn as a generator for $^{211}$At. Beside this application, a molten salt loop target is also envisaged for the production of $^{18}$Ne isotopes [143]. The neutrino/antineutrino beams coming from the decay of such β active isotopes is of interest for fundamental studies.

The construction, offline tests and online operation of the LBE loop target will also open perspectives for other liquid targets. As introduced in chapter 1, different molten metals and salts have been studied and operated in the past as ISOL target material. In the favor of faster release times, some of these have however been replaced over the years by solid targets [72]. However, unlike some solid targets, high durability and stability can be achieved with liquid targets under ISOL heat and radiation conditions. Additionally, some solutions have been proposed to corrosion issues, such as a corrosion-resistive nickel-rich alloy container for a molten LiF:NaF eutectic [144] or a dedicated $Y_2O_3$ container for the highly aggressive liquid uranium metal [145]. A renewed interest for molten targets can therefore be expected from improving the release of isotopes from molten targets.

However, prior to the outlook points mentioned above, the prototype will be constructed and tested at CERN-ISOLDE. Offline tests are foreseen this fall and the prototype is planned for online tests in November 2016.

# Appendices

## Appendix A

Details of the irradiation volume concepts studied in section 2.4.

| | Inlet velocity magnitude | Number of evacuation apertures | Evacuation apertures radius | Evacuation apertures spacing | Number of feeder grid apertures | Feeder grid apertures radius | Feeder grid apertures spacing | Mesh size | Required flow rate |
|---|---|---|---|---|---|---|---|---|---|
| Concept 1 | 2 m/s | 2496 | 200 μm | 0.9 mm | No feeder grid | No feeder grid | No feeder grid | $7\ 10^6$ cells | 0.157 l/s |
| Concept 2 | 2 m/s | 4998 | 200 μm | 0.6 mm | No feeder grid | No feeder grid | No feeder grid | $1\ 10^7$ cells | 0.314 l/s |
| Concept 3 | 1 m/s | 2496 | 200 μm | 0.9 mm | No feeder grid | No feeder grid | No feeder grid | $7\ 10^6$ cells | 0.157 l/s |
| Concept 4 | 1.5 m/s | 2496 | 200 μm | 0.9 mm | 11044 | 100 μm | 0.4 mm | $1.3\ 10^7$ cells | 0.178 l/s |
| Concept 5 | 1.5 m/s | 2496 | 200 μm | 0.9 mm | 2496 | 200 μm | 0.9 mm | $2.3\ 10^7$ cells | 0.178 l/s |
| Concept 6 | 0.4 m/s | 2496 | 200 μm | 0.9 mm | 2496 | 200 μm | 0.9 mm | $1.9\ 10^7$ cells | 0.178 l/s |

# List of Figures

# List of Tables

# Bibliography

[1] M. Huyse, The Why and How of Radioactive-Beam Research, in: J. Al-Khalili, E. Roeckl (Eds.) The Euroschool Lectures on Physics with Exotic Beams, Vol. I, Springer Berlin Heidelberg, 2004, pp. 1-32.

[2] D.J. Morrissey, B.M. Sherrill, In-Flight Separation of Projectile Fragments, in: J. Al-Khalili, E. Roeckl (Eds.) The Euroschool Lectures on Physics with Exotic Beams, Vol. I, Springer Berlin Heidelberg, Berlin, Heidelberg, 2004, pp. 113-135.

[3] U. Koster, ISOLDE Collaboration, ISOLDE target and ion source chemistry, Radiochimica Acta, 89 (2001) 749-756.

[4] P. Van Duppen, Isotope Separation On Line and Post Acceleration, in: J. Al-Khalili, E. Roeckl (Eds.) The Euroschool Lectures on Physics with Exotic Beams, Vol. II, Springer Berlin Heidelberg, 2006, pp. 37-77.

[5] M. Lindroos, Review of ISOL-type radioactive beam facilities, European Particle Accelerator Conference, EPAC, Lucerne, Switzerland, 2004, pp. 45-49.

[6] J. Ärje, J. Äystö, H. Hyvönen, P. Taskinen, V. Koponen, J. Honkanen, K. Valli, A. Hautojärvi, K. Vierinen, The ion guide isotope separator on-line, IGISOL, Nuclear Instruments and Methods in Physics Research Section A: Accelerators, Spectrometers, Detectors and Associated Equipment, 247 (1986) 431-437.

[7] J.F. Ziegler, Stopping of energetic light ions in elemental matter, Journal of applied Physics, 85 (1999) 1249-1272.

[8] K.H. Schmidt, E. Hanelt, H. Geissel, G. Munzenberg, J.P. Dufour, The momentum-loss achromat - A new method for the isotopic-separation of relativistic heavy-ions, Nuclear Instruments and Methods in Physics Research Section A-Accelerators Spectrometers Detectors and Associated Equipment, 260 (1987) 287-303.

[9] H. Geissel, T. Schwab, P. Armbruster, J.P. Dufour, E. Hanelt, K.H. Schmidt, B. Sherrill, G. Munzenberg, Ions penetrating through ion-optical systems and matter - non-Liouvillian phase-space modeling, Nuclear Instruments and Methods in Physics Research Section A-Accelerators Spectrometers Detectors and Associated Equipment, 282 (1989) 247-260.

[10] P. Van Duppen, Laser ion sources for on-line isotope separators, Nuclear Instruments and Methods in Physics Research Section B: Beam Interactions with Materials and Atoms, 126 (1997) 66-72.

[11] J. Hüfner, Heavy fragments produced in proton-nucleus and nucleus-nucleus collisions at relativistic energies, Physics Reports, 125 (1985) 129-185.

[12] P.G. Bricault, M. Dombsky, P.W. Schmor, G. Stanford, Radioactive ion beams facility at TRIUMF, Nuclear Instruments and Methods in Physics Research Section B-Beam Interactions with Materials and Atoms, 126 (1997) 231-235.

[13] E. Kugler, D. Fiander, B. Jonson, H. Haas, A. Przewloka, H.L. Ravn, D.J. Simon, K. Zimmer, The new CERN-ISOLDE online mass-separator facility at the PS-Booster, Nuclear Instruments and Methods in Physics Research Section B-Beam Interactions with Materials and Atoms, 70 (1992) 41-49.

[14] G.A. Souliotis, M. Veselsky, G. Chubarian, L. Trache, A. Keksis, E. Martin, A. Ruangma, E. Winchester, S.J. Yennello, Enhanced production of neutron-rich rare isotopes in the reaction of 25 MeV/nucleon 86Kr on 64Ni, Physics Letters B, 543 (2002) 163-172.

[15] J. Benlliure, Spallation Reactions in Applied and Fundamental Research, in: J. Al-Khalili, E. Roeckl (Eds.) The Euroschool Lectures on Physics with Exotic Beams, Vol. II, Springer Berlin Heidelberg, Berlin, Heidelberg, 2006, pp. 191-238.

[16] P. Armbruster, J. Benlliure, M. Bernas, A. Boudard, E. Casarejos, S. Czajkowski, T. Enqvist, S. Leray, P. Napolitani, J. Pereira, F. Rejmund, M.V. Ricciardi, K.H. Schmidt, C. Stephan, J. Taieb, L. Tassan-Got, C. Volant, Measurement of a complete set of nuclides, cross sections, and kinetic energies in spallation of U-238 1A GeV with protons, Physical Review Letters, 93 (2004) 212701.

[17] K. Tshoo, D.Y. Jang, H.J. Woo, B.H. Kang, G.D. Kim, W. Hwang, Y.K. Kim, Design study of 10 kW direct fission target for RISP project, International Nuclear Physics Conference (INPC), Firenze, ITALY, in: EPJ Web of Conferences, 2014, pp. 11016.

[18] P.V. Drumm, J.R.J. Bennett, C.J. Densham, W.R. Evans, M. Holding, G.R. Murdoch, A.H. Evenson, E. Kugler, J. Lettry, H. Ravn, O. Tengblad, P. Van Duppen, R. Catherall, O. Jonsson, J. Kay, D.D. Warner, M. Harder, C. Thwaites, J. Honsi, R. Page, J. Billowes, S.J. Freeman, I.S. Grant, S. Schwebel, G. Smith, C. Bishop, P.M. Walker, A comparison of RIST and ISOLDE tantalum targets and geometries used on-line at ISOLDE, Nuclear Instruments and Methods in Physics Research Section B: Beam Interactions with Materials and Atoms, 126 (1997) 121-124.

[19] P. Kunz, P. Bricault, M. Dombsky, N. Erdmann, V. Hanemaayer, J. Wong, K. Lützenkirchen, Composite uranium carbide targets at TRIUMF: Development and characterization with SEM, XRD, XRF and L-edge densitometry, Journal of Nuclear Materials, 440 (2013) 110-116.

[20] J.R.J. Bennett, U.C. Bergmann, P.V. Drumm, J. Lettry, T. Nilsson, R. Catherall, O.C. Jonsson, H.L. Ravn, H. Simon, Release studies of a thin foil tantalum target for the production of short-lived radioactive nuclei, Nuclear Physics A, 701 (2002) 327-333.

[21] L.C. Carraz, I.R. Haldorsen, H.L. Ravn, M. Skarestad, L. Westgaard, Fast release of nuclear reaction products from refractory matrices, Nuclear Instruments and Methods, 148 (1978) 217-230.

[22] T. Bjornstad, E. Hagebo, P. Hoff, O.C. Jonsson, E. Kugler, H.L. Ravn, S. Sundell, B. Vosicki, Methods for production of intense beams of unstable nuclei - new developments at ISOLDE, Physica Scripta, 34 (1986) 578-590.

[23] T. Bjørnstad, E. Hagebø, P. Hoff, O.C. Jonsson, E. Kugler, H.L. Ravn, S. Sundell, B. Vosicki, Recent development of high-temperature metal targets for ISOLDE, Nuclear Instruments and Methods in Physics Research Section B: Beam Interactions with Materials and Atoms, 26 (1987) 174-182.

[24] T. Bjørnstad, L.C. Carraz, H.Å. Gustafsson, J. Heinemeier, B. Jonson, O.C. Jonsson, V. Lindfors, S. Mattsson, H.L. Ravn, New targets for on-line mass separation of nuclei formed in 600 MeV proton and 910 MeV 3He

reactions, Nuclear Instruments and Methods in Physics Research, 186 (1981) 391-400.

[25] V.N. Panteleev, O. Alyakrinskiy, A. Andrighetto, A.E. Barzakh, M. Dubois, C. Eleon, S. Essabaa, O. Bajeat, D.V. Fedorov, G. Gaubert, A.M. Ionan, V.S. Ivanov, P. Jardin, A. Lanchais, C. Lau, R. Leroy, G. Lhersonneau, C. Mhamed, K.A. Mezilev, P.L. Molkanov, F.V. Moroz, S.Y. Orlov, V. Rizzi, M.G. Saint Laurent, L. Stroe, L.B. Tecchio, A.C.C. Villari, Y.M. Volkov, Recent developments and on-line tests of uranium carbide targets for production of nuclides far from stability, European Physical Journal-Special Topics, 150 (2007) 297-300.

[26] L.C. Carraz, S. Sundell, H.L. Ravn, M. Skarestad, L. Westgaard, High-temperature carbide targets for fast on-line mass separation of alkali and noble gas elements, Nuclear Instruments and Methods, 158 (1979) 69-80.

[27] E. Hagebø, P. Hoff, O.C. Jonsson, E. Kugler, J.P. Omtvedt, H.L. Ravn, K. Steffensen, New production systems at ISOLDE, Nuclear Instruments and Methods in Physics Research Section B: Beam Interactions with Materials and Atoms, 70 (1992) 165-174.

[28] H.L. Ravn, T. Bjørnstad, P. Hoff, O.C. Jonsson, E. Kugler, S. Sundell, B. Vosički, Use of refractory oxides, carbides and borides as targets for on-line mass separation, Nuclear Instruments and Methods in Physics Research Section B: Beam Interactions with Materials and Atoms, 26 (1987) 183-189.

[29] H.L. Ravn, R. Catherall, J. Barker, P. Drumm, A.H.M. Evensen, E. Hagebø, P. Hoff, O.C. Jonsson, E. Kugler, J. Lettry, K. Steffensen, O. Tengblad, Bunched release of gases from oxide targets, Nuclear Instruments and Methods in Physics Research Section B: Beam Interactions with Materials and Atoms, 126 (1997) 176-181.

[30] J. Lettry, R. Catherall, P. Drumm, A. Evenson, O. Jonnson, E. Kugler, H. Ravn, J. Obert, J.C. Putaux, J. Sauvage, M. Toulemonde, Experience with ISOLDE molten metal targets at the CERN PS-Booster, Proceedings of the meetings ICANS-XIII and ESS-PM4 Volume II, Paul Scherrer Institut, Switzerland, 1995, pp. 595-603.

[31] H.L. Ravn, S. Sundell, L. Westgaard, Target Techniques for the isolde on-line isotope separator, Nuclear Instruments and Methods, 123 (1975) 131-144.

[32] P. Hoff, O.C. Jonsson, E. Kugler, H.L. Ravn, Release of nuclear reaction products from refractory compounds, Nuclear Instruments and Methods in Physics Research, 221 (1984) 313-329.

[33] J. Lettry, R. Catherall, G. Cyvoct, P. Drumm, A.H.M. Evensen, M. Lindroos, O.C. Jonsson, E. Kugler, J. Obert, J.C. Putaux, J. Sauvage, K. Schindl, H. Ravn, E. Wildner, Release from ISOLDE molten metal targets under pulsed proton beam conditions, Nuclear Instruments & Methods in Physics Research Section B-Beam Interactions with Materials and Atoms, 126 (1997) 170-175.

[34] D. Houngbo, L. Popescu, P. Schuurmans, M. Delonca, R. Losito, C. Maglioni, T. Stora, P. Bricault, J. Vierendeels, CFD analysis and optimization of a liquid lead–bismuth loop target for ISOL facilities, Nuclear Instruments and Methods in Physics Research Section A: Accelerators, Spectrometers, Detectors and Associated Equipment, 777 (2015) 202-210.

[35] H.A. Abderrahim, P. Baeten, D. De Bruyn, J. Heyse, P. Schuurmans, J. Wagemans, MYRRHA, a Multipurpose hYbrid Research Reactor for High-end Applications, Nuclear Physics News, 20 (2010) 24-28.

[36] L. Popescu, (for the ISOL@MYRRHA and MYRRHA Collaborations), Nuclear-physics applications of MYRRHA, INPC2013 Conference proceedings, in: EPJ Web of Conferences, 2014, pp. 10011.

[37] SCK-CEN, ISOL@MYRRHA Homepage, http://isolmyrrha.sckcen.be/, accessed on 06-01-2016.

[38] A. Bonaccorso, G. Prete, EURISOL: an European Isotope Separation On-Line radioactive ion beam facility, Journal of Physics: Conference Series, 168 (2009) 012023.

[39] The EURISOL Report – A Feasibility Study for a European Isotope-Separation-On-Line Radioactive Ion Beam Facility, GANIL, Caen, France, 2003.

[40] EURISOL project Coordination Board, Final report of the EURISOL design study (2005-2009), John Cornell ed., GANIL, http://www.eurisol.org/eurisol_design_study_final_report-1156.html, 2009.

[41] G.D.A. Y. Zhang, Design of high-power ISOL targets for radioactive ion beam generation, Nuclear Instruments and Methods in Physics Research Section A: Accelerators, Spectrometers, Detectors and Associated Equipment, 521 (2004) 72–107.

[42] P. Bricault, M. Dombsky, A. Dowling, M. Lane, High power target developments at ISAC, Nuclear Instruments and Methods in Physics Research Section B-Beam Interactions with Materials and Atoms, 204 (2003) 319-324.

[43] M. Dombsky, P. Bricault, High intensity targets for ISOL, historical and practical perspectives, Nuclear Instruments and Methods in Physics Research Section B: Beam Interactions with Materials and Atoms, 266 (2008) 4240–4246.

[44] T. Stora, Recent developments of target and ion sources to produce ISOL beams, Nuclear Instruments and Methods in Physics Research Section B: Beam Interactions with Materials and Atoms, 317, Part B (2013) 402-410.

[45] E. Noah, R. Catherall, Y. Kadi, C. Kharoua, J. Lettry, T. Stora, Driver beam-led EURISOL target design constraints, Proceedings of EPAC'08, the 11th European Particle Accelerator Conference, Genoa, Italy, 2008, pp. 271-273.

[46] T. Stora, J. Lettry, R. Catherall, E. Noah, R. Wilfinger, L. Penescu, E. Bouquerel, S. Fernandes, M. Santana-Leitner, L. Zanini, I. Guenter, F. Groeschel, The EURISOL facility: Feasibility study for the 100 kW direct targets, internal task note EURISOL project, http://www.eurisol.org/site02/doc_details.php?url=search_results.php&operation=download&docu=450&type, (accessed on 06-01-2016), 2006.

[47] K. Heyde, J.L. Wood, Shape coexistence in atomic nuclei, Reviews of Modern Physics, 83 (2011) 1467-1521.

[48] M. Andersson, Measurement of gas and volatile elements production rates in molten lead bismuth target, Master thesis, Dep. of Nuclear Physics, LTH Lund, Sweden, Paul Scherrer Institut, Villigen, Switzerland, 2004, pp. 66.

[49] Y. Blumenfeld, P. Butler, J. Cornell, G. Fortuna, M. Lindroos, EURISOL Design Study: towards an ultimate ISOL facility for Europe, International Journal of Modern Physics E-Nuclear Physics, 18 (2009) 1960-1964.

[50] T.V. Dury, CFD design support at PSI for the international MEGAPIE liquid-metal spallation target, Journal of Nuclear Science and Technology, 41 (2004) 285-295.

[51] K. Samec, R.Ž. Milenković, S. Dementjevs, M. Ashrafi-Nik, A. Kalt, Design of a compact high-power neutron source—The EURISOL converter target, Nuclear Instruments and Methods in Physics Research Section A: Accelerators, Spectrometers, Detectors and Associated Equipment, 606 (2009) 281-290.

[52] E. Noah, L. Bruno, R. Catherall, J. Lettry, T. Stora, Hydrodynamics of ISOLDE liquid metal targets, Nuclear Instruments & Methods in Physics Research Section B-Beam Interactions with Materials and Atoms, 266 (2008) 4303-4307.

[53] R.Ž. Milenković, S. Dementjevs, K. Samec, A. Flerov, K. Thomsen, Wavelet analysis of experimental results for coupled structural–hydraulic behavior of the EURISOL target mock-up, Nuclear Instruments and Methods in Physics Research Section A: Accelerators, Spectrometers, Detectors and Associated Equipment, 608 (2009) 175-182.

[54] P. Jung, T. Koppitz, G. Muller, A. Weisenburger, M. Futakawa, Y. Ikeda, Improved cavitation resistance of structural materials in pulsed liquid metal targets by surface hardening, Journal of Nuclear Materials, 343 (2005) 92-100.

[55] J. Lettry, R. Catherall, P. Drumm, P. Van Duppen, A.H.M. Evensen, G.J. Focker, A. Jokinen, O.C. Jonsson, E. Kugler, H. Ravn, Pulse shape of the ISOLDE radioactive ion beams, Nuclear Instruments and Methods in Physics Research Section B: Beam Interactions with Materials and Atoms, 126 (1997) 130-134.

[56] E. Platacis, K. Kravalis, Electromagnetic pump feasibility for LIEBE, Private communication, Institute of Physics of the University of Latvia, Latvia, 2012.

[57] C. Clanet, J.C. Lasheras, Transition from dripping to jetting, Journal of Fluid Mechanics, 383 (1999) 307-326.

[58] J. Delteil, S. Vincent, A. Erriguible, P. Subra-Paternault, Numerical investigations in Rayleigh breakup of round liquid jets with VOF methods, Computers & Fluids, 50 (2011) 10-23.

[59] J.B. Blaisot, S. Adeline, Instabilities on a free falling jet under an internal flow breakup mode regime, International Journal of Multiphase Flow, 29 (2003) 629-653.

[60] J. Eggers, E. Villermaux, Physics of liquid jets, Reports on Progress in Physics, 71 (2008) 036601.

[61] B. Chang, G. Nave, S. Jung, Drop formation from a wettable nozzle, Communications in Nonlinear Science and Numerical Simulation, 17 (2012) 2045-2051.

[62] W. van Hoeve, S. Gekle, J.H. Snoeijer, M. Versluis, M.P. Brenner, D. Lohse, Breakup of diminutive Rayleigh jets, Physics of Fluids, 22 (2010) 122003.

[63] S.P. Lin, R.D. Reitz, Drop and spray formation from a liquid jet, Annual Review of Fluid Mechanics, 30 (1998) 85-105.

[64] M. Vanderhaegen, J. Vierendeels, B. Arien, CFD analysis of the MYRRHA primary cooling system, Nuclear Engineering and Design, 241 (2011) 775-784.

[65] J. Wolters, G. Hansen, E.M.J. Komen, F. Roelofs, Validation of CFD Models with Respect to the Thermal-Hydraulic Design of the ESS target, IAEA Technical Meeting, http://www.fz-juelich.de/cae/servlet/contentblob/930156/publicationFile/12559/ValidationCFDESS.pdf, (accessed on 06-01-2016), Karlsruhe, Germany, 2003.

[66] C. Fazio, F. Gröschel, W. Wagner, K. Thomsen, B.L. Smith, R. Stieglitz, L. Zanini, A. Guertin, A. Cadiou, J. Henry, P. Agostini, Y. Dai, H. Heyck, S. Dementjev, S. Panebianco, A. Almazouzi, J. Eikenberg, A. Letourneau, J.C. Toussaint, A. Janett, C. Perret, S. Joray, J. Patorski, W. Leung, P. Meloni, P. Turroni, A. Zucchini, G. Benamati, J. Konys, T.

Auger, A. Gessi, D. Gorse, I. Serre, A. Terlain, J.B. Vogt, A. Batta, A. Class, X. Cheng, F. Fellmoser, M. Daubner, S. Gnieser, G. Grötzbach, R. Milenkovic, C. Latgé, J.U. Knebel, The MEGAPIE-TEST project: Supporting research and lessons learned in first-of-a-kind spallation target technology, Nuclear Engineering and Design, 238 (2008) 1471-1495.

[67] K. Samec, R.Z. Milenkovic, L. Blumenfeld, S. Dementjevs, C. Kharoua, Y. Kadi, Measurement and analysis of turbulent liquid metal flow in a high-power spallation neutron source-EURISOL, Nuclear Instruments & Methods in Physics Research Section A-Accelerators Spectrometers Detectors and Associated Equipment, 638 (2011) 1-10.

[68] R. Stieglitz, M. Daubner, A. Batta, C.H. Lefhalm, Turbulent heat mixing of a heavy liquid metal flow in the MEGAPIE target geometry—The heated jet experiment, Nuclear Engineering and Design, 237 (2007) 1765-1785.

[69] N.E. Agency, Handbook on Lead-bismuth Eutectic Alloy and Lead Properties, Materials Compatibility, Thermal-hydraulics and Technologies, in: OECD (Ed.), 2007.

[70] J. Lettry, G. Arnau, M. Benedikt, S. Gilardoni, R. Catherall, U. Georg, G. Cyvogt, A. Fabich, O. Jonsson, H. Ravn, S. Sgobba, G. Bauer, H. Brucherstseifer, T. Graber, C. Güdermann, L. Ni, R. Rastani, Effects of thermal shocks on the release of radioisotopes and on molten metal target vessels, Nuclear Instruments and Methods in Physics Research Section B: Beam Interactions with Materials and Atoms, 204 (2003) 251-256.

[71] P. Van Duppen, Technological challenges of new radioactive beam facilities, Nuclear Instruments & Methods in Physics Research Section B-Beam Interactions with Materials and Atoms, 204 (2003) 9-16.

[72] A. Gottberg, Target materials for exotic ISOL beams, Nuclear Instruments and Methods in Physics Research Section B: Beam Interactions with Materials and Atoms, 376 (2016) 8-15.

[73] C.M. Grinstead, J.L. Snell, Sums of Random Variables (Chapter 7), in: Introduction to Probability, American Mathematical Society, 1997, pp. 285-304.

[74] R. Kirchner, On the release and ionization efficiency of catcher-ion-source systems in isotope separation on-line, Nuclear Instruments and Methods in Physics Research Section B: Beam Interactions with Materials and Atoms, 70 (1992) 186-199.

[75] G. Lhersonneau, A.E. Barzarkh, V. Rizzi, O. Alyakrinskiy, K.A. Mezilev, F.V. Moroz, V.N. Panteleev, L.B. Tecchio, Influence of radioactive filiation on measured release curves, Nuclear Instruments & Methods in Physics Research Section a-Accelerators Spectrometers Detectors and Associated Equipment, 566 (2006) 465-471.

[76] G. Lhersonneau, A.E. Barzakh, V. Rizzi, O. Alyakrinskiy, K.A. Mezilev, F.V. Moroz, V.N. Panteleev, L.B. Tecchio, Influence of decay in the target on the measurement of release times and release efficiency, Nuclear Instruments & Methods in Physics Research Section B-Beam Interactions with Materials and Atoms, 266 (2008) 4314-4317.

[77] B.E. Poling, J.M. Prausnitz, J.P. O'Connell, The properties of gases and liquids, 5 ed., McGraw-Hill, New York, 2004.

[78] E.L. Cussler, Diffusion mass transfer in fluid systems, 3 ed., Cambridge University Press, Cambridge, 2007.

[79] J. Tsu-Wei Su, Mass Transfer in Multi-Phase Single Particle Systems, PhD thesis, Department of Mechanical Engineering and Materials Science Duke University, USA, 2011, pp. 198.

[80] H.J.V. Tyrrell, K.R. Harris, Diffusion in liquids: a theoretical and experimental study, Butterworths, London, 1984.

[81] J. Crank, G.S. Park, Diffusion in polymers, Academic Press Inc, London, 1968.

[82] M.H. Cohen, D. Turnbull, Molecular Transport in Liquids and Glasses, Journal of Chemical Physics, 31 (1959) 1164-1169.

[83] N.H. March, M.P. Tosi, Introduction to Liquid State Physics, World Scientific Pub Co Inc, Singapore, 2002.

[84] P. Neogi, Diffusion in Polymers, CRC Press, New York, 1996.

[85] P.B. Macedo, T.A. Litovitz, On the Relative Roles of Free Volume and Activation Energy in the Viscosity of Liquids, Journal of Chemical Physics, 42 (1965) 245-256.

[86] J. Crank, The mathematics of diffusion, Clarendon Press, Oxford, 1975.

[87] M. Fujioka, Y. Arai, Diffusion of radioisotopes from solids in the form of foils, fibers and particles, Nuclear Instruments and Methods in Physics Research, 186 (1981) 409-412.

[88] A. Latuszyński, Investigation of the diffusion process at electromagnetic separation of the radioactive isotopes of rare-earth elements, Nuclear Instruments and Methods, 123 (1975) 489-494.

[89] H. Mehrer, Diffusion in Solids: Fundamentals, Methods, Materials, Diffusion-Controlled Processes, Springer Berlin Heidelberg, 2007.

[90] G.J. Beyer, E. Hagebø, A.F. Novgorodov, H.L. Ravn, The role of diffusion in ISOL targets for the production of radioactive ion beams, Nuclear Instruments and Methods in Physics Research Section B: Beam Interactions with Materials and Atoms, 204 (2003) 225-234.

[91] G.J. Beyer, W.D. Fromm, A.F. Novgorodov, Trace diffusion of different nuclear reaction products in polycrystalline tantalum, Nuclear Instruments and Methods, 146 (1977) 419-430.

[92] A. Fick, Ueber Diffusion, Annalen der Physik, 170 (1855) 59-86.

[93] H.L. Ravn, L.C. Carraz, J. Denimal, E. Kugler, M. Skarestad, S. Sundell, L. Westgaard, New techniques at ISOLDE-2, Nuclear Instruments and Methods, 139 (1976) 267-273.

[94] M. Santana Leitner, A Monte Carlo Code to optimize the production of radioactive ion beams by the ISOL technique, PhD Thesis, Technical University of Catalonia (UPC), CERN, 2005.

[95] A.K. Roy, R.P. Chhabra, Prediction of solute diffusion-coefficients in liquid-metals, Metallurgical Transactions a-Physical Metallurgy and Materials Science, 19 (1988) 273-279.

[96] W. Huang, The measurement of precise solute diffusion coefficients in molten metals and semiconductors, PhD thesis, Queen's University, Kingston, Ontario, Canada, 2003.

[97] R. Kirchner, An ion source with bunched beam release, Nuclear Instruments and Methods in Physics Research Section B: Beam Interactions with Materials and Atoms, 26 (1987) 204-212.

[98] P.G. Bricault, M. Dombsky, P.W. Schmor, A. Dowling, High power targets for ISOL radioactive ion beam facility, Proceedings of the Particle Accelerator Conference (PAC), 2003, pp. 439-443.

[99] H. Rossbach, B. Eichler, Adsorption of metals on metal surfaces and the possibilities of its application in nuclear chemistry, zentralinstitut für kernforschung, German Democratic Republic, 1984, pp. 20.

[100] J.C. Bilheux, G.D. Alton, Y. Liu, S.N. Murray, C. Williams, C.A. Reed, A universal method for effusive-flow characterization of target/vapor transport systems for RIB generation, Proceedings of the Particle Accelerator Conference (PAC), 2001, pp. 1610-1612.

[101] B. Mustapha, J.A. Nolen, Optimization of ISOL targets based on Monte-Carlo simulations of ion release curves, Nuclear Instruments & Methods in Physics Research Section B-Beam Interactions with Materials and Atoms, 204 (2003) 286-292.

[102] J.R.J. Bennett, An improved analytical model of diffusion through the RIST target, Nuclear Instruments and Methods in Physics Research Section B: Beam Interactions with Materials and Atoms, 204 (2003) 211-214.

[103] Y. Zhang, G.D. Alton, Monte-Carlo simulation of complex vapor-transport systems for RIB applications, Nuclear Instruments and Methods in Physics Research Section B: Beam Interactions with Materials and Atoms, 241 (2005) 947-952.

[104] B. Roussière, F. Ibrahim, J. Sauvage, O. Bajeat, N. Barré, F. Clapier, E. Cottereau, C. Donzaud, M. Ducourtieux, S. Essabaa, D. Guillemaud-Mueller, C. Lau, H. Lefort, C.F. Liang, F. Le Blanc, A.C. Mueller, J. Obert, N. Pauwels, J.C. Potier, F. Pougheon, J. Proust, O. Sorlin, D. Verney, A. Wojtasiewicz, Release properties of UCx and molten U targets, Nuclear

Instruments and Methods in Physics Research Section B: Beam Interactions with Materials and Atoms, 194 (2002) 151-163.

[105] F. Sharipov, V. Seleznev, Data on internal rarefied gas flows, Journal of Physical and Chemical Reference Data, 27 (1998) 657-706.

[106] P. Jeerasak, W. Rugkanawan, Rarefied gas flow in pressure and vacuum measurements, Acta IMEKO, 3 (2014) 60-63.

[107] C.J. Smithells, Metals reference book, Butterworths, London, 1962.

[108] E.J.A. Bouquerel, Atomic beam merging and suppression of Alkali Contaminants in multi body high power targets design and test of target and ion source prototypes at ISOLDE, PhD thesis, Université Paris-Sud XI, 2009, pp. 100.

[109] F.J. Alexander, A.L. Garcia, The direct simulation Monte Carlo method, Computers in Physics, 11 (1997) 588-593.

[110] A.L. Garcia, Direct Simulation Monte Carlo: Theory, Methods, and Open Challenges, Report of the Department of Physics & Astronomy, San Jose State University and Center for Computational Sciences and Engineering, Lawrence Berkeley Nat. Lab., USA, 2011, pp. 12.

[111] X. Luo, C. Day, Investigation of a New Monte Carlo Method for the Transitional Gas Flow, 27th International Symposium on Rarefied Gas Dynamics, Asilomar Conf Grounds, Pacific Grove, CA, 2010, pp. 272-276.

[112] P. Ossipov, The angular coefficient method for calculating the stationary molecular gas flow for arbitrary reflection law, Vacuum, 48 (1997) 409-412.

[113] C. Garion, Monte Carlo method implemented in a finite element code with application to dynamic vacuum in particle accelerators, Vacuum, 84 (2009) 274-276.

[114] Y. Suetsugu, Application of the Monte Carlo method to pressure calculation, Journal of Vacuum Science & Technology a-Vacuum Surfaces and Films, 14 (1996) 245-250.

[115] R. Kersevan, J.L. Pons, Introduction to MOLFLOW plus : New graphical processing unit-based Monte Carlo code for simulating molecular flows and for calculating angular coefficients in the compute unified device architecture environment, Journal of Vacuum Science & Technology A, 27 (2009) 1017-1023.

[116] M. Ady, R. Kersevan, Introduction to the latest version of the test-particle Monte Carlo code Molflow, IPAC 2014: Proceedings of the 5th International Particle Accelerator Conference, 2014, pp. 2348-2350.

[117] M. ADY, R. KERSEVAN, MolFlow+ user guide, https://test-molflow.web.cern.ch/sites/test-molflow.web.cern.ch/files/molflow_user_guide.pdf, accessed on 06-01-2016.

[118] A. Roth, Vacuum technology, North-Holland Pub. Co., Amsterdam; New York, 1982.

[119] D.M. Ruthven, Principles of adsorption and adsorption processes, Wiley, New York, 1984.

[120] L.B. Loeb, The Kinetic Theory of Gases: Being a Text and Reference Book Whose Purpose is to Combine the Classical Deductions with Recent Experimental Advances in a Convenient Form for Student and Investigator, McGraw-Hill, New York, 1934.

[121] K.W. Kolasinski, Surface science : foundations of catalysis and nanoscience, Wiley, New York, 2002.

[122] J.H. Lambert, Photometria sive de mensure de gratibus luminis, colorum umbrae, Eberhard Klett1760.

[123] M.N. Kogan, Rarefied Gas Dynamics, Plenum Press, New York, 1969.

[124] J.C. Maxwell, On the Dynamical Theory of Gases, Philosophical Transactions of the Royal Society of London, 157 (1966) 49-88.

[125] B.T. Phong, Illumination for Computer-Generated Images, PhD thesis, AD-A008, Department of Computer Science, Utah University, Utah, 1973.

[126] K.E. Torrance, E.M. Sparrow, Theory for Off-Specular Reflection From Roughened Surfaces, Journal of the Optical Society of America, 57 (1967) 1105-1114.

[127] J. Blinn, Models of light reflection for computer synthesized pictures, SIGGRAPH Computer Graphics, 11 (1977) 192-198.

[128] N.V. Blinov, D.V. Kul'ginov, Quasi-classical description of the single-phonon scattering of an atom by a surface in the diffraction regime Zhurnal Tekhnicheskoi Fiziki, 65 (1995) 93-105.

[129] l. Egoriti, S. Boeckx, L. Ghys, D. Houngbo, L. Popescu, Analytical model for release calculations in solid thin-foils ISOL targets, Nuclear Instruments and Methods in Physics Research Section A: Accelerators, Spectrometers, Detectors and Associated Equipment, 832 (2016) 202-207.

[130] S. Alexey, MCNP calculations of the production of Hg Isotopes in an LBE ISOL-target, Private communication, SCK-CEN, 2015.

[131] J. Vierendeels, FLUID MECHANICS lecture notes, Ghent, Academic Year 2012-2013, pp. 291.

[132] S.P. Chabod, J.C. David, D. Ene, D. Ridikas, N. Thiolliere, In-target radioactive nuclei production rates with EURISOL single-stage target configuration, European Physical Journal A, 45 (2010) 131-145.

[133] P.R.S. A. Ferrari, A. Fassò,and J. Ranft, FLUKA: a multi-particle transport code, CERN-2005-10 (2005), INFN/TC_05/11, SLAC-R-773, 2005.

[134] ISOLDE-CERN, ISOLDE Yield Database, Available at https://test-isolde-yields.web.cern.ch/test-isolde-yields/query_tgt.htm, (accessed 17.04.15).

[135] J. Dilling, R. Krücken, L. Merminga, ISAC and ARIEL: The TRIUMF Radioactive Beam Facilities and the Scientific Program, Springer Netherlands, Dordrecht, 2014.

[136] A. Herlert, Y. Kadi, The HIE-ISOLDE Project, Proceedings of the International Nuclear Physics Conference (INPC), in: Journal of Physics Conference Series, TRIUMF, Vancouver, CANADA, 2011, pp. 052010.

[137] H.J. Woo, B.H. Kang, K. Tshoo, C.S. Seo, W. Hwang, Y.H. Park, J.W. Yoon, S.H. Yoo, Y.K. Kim, D.Y. Jang, Overview of the ISOL facility for the RISP, Journal of the Korean Physical Society, 66 (2015) 443-448.

[138] A. Andrighetto, L. Biasetto, M. Manzolaro, D. Scarpa, J. Montano, J. Stanescu, P. Benetti, I. Cristofolini, M.S. Carturan, P. Colombo, P. di Bernardo, M. Guerzoni, G. Meneghetti, B.D. Monelli, G. Prete, G. Puglierin, A. Tomaselli, P. Zanonato, Production of high-intensity RIB at SPES, Nuclear Physics A, 834 (2010) 754C-757C.

[139] M. Lewitowicz, S.p. group, The SPIRAL 2 project, Proceedings of the Symposium on Nuclear Physics VI, Tours, FRANCE, 2006, pp. 91-98.

[140] S. Fernandes, Submicro and Nano Structured Porous Materials for the Production of High-Intensity Exotic Radioactive Ion Beams, PhD thesis, Ecole Polytechnique, Lausanne, Ecole Polytechnique, Lausanne, Lausanne : EPFL, 2010, pp. 248.

[141] A. Kjelberg, G. Rudstam, The ISOLDE isotope separator on-line facility at CERN, CERN Report, Geneva, 1970, pp. 140.

[142] S. Rothe, A.N. Andreyev, S. Antalic, A. Borschevsky, L. Capponi, T.E. Cocolios, H. De Witte, E. Eliav, D.V. Fedorov, V.N. Fedosseev, D.A. Fink, S. Fritzsche, L. Ghys, M. Huyse, N. Imai, U. Kaldor, Y. Kudryavtsev, U. Koester, J.F.W. Lane, J. Lassen, V. Liberati, K.M. Lynch, B.A. Marsh, K. Nishio, D. Pauwels, V. Pershina, L. Popescu, T.J. Procter, D. Radulov, S. Raeder, M.M. Rajabali, E. Rapisarda, R.E. Rossel, K. Sandhu, M.D. Seliverstov, A.M. Sjoedin, P. Van den Bergh, P. Van Duppen, M. Venhart, Y. Wakabayashi, K.D.A. Wendt, Measurement of the first ionization potential of astatine by laser ionization spectroscopy, Nature Communications, 4 (2013) 1835.

[143] T.M. Mendonca, R. Hodak, T. Stora, Opportunities for neutrino experiments at ISOLDE, Proceedings of the 13th International Workshop on Neutrino Factories, Super beams and Beta beams (NUFACT), in: Journal of Physics Conference SeriesProceedings of the 13th International Workshop

on Neutrino Factories, Super beams and Beta beams (NUFACT), in: Journal of Physics Conference Series, Geneva, Switzerland, 2011.

[144] T.M. Mendonca, R. Hodak, V. Ghetta, M. Allibert, D. Heuer, E. Noah, S. Cimmino, M. Delonca, A. Gottberg, M. Kronberger, J.P. Ramos, C. Seiffert, T. Stora, Production and release of ISOL beams from molten fluoride salt targets, Nuclear Instruments & Methods in Physics Research Section B-Beam Interactions with Materials and Atoms, 329 (2014) 1-5.

[145] S. Kandri-Rody, J. Obert, E. Cottereau, O. Bajeat, M. Ducourtieux, C. Lau, H. Lefort, J.C. Potier, J.C. Putaux, F. Clapier, J. Lettry, A.C. Mueller, N. Pauwels, J. Proust, C.F. Liang, P. Paris, H.L. Ravn, B. Roussiere, J. Sauvage, J.A. Scarpaci, F. Le Blanc, G. Lalu, I. Lhenry, T. Von Egidy, R. Antoni, Exotic nuclei produced by fast neutrons in a liquid uranium target, Nuclear Instruments & Methods in Physics Research Section B-Beam Interactions with Materials and Atoms, 160 (2000) 1-6.